

BOSTON UNIVERSITY  
COLLEGE OF ENGINEERING

Dissertation

**CLINICAL FEASIBILITY OF DIFFUSE OPTICAL  
SPECTROSCOPIC IMAGING IN SARCOMA**

by

**HANNAH M. PETERSON**

B.S., Rensselaer Polytechnic Institute, 2011  
M.S., Boston University, 2016

Submitted in partial fulfillment of the  
requirements for the degree of  
Doctor of Philosophy

2019

© 2019 by  
HANNAH M. PETERSON  
All rights reserved

Approved by

First Reader

---

Darren Roblyer, Ph.D.  
Assistant Professor of Biomedical Engineering

Second Reader

---

Bang H. Hoang, M.D.  
Professor of Orthopaedic Surgery  
Albert Einstein College of Medicine

Third Reader

---

Catherine M. Klapperich, Ph.D.  
Associate Dean for Research and Technology Development  
Professor of Biomedical Engineering  
Professor of Materials Science and Engineering  
Professor of Mechanical Engineering

Fourth Reader

---

Elise Morgan, Ph.D.  
Professor of Mechanical Engineering  
Professor of Materials Science and Engineering  
Professor of Biomedical Engineering

Fifth Reader

---

Ji Yi, Ph.D.  
Assistant Professor of Medicine  
Assistant Professor of Biomedical Engineering

*Facilis descensus Averni;  
Noctes atque dies patet atri janua Ditis;  
Sed revocare gradum, superasque evadere ad auras,  
Hoc opus, hic labor est.* Virgil (from Don's thesis!)



## **Dedication**

To all of my patients, especially those no longer with us.

## Acknowledgments

# CLINICAL FEASIBILITY OF DIFFUSE OPTICAL SPECTROSCOPIC IMAGING IN SARCOMA

HANNAH M. PETERSON

Boston University, College of Engineering, 2019

Major Professor: Darren Roblyer, Ph.D.

Assistant Professor of Biomedical Engineering

## ABSTRACT

Sarcomas are broadly defined as cancers that form in the bone, soft tissue, or connective tissue. While they represent only 1% of all cancers in the United States, sarcomas constitute 12% of all childhood cancers. Five-year survival has not changed in over 40 years. The only clinically accepted indicator of pathologic response and disease-free survival is percent tumor-cell necrosis at time of surgery—there are no established prognostic markers before surgery. Unfortunately, 40–70% of patients have a poor pathologic response and attempts to modify treatment to improve their outcomes have been unsuccessful. Diffuse Optical Spectroscopic Imaging (DOSI) is a non-invasive, functional imaging technique that has been previously implemented to predict pathologic response in patients with breast cancer. Specifically, DOSI combines frequency amplitude modulated near-infrared light and broadband continuous wave light to measure quantitative concentrations of oxyhemoglobin, deoxyhemoglobin, water, and lipids. This project developed and validated DOSI as a new non-invasive measurement modality to track treatment for sarcomas. For the first time, the optical properties and functional hemodynamic information of the distal femur, tibia, and humerus were characterized in normal volunteers. DOSI demon-

strated the ability to measure optical properties and functional information at several sarcoma locations throughout the course of treatment. It was able to differentiate between healthy and sarcoma tissues within a patient. Improvements made to the instrumentation will facilitate future measurements in this patient population. In the future, DOSI may provide a way to monitor treatment response and improve patient outcomes.

# Contents

<b>1</b>	<b>Background and significance</b>	<b>1</b>
1.1	Sarcomas . . . . .	1
1.1.1	Epidemiology and diagnosis . . . . .	1
1.1.2	Treatment and survival . . . . .	2
1.1.3	Prognostic markers . . . . .	3
1.2	Diffuse Optical Spectroscopic Imaging . . . . .	4
1.2.1	Instrumentation . . . . .	4
1.2.2	Optical properties and functional hemodynamic information calculations . . . . .	5
1.2.3	Potential as a prognostic tool . . . . .	6
1.2.4	Previous diffuse optics work in bone . . . . .	6
1.3	Goal of this dissertation . . . . .	7
<b>2</b>	<b>Characterize the optical properties and hemodynamics of normal volunteers in common sarcoma locations</b>	<b>8</b>
2.1	Introduction . . . . .	8
2.2	Methods . . . . .	8
2.2.1	Subject eligibility and enrollment . . . . .	8
2.2.2	DOSI instrumentation . . . . .	9
2.2.3	Imaging procedures . . . . .	10
2.2.4	Data quality control . . . . .	11
2.2.5	Estimates of body fat percentage . . . . .	12

2.2.6	Comparison of optical properties and chromophore concentrations	12
2.3	Results . . . . .	13
2.3.1	Subject enrollment . . . . .	13
2.3.2	Optical properties . . . . .	14
2.3.3	Chromophore concentrations . . . . .	16
2.3.4	Longitudinal measurements . . . . .	23
2.4	Discussion . . . . .	26
2.4.1	Limitations . . . . .	27
2.4.2	Conclusions . . . . .	29
<b>3</b>	<b>Determine if DOSI can detect differences between normal and sarcoma tissue</b>	<b>30</b>
3.1	Introduction . . . . .	30
3.2	Methods . . . . .	31
3.2.1	Subject eligibility and enrollment . . . . .	31
3.2.2	DOSI instrumentation . . . . .	31
3.2.3	Imaging procedures . . . . .	31
3.2.4	Data quality . . . . .	32
3.2.5	Estimates of signal-to-noise ratio . . . . .	32
3.2.6	Estimates of tumor depth . . . . .	32
3.2.7	Estimates of imaging depth . . . . .	33
3.2.8	Comparison of optical properties and chromophore concentrations	33
3.3	Results . . . . .	33
3.3.1	Subject enrollment and tumor characteristics . . . . .	33
3.3.2	Estimates of signal-to-noise ratio at baseline . . . . .	36
3.3.3	Estimates of tumor and imaging depths at baseline . . . . .	37
3.3.4	Optical properties at baseline . . . . .	38

3.3.5	Chromophore concentrations at baseline . . . . .	43
3.4	Discussion . . . . .	47
3.4.1	Limitations . . . . .	49
3.4.2	Conclusions . . . . .	51
<b>4</b>	<b>Optimize DOSI instrumentation for sarcoma</b>	<b>53</b>
4.1	Introduction . . . . .	53
4.2	Methods . . . . .	53
4.2.1	Literature review of optical properties . . . . .	53
4.2.2	Selection of optical property test set . . . . .	54
4.2.3	Creation of tissue-mimicking phantoms . . . . .	55
4.2.4	DOSI instrumentation . . . . .	55
4.2.5	Calculation of signal-to-noise ratio . . . . .	56
4.2.6	Calculation of accuracy and precision . . . . .	56
4.2.7	Monte Carlo estimates of imaging depth . . . . .	57
4.2.8	Optimal source-detector separation . . . . .	57
4.2.9	Probe housing considerations . . . . .	58
4.3	Results . . . . .	58
4.3.1	Literature review of optical properties . . . . .	58
4.3.2	Selection of optical property test set . . . . .	60
4.3.3	Signal-to-noise ratio . . . . .	62
4.3.4	Accuracy and precision . . . . .	65
4.3.5	Estimates of imaging depth . . . . .	68
4.3.6	Optimal source-detector separation . . . . .	69
4.3.7	Probe housing . . . . .	72
4.4	Discussion . . . . .	72
4.4.1	Limitations . . . . .	74

4.4.2	Conclusions . . . . .	75
<b>5</b>	<b>Conclusions</b>	<b>76</b>
5.1	Discussion . . . . .	76
5.2	Future directions . . . . .	79
5.2.1	Instrumentation and measurement procedures . . . . .	79
5.2.2	Processing model . . . . .	80
5.2.3	Clinical studies . . . . .	81
5.3	Concluding remarks . . . . .	82
<b>A</b>	<b>Optical properties from literature</b>	<b>83</b>
<b>B</b>	<b>Phantom recipe</b>	<b>91</b>
	<b>References</b>	<b>95</b>
	<b>Curriculum Vitae</b>	<b>105</b>



## List of Tables

2.1	Subject characteristics. . . . .	14
2.2	Mean and standard deviation for chromophore concentrations in bones. . . . .	16
2.3	Mean and absolute maximum changes for optical properties and chromophore values between left and right sides within an individual. . . . .	20
2.4	Mean and absolute maximum changes in optical properties and chromophore values between visits. . . . .	24
3.1	Subject and tumor characteristics. . . . .	35
3.2	Median SNR with 10–90 percentiles from average SNR of all measurements as a function of the modulation frequency. . . . .	36
3.3	Median SNR with 10–90 percentiles from average SNR of contralateral normal measurements as a function of the modulation frequency. . . . .	37
3.4	Median SNR with 10–90 percentiles from average SNR of tumor measurements as a function of the modulation frequency. . . . .	38
3.5	Tumor and imaging depths. . . . .	39
4.1	Tissue-mimicking phantom recipes. . . . .	56
4.2	Median and 10 to 90 percentile ranges of optical properties from literature 630–670 nm. . . . .	60
4.3	Optical property test set. . . . .	62
A.1	Bone optical properties. . . . .	84
A.2	Muscle optical properties. . . . .	85

A.3 Lipid optical properties. . . . .	89
---------------------------------------	----

# List of Figures

2.1	(a) Picture of the probe used in clinical measurements with (b) a close-up of the broadband source and detector fibers, laser source fiber bundle, and APD. . . . .	10
2.2	Transparency used to transfer fiducial markers onto the tibia of a normal volunteer. . . . .	11
2.3	Example (a) $\mu_a$ and (b) $\mu'_s$ spectra for the humerus (orange), femur (blue), and tibia (green) from a 25 year old female. . . . .	15
2.4	Concentrations of (a) oxyhemoglobin, (b) deoxyhemoglobin, (c) water, (d) lipids, (e) total hemoglobin, and (f) tissue oxygen saturation for the humerus (orange), femur (blue), and tibia (green). The box shows the interquartile range and the whiskers extend to 1.5 the interquartile range of the lower and upper quartile. . . . .	18
2.5	Comparison of (a) oxyhemoglobin, (b) deoxyhemoglobin, and (c) total hemoglobin concentration for the femur (blue), humerus (orange), and tibia (green). . . . .	21
2.6	Comparison of (a) tissue oxygen saturation, (b) water, and (c) lipids for the femur (blue), humerus (orange), and tibia (green). . . . .	22
2.7	Linear correlation between body fat percentage (%) and DOSI lipid concentration (%) for the (a) femur, (b) humerus, and (c) tibia. . . . .	23

2·8	A 26 year old female measured on four separate days with DOSI. Concentrations of (a) oxyhemoglobin, (b) deoxyhemoglobin, (c) water, (d) lipids, (e) total hemoglobin, and (f) oxygen saturation are shown for the femur (blue), humerus (orange), and tibia (green). . . . .	25
3·1	DOSI imaging depth estimates from the PHD. At a line perpendicular to the tissue surface emanating from the geometric midpoint between the source and detector locations (red dotted line), the peak PHD (black dotted), and the 90%, 50%, and 10% of the peak PHD (black dash-dot, dashed, and solid lines, respectively) are calculated. The inset shows the PHD profile along the midline. . . . .	34
3·2	Median (solid line) and interquartile range (shaded) of $\mu_a$ versus source wavelength obtained at tumor (blue) and contralateral normal (dark blue) locations for six sarcoma patients (a–f). . . . .	41
3·3	Median (solid line) and interquartile range (shaded) of $\mu'_s$ versus source wavelength obtained at tumor (blue) and contralateral normal (dark blue) locations for six sarcoma patients (a–f). . . . .	42
3·4	A 10 year old male with osteosarcoma in the right distal femur was measured with DOSI before neoadjuvant chemotherapy. (a) Diagram of bones in the right knee. The measurement area is the shaded region with the origin being the bottom tip of the patella. (b) Oxygen saturation maps for tumor and contralateral normal tissue. . . . .	43
3·5	Hemoglobin concentrations ( $\mu\text{M}$ ) for tumor (blue) and contralateral normal (dark blue) tissue for six sarcoma subjects (a–f). $\star$ represent a statistical significance between tumor and contralateral normal tissue at $p = 0.05$ . . . . .	44

3·6	Water, lipid, and oxygen saturation (% concentration) for tumor (blue) and contralateral normal (dark blue) tissue for six sarcoma subjects (a–f). $\star$ represent a statistical significance between tumor and contralateral normal tissue at $p = 0.05$ . . . . .	45
4·1	Literature values for $\mu_a$ (a) and $\mu'_s$ (b) for lipid (gold), muscle (green), bone (dark blue). Optical properties from 630–670 nm used for further analysis are shaded in grey. . . . .	59
4·2	The phase and amplitude from the P1 diffusion approximation of the radiative transport equation for optical properties in literature from 630–670 nm for lipid (gold), muscle (green), bone (dark blue), and sarcoma (blue) is shown. Black markers are the test set optical properties defined in 4.3. The implementation of the 3-mm diameter area detector will lower the noise floor (dashed line) and allow a greater range of optical properties to be measured. . . . .	61
4·3	The SNR averaged across modulation frequencies for the 0.5-mm APD (dark blue) and the 3-mm APD (yellow). . . . .	63
4·4	The median SNR at each wavelength for different source-detector (SD) separations for a phantom for the 0.5-mm APD (blue, dark blue, grey) and the 3-mm APD (yellow, orange). . . . .	64
4·5	The median SNR at each wavelength for different source-detector separations for a phantom for the 0.5-mm APD (blue, dark blue, grey) and the 3-mm APD (yellow, orange). . . . .	65
4·6	Bland-Altman plots comparing measurements of $\mu_a$ at (a) 658, (b) 690, (c) 785, (d) 808, (e) 830, and (f) 850 nm. The mean (solid line) and $\pm 1.96$ standard deviations (dashed lines) of the data are shown. . . . .	66

4·7	Bland-Altman plots comparing measurements of $\mu'_s$ at (a) 658, (b) 690, (c) 785, (d) 808, (e) 830, and (f) 850 nm. The mean (solid line) and $\pm 1.96$ standard deviations (dashed lines) of the data are shown. . . .	67
4·8	Proportion of photons reaching an underlying sarcoma-like tissue with varying lipid layer thicknesses. Simulations are for a (a) low and (b) high absorbing lipid layer. . . . .	68
4·9	The phase and amplitude from the P1 diffusion approximation of the radiative transport equation for optical properties in sarcoma test set at 22 (gold), 28 (green), 34 (blue), and 40 mm (dark blue) source-detector separation. The noise floor for the 0.5-mm APD (solid line) and the 3-mm APD (dashed line) are shown for reference. . . . .	70
4·10	3-mm APD SNR for sarcoma-like phantoms at wavelengths (a) 658, (b) 690, (c) 785, (d) 808, (e) 830, and (f) 850 nm at source-detector separations from 34–88 mm. . . . .	71
4·11	Designed probe housing for 3-mm APD. . . . .	72
B·1	Recipes (line) with a 95% confidence interval for silicone tissue-mimicking with specific (a) $\mu_a$ and (b) $\mu'_s$ values at 658 nm. . . . .	92

## List of Abbreviations

2D	.....	two-dimensional
3D	.....	three-dimensional
ADC	.....	analog to digital converters
ANOVA	.....	analysis of variance
ANSI	.....	American National Standards Institute
APD	.....	avalanche photodiode
AU	.....	arbitrary units
BOTLab	.....	Biomedical Optical Technologies Lab
dDOSI	.....	digital diffuse optical spectroscopic imaging
DDS	.....	direct digital synthesizers
DOS	.....	diffuse optical spectroscopic
DOSI	.....	diffuse optical spectroscopic imaging
DW	.....	diffuse weighted
FDG PET/CT	.....	Fluorine 18 fluorodeoxyglucose positron emission tomography/computed tomography
H <sub>2</sub> O	.....	water
HbO <sub>2</sub>	.....	oxyhemoglobin
HHb	.....	deoxyhemoglobin
HSD	.....	honestly significant difference
Hz	.....	hertz
L	.....	liter
Max	.....	Maximum
MCML	.....	Monte Carlo multi layered
MHz	.....	megahertz
MRI	.....	magnetic resonance imaging
NIR	.....	near infrared light
P1	.....	
PHD	.....	photon hitting density
PIP	.....	proximal interphalangeal
PMT	.....	photomultiplier tube
SNR	.....	signal-to-noise ratio
StO <sub>2</sub>	.....	tissue oxygen saturation
THC	.....	total hemoglobin

TiO <sub>2</sub>	.....	titanium dioxide
TOI	.....	tissue optical index
<i>V</i>	.....	volume
cm	.....	centimeter
deg	.....	degrees
g	.....	grams
μM	.....	micromolar
μm	.....	micrometer
min	.....	minute
mL	.....	milliliter
mm	.....	millimeter
n	.....	number
nm	.....	nanometer
p	.....	p-value
s	.....	second
x	.....	distance
y	.....	distance
z	.....	depth
α	.....	significance level
<i>n</i>	.....	index of refraction
<i>NA</i>	.....	numerical aperture
θ	.....	angle
μ <sub>a</sub>	.....	absorption coefficient
μ' <sub>s</sub>	.....	reduced scattering coefficient
ρ	.....	distance



## Chapter 1

# Background and significance

### 1.1 Sarcomas

#### 1.1.1 Epidemiology and diagnosis

Sarcomas are malignant tumors of the connective tissue, such as bone, muscle, and cartilage (Klein and Siegal, 2006). While they represent less than 1% of cancers in the United States (National Cancer Institute, b; National Cancer Institute, a), they comprise 12% of all childhood cancers (Howlander et al., 2016). Osteosarcoma and Ewing sarcoma are the two most common bone malignancies in children and young adults (National Cancer Institute, b; Mirabello et al., 2009), representing 5% of all pediatric cancers (Howlander et al., 2016). Soft tissue sarcomas are another common malignancy and represent 6% of all pediatric cancers (Howlander et al., 2016).

Peak incidence of bone cancer is in the second decade of life (National Cancer Institute, b; Mirabello et al., 2009), occurring in males slightly more often than in females (National Cancer Institute, b; National Cancer Institute, a; Mirabello et al., 2009). Bone cancers, especially osteosarcomas, occur most frequently in the long bones of the body (Klein and Siegal, 2006; Mirabello et al., 2009; Bielack et al., 2002). Sarcoma symptoms include pain and swelling at the bone and joint, often accompanied by a soft tissue mass (Bielack et al., 2002; Davis et al., 1994; Biermann et al., 2013; Bernstein et al., 2006). After imaging studies, such as MRI, the diagnosis is confirmed by a biopsy (Hosalkar and Dormans, 2004).

### 1.1.2 Treatment and survival

Before 1970, amputation was the primary treatment for sarcomas (Hosalkar and Dormans, 2004; Link et al., 1986). Despite local control, the overall survival at 5 years was less than 20% (Link et al., 1986; Uribe-Botero et al., 1977; Dahlin and Coventry, 1967). Thus all patients are assumed to have subclinical metastasis (Klein and Siegal, 2006; Hosalkar and Dormans, 2004; Link et al., 1986). With the introduction of chemotherapy in the early 1970's, 5 year disease-free survival and overall survival increased from less than 20% to almost 70% (National Cancer Institute, b; National Cancer Institute, a; Mirabello et al., 2009; Link et al., 1986; Uribe-Botero et al., 1977; Dahlin and Coventry, 1967).

Sarcomas are now treated as a systemic disease using multiagent neoadjuvant (presurgical) chemotherapy followed by surgery and postoperative chemotherapy (Hosalkar and Dormans, 2004; Meyers et al., 1992; Mehren et al., 2014). Chemotherapy drugs such as Adriamycin (doxorubicin), cisplatin, methotrexate, and ifosfamide are delivered cyclically for a few months before surgical resection or amputation (Carrle and Bielack, 2006; The ESMO/European Sarcoma Network Working Group, 2014; Wittig et al., 2002). Despite these advances in treatment, disease-free survival and overall survival for localized disease have stagnated for the last 40 years, remaining at approximately 70% survival (National Cancer Institute, b; National Cancer Institute, a; Mirabello et al., 2009; Link et al., 1986; Uribe-Botero et al., 1977; Dahlin and Coventry, 1967).

Even though neoadjuvant chemotherapy and adjuvant chemotherapy have similar disease-free survival rates (Meyers et al., 1992), neoadjuvant chemotherapy is the standard of care (Marina et al., 2004). Neoadjuvant chemotherapy is favored because it gives early systemic treatment for subclinical microscopic metastases (Rosen et al., 1979), improves the quality of the surgical margin (Hosalkar and Dormans, 2004),

increases limb-saving surgeries (Bielack et al., 2002; Hosalkar and Dormans, 2004; Marina et al., 2004; Bacci et al., 2005), and assesses chemotherapy response at time of surgery (Marina et al., 2004).

### **1.1.3 Prognostic markers**

The only clinically accepted prognostic marker is histologic response to neoadjuvant chemotherapy (Bieling et al., 1996). Good histologic response is typically defined as having greater than 90% tumor-cell necrosis at time of surgery and is correlated with longer disease-free survival, event-free survival, and overall survival rates (Meyers et al., 1992; Hosalkar and Dormans, 2004; Provisor et al., 1997; Wunder et al., 1998). Unfortunately, this biomarker can only be determined at the time of surgery, weeks or months after intensive chemotherapy (Bacci et al., 2003; Bielack et al., 2002; Hauben et al., 2002).

At the time of surgery, approximately 40–70% of patients have a poor histologic response (Hauben et al., 2002; Asha et al., 2012). For patients with a poor response, salvage therapy modifies the post-surgery chemotherapy regimen in hopes of better patient outcomes. Since an initial success in the 1980's (Rosen et al., 1979), salvage therapy has been unsuccessful at improving the outcome of poor responders (Meyers et al., 1992; Carrle and Bielack, 2006; Provisor et al., 1997; Winkler et al., 1988; The ESMO/European Sarcoma Network Working Group, 2014). The delayed evaluation of treatment response could be a reason for continued poor outcomes (Asha et al., 2012), emphasizing the need to identify poor responders early in treatment before surgery.

Other prognostic markers, such as tumor location (Mirabello et al., 2009; Bielack et al., 2002; Meyers et al., 1992), initial tumor size (Bielack et al., 2002; Bieling et al., 1996), intratumoral microvessel density (Kreuter et al., 2004), disease stage (Mirabello et al., 2009), and metastasis (Bielack et al., 2002), have been proposed, but

they remain unverified and cannot be used as a clinical recommendation. Similarly, the molecular marker alkaline phosphatase has been suggested (Meyers et al., 1992; Bacci et al., 2005; Levine and Rosenberg, 1979; Bacci et al., 2006), but it also lacks validation and loses its prognostic significance in multivariate analyses (Bielack et al., 2002; Marina et al., 2004).

Imaging techniques have been mostly unsuccessful in predicting chemotherapy response in sarcoma (The ESMO/European Sarcoma Network Working Group, 2014; Bajpai et al., 2011; Sanchez et al., 1990). Due to the bony nature of many sarcomas, volumetric changes may not occur despite responding to treatment (Bajpai et al., 2011), rendering many structural imaging techniques unhelpful. For changes to be seen on X-rays, 30–40% of the bone must be destroyed (Hosalkar and Dormans, 2004). Diffuse weighted (DW) MRI has had mixed results detecting tumor viability and it remains unverified (Bajpai et al., 2011; Sanchez et al., 1990; Moffat et al., 2006; Markus Uhl et al., 2006). Recently, the functional imaging techniques FDG PET/CT found that tumor necrosis at time of diagnosis was correlated with pathologic response and mortality (Rakheja et al., 2013). However, these techniques cannot be used for frequent treatment monitoring because of cost, access, and potential harm to the patient from radiation or exogenous contrast agents (Facey et al., 2007; Meertens et al., 2018). Thus, tumor response to chemotherapy remains the best prognostic marker (Bielack et al., 2002; Davis et al., 1994; Meyers et al., 1992; Bacci et al., 2005) for sarcoma and finding a new marker earlier in treatment is a priority.

## **1.2 Diffuse Optical Spectroscopic Imaging**

### **1.2.1 Instrumentation**

Diffuse Optical Spectroscopic Imaging (DOSI) is a noninvasive, nondestructive, non-ionizing, functional imaging technique that holds potential as a new prognostic tool for

sarcoma. DOSI measures quantitative concentrations of functional hemodynamic information (chromophores), such as oxyhemoglobin ( $\text{HbO}_2$ ), deoxyhemoglobin (HHb), water, and lipids. The DOSI system described here was originally designed for breast cancer and has been extensively described (Tromberg et al., 2016; No et al., 2008).

The system is compact and fits on a medical cart, allowing bedside access during chemotherapy. The system acquires both frequency-domain and continuous wave (broadband) measurements. It has a handheld probe that delivers amplitude modulated near-infrared (NIR) light and broadband light to the tissue via 400  $\mu\text{m}$  and 1 mm optical fibers, respectively. Light levels delivered to the tissue are within ANSI limits for skin exposure.

For the frequency-domain measurements, light from four lasers (659, 689, 781, and 829 nm) is amplitude modulated in a sweep from 50 to 500 MHz and detected by an avalanche photodiode (APD) with a 0.5 mm active area (C5658 with detector S-6045, Hamamatsu Photonics, Hamamatsu, Japan). Broadband light from a tungsten-halogen lamp is detected by an NIR spectrometer (650 to 1000 nm). The APD and the fiber bundle leading to the spectrometer are embedded in the handheld probe.

### **1.2.2 Optical properties and functional hemodynamic information calculations**

DOSI measures broadband absorption by combing frequency-domain and continuous wave measurements. An example of measured amplitude and phase from a frequency-domain measurement taken at a single wavelength. The optical properties, absorption and reduced scattering coefficients ( $\mu_a$  and  $\mu'_s$ , respectively), are calculated from simultaneously fitting calibrated frequency-domain amplitude and phase measurements from 50 to 400 MHz to a P1 diffusion approximation of the radiative transport equation, typically assuming a homogenous, semi-infinite material, although multilayer models have previously been developed (Haskell et al., 1994; Pham et al., 2000).

Broadband absorption is fit and scaled to the frequency-domain absorption measurements (Pham et al., 2000; Bevilacqua et al., 2000; The MathWorks Inc., 2014). Using the broadband absorption and known extinction coefficients (Pope and Fry, 1997; Kou et al., 1993; van Veen et al., 2004; Zijlstra et al., 2000) quantitative concentrations of oxyhemoglobin, deoxyhemoglobin, water, and lipids are calculated using Beer’s Law. In addition, total hemoglobin concentration (THC) and tissue oxygen saturation ( $StO_2$ ) are calculated from oxyhemoglobin and deoxyhemoglobin concentrations.

### **1.2.3 Potential as a prognostic tool**

DOSI has been studied extensively in the context of breast cancer, where it has been shown that functional hemodynamic information measured using DOSI is correlated with pathologic response as early as the first day after the start of neoadjuvant chemotherapy (Ueda et al., 2012; Roblyer et al., 2011; Cerussi et al., 2011). Similar optical biomarkers may exist in sarcoma. Since DOSI does not rely on structural changes, but is sensitive to tumor metabolism and necrosis, it may provide earlier assessments of treatment response than other available methods.

### **1.2.4 Previous diffuse optics work in bone**

Many sarcomas develop in the bone and imaging will need to take place in lipid, muscle, and bone. While previous work has established diffuse optical techniques in breast and muscle, less work has been done in bone (Sandell and Zhu, 2011; Jacques, 2013).

A recent review of optical systems used for measuring human hemodynamic markers in vivo bone tissue identified 19 studies that used NIR spectroscopy (Meertens et al., 2018). Nine studies used continuous wave measurements to detect changes in oxyhemoglobin and deoxyhemoglobin while three studies used multiple lasers to measure hemodynamics. Only one study used frequency-domain NIR spectroscopy. Five

studies used time-resolved NIR spectroscopy. In addition to hemodynamic markers, the time-resolved NIR spectroscopy studies could measure  $\mu_a$  and  $\mu'_s$ . (One study did not describe its NIR spectroscopy system.)

In addition, several groups have measured the optical properties of human bone in vivo using near infrared spectroscopy. The absorption and reduced scattering coefficients of the patella and bones in the index finger were respectively measured using frequency-domain diffuse optical spectroscopy and tomography (Farzam et al., 2013; Xu et al., 2001). With a time resolved transmittance system, the optical properties for the manubrium, forearm, forehead, and calcaneus were measured in transmission (Pifferi et al., 2004; Sekar et al., 2015b; Sekar et al., 2015a). The optical properties for the forehead, tibia, radius, ulna, and greater trochanter of the femur have also been measured with time resolved reflectance spectroscopy (Matcher et al., 1997; Sekar et al., 2015a; Doornbos et al., 1999).

Other near infrared diffuse optical systems have been used to measure the optical properties of ex vivo animal bones such as bovine dry bone matrix (Pifferi et al., 2004), chicken bone (Xu et al., 2001), pig skull (Firbank et al., 1993), horse bone (Ugryumova et al., 2004), and rabbit cartilage (Beek et al., 1997).

### 1.3 Goal of this dissertation

As a NIR system, DOSI is a noninvasive, nondestructive, nonionizing, inexpensive tool for longitudinal hemodynamic measurements. Due to the high density and mineral content of bone, measuring functional hemodynamic information is a challenge (Meertens et al., 2018). This work determines the feasibility of using DOSI in sarcomas.

## Chapter 2

# Characterize the optical properties and hemodynamics of normal volunteers in common sarcoma locations

### 2.1 Introduction

The DOSI instrumentation was designed for pliable and optically transparent breast tissue. This section establishes the feasibility of using DOSI to measure the angular, rigid, and highly attenuating tissues at bony locations that are common to sarcomas. For the first time, the optical properties and functional hemodynamic information from adult and pediatric normal volunteers will be characterized using diffuse optics at the at the medial distal humerus, distal femur, and proximal tibia.

### 2.2 Methods

#### 2.2.1 Subject eligibility and enrollment

Any volunteer was eligible as a subject for the normal volunteer study. A power analysis based on previous exploratory DOSI studies in breast cancer and preliminary data calculated a target sample size of 25 subjects. The power analysis aimed to detect a 27% difference in mean tissue optical index (defined as deoxyhemoglobin\*water/lipids) between responders and nonresponders with 80% power and a significance level of  $\alpha=0.05$ , assuming equal sample sizes in responders and nonresponders with an expected 25% standard deviation within groups.



Normal volunteer subjects were recruited in an effort to match expected sarcoma patient population demographics. Almost 60% of the sarcoma population is male (National Cancer Institute, a; National Cancer Institute, b), so the target accrual for males and females is 15 and 10, respectively. Informed consent was obtained from all subjects. Minors (<18 years) gave assent to the best of their ability to understand, and their parent or guardian gave written informed consent. This project was approved by the Institutional Review Board at Boston University.

### **2.2.2 DOSI instrumentation**

The DOSI system used to measure volunteers is a benchtop system the Biomedical Optical Technologies Lab (BOTLab) considers to be a “gold standard” for its measurements. Unlike the clinical system which is portable (Section 1.2.1), this system spans an optical table.

Like the clinical system, the benchtop system acquires both frequency-domain and continuous wave measurements. Unlike the clinical system, the frequency-domain measurements use light from six lasers (658, 690, 785, 808, 830, and 850 nm) instead of four lasers. Optical fibers deliver amplitude modulated NIR light and broadband light to the tissue via 400  $\mu\text{m}$  and 1 mm optical fibers, respectively. The light is amplitude modulated in a sweep from 50 to 500 MHz and is detected by a 0.5-mm active area APD (C5658 with detector S-6045, Hamamatsu Photonics, Hamamatsu, Japan). Continuous wave light from a tungsten-halogen lamp is detected by an NIR spectrometer (650 to 1000 nm). Light levels delivered to the sample are within ANSI limits for skin exposure. Figures 2-1 shows a picture of the probe sources and detectors. All measurements for this study were taken with a source-detector separation of 28 mm.

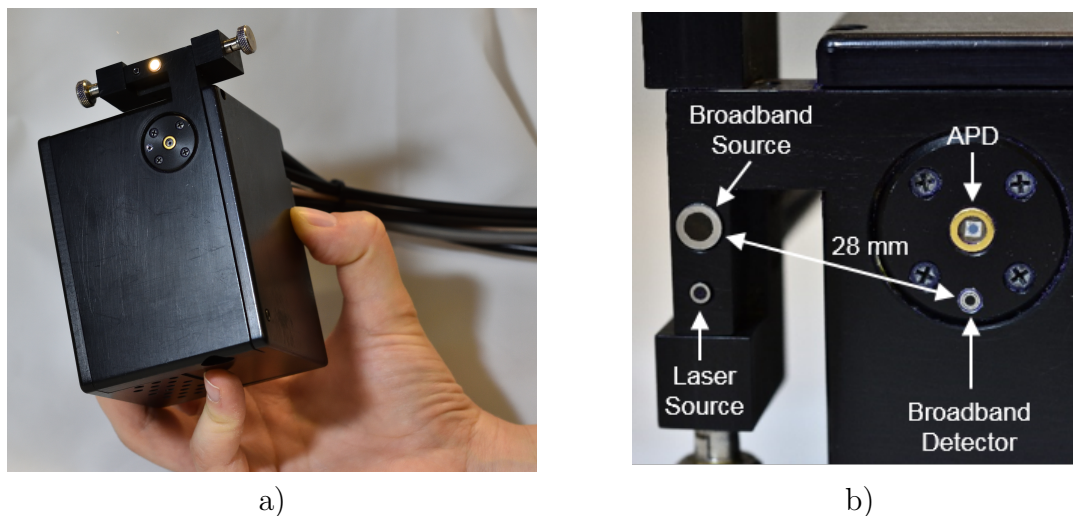


**Figure 2-1:** (a) Picture of the probe used in clinical measurements with (b) a close-up of the broadband source and detector fibers, laser source fiber bundle, and APD.

### 2.2.3 Imaging procedures

A standard DOSI measurement procedure originally developed for breast and used for several prior published studies was modified for measurements taken in this study (Cerussi et al., 2011; Tromberg et al., 2016). In this study, measurements were made on the left and right medial distal humerus, distal femur, and proximal tibia.

The corners of 1 square cm grid were transferred onto the skin surface at each location using a transparency and nonpermanent surgical marker. All subjects were measured 4 cm from the medial epicondyle of the humerus, on the medial epicondyle of the femur, and 3 cm from the distal end of the patella. As seen in Figure 2-2, the transparency included distinctive features to serve as a reference, e.g. freckles, moles, scars, and bone landmarks. The landmarks helped to identify the same region of interest for any subsequent measurements.

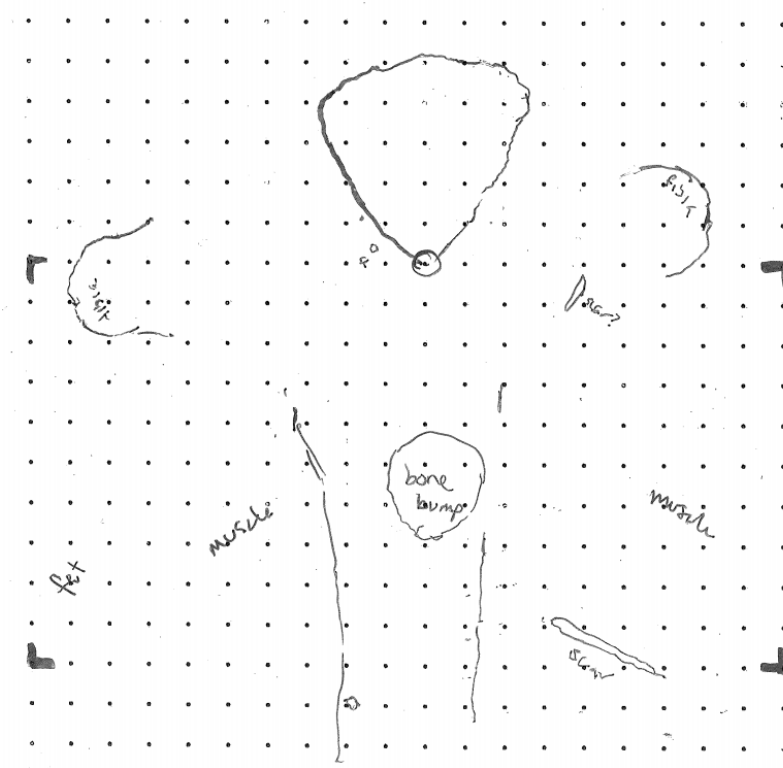


**Figure 2.2:** Transparency used to transfer fiducial markers onto the tibia of a normal volunteer.

An operator scanned the handheld probe over the square, taking a point measurement at each dot. Data was processed using the methods described in Section 1.2.2 to calculate optical properties and concentrations of oxyhemoglobin, deoxyhemoglobin, water, and lipids.

Each subject in this study had a total of 24 point measurements.

#### 2.2.4 Data quality control

To be included in the dataset, the broadband reduced scattering coefficient must follow a power law and chromophore values must be physiological (i.e. lipid and water percentage cannot exceed 100%). Data that do not meet these requirements were excluded. Any points over tattoos were also excluded.

### **2.2.5 Estimates of body fat percentage**

Estimates of body fat percentage were calculated by measurements of subcutaneous tissue. Using the Lange Skinfold Caliper (Beta Technology, Santa Cruz, California), skinfold measurements were taken at the biceps, triceps, subscapular, and the suprailiac. The sum of the four skinfold measurements were converted to the equivalent fat content as a percentage of body weight using the Lange Skinfold Caliper Operators Manual (Beta Technology, 2008). For subjects <18, only triceps and subscapular skinfold measurements were taken.

### **2.2.6 Comparison of optical properties and chromophore concentrations**

The two-sided Mann-Whitney test was used to statically compare the distribution of point measurements for left and right tissues at each bone location. ANOVA with Tukey's honestly significant difference (HSD) post hoc test compared differences between the humerus, femur, and tibia. Pearson's correlation coefficient quantified the relationship between DOSI lipid concentrations at a bony location and the body fat percentage.

A subset of individuals were measured multiple times over the course of 3 weeks to quantify the variation within an individual. Tukeys HSD compared differences in means that were designated significant by ANOVA. The average and absolute maximum change from the first visit was calculated.

All statistics were calculated using SciPy 1.0.0 in Python version 2.7.13 (Python Software Foundation, 2015; Jones et al., 2001).

## **2.3 Results**

### **2.3.1 Subject enrollment**

Twenty four subjects were enrolled in the study. One subject was not analyzed due to data processing issues. The subject characteristics are shown in Table 2.1. Subjects are identified by the study number with a three digit identifier in the form 3367-000. The protocol is approved for several studies, so identifiers are not necessarily sequential and the first subject number is 3367-012.

**Table 2.1:** Subject characteristics.

Variable	Enrolled
Subjects	24
Adult ( $\geq 18$ years)	22
Minor ( $<18$ years)	3
Age (years)	
Median	27
Range	[4–46]
Sex	
Male	12
Female	12
Race	
White	10
Black/African-American	1
Asian	9
Multiracial	1
Unknown	3
Ethnicity	
Hispanic or Latino	4
Not Hispanic or Latino	20
Adult body fat	
Median (%)	21.4
Range (%)	[10.5–27.8]
Off the chart (n)	1
Unknown (n)	1

### 2.3.2 Optical properties

Examples of  $\mu_a$  and  $\mu'_s$  spectra for the humerus, femur, and tibia from a 25 year old female are shown in Figure 2-3. Though the magnitude of  $\mu_a$  differs, the spectra have the same shape from 650–900 nm (Figure 2-3a). At 980 nm there is a water

absorption peak and there are notable differences in the magnitude of  $\mu_a$ , with the tibia being most absorbing and the femur the least. For this individual, the scattering slope and amplitude of  $\mu'_s$  is different for each bone (Figure 2.3b). At the population level, the scattering slope of the humerus, femur, and tibia are statistically different from each other; there are no differences in scattering amplitude.

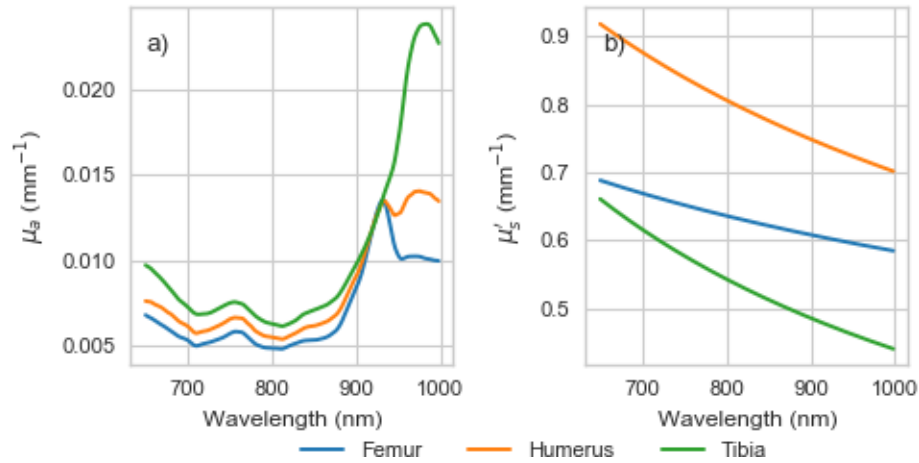


**Figure 2.3:** Example (a)  $\mu_a$  and (b)  $\mu'_s$  spectra for the humerus (orange), femur (blue), and tibia (green) from a 25 year old female.

Optical properties were compared for measurements taken on the left and right tissues at each bony location for each subject. The humerus had the most subjects with statistical differences between the sides—9 subjects had a difference in the scattering slope and the scattering amplitude, while an additional 2 had differences in the scattering amplitude. Five subjects had differences in the scattering amplitude and slope in the femur. In the tibia, 2 subjects had a difference in the scattering amplitude and slope, with an additional 2 had differences in the scattering amplitude.

Comparing bones within an individual, there were few statistical differences in the scattering amplitude parameter. Only 4 subjects had a difference between the humerus and tibia, and 2 subjects had a difference between the femur and tibia. None had a statistical difference between the humerus and femur. The subjects with

statistical differences were the oldest and youngest participants. Scattering slope had more differences between the bones. Fifteen subjects had differences between the tibia and humerus, 11 had differences between the tibia and femur, and 6 had differences between the femur and humerus.

### 2.3.3 Chromophore concentrations

The mean and standard deviation of oxyhemoglobin, deoxyhemoglobin, water, lipids, total hemoglobin, and tissue oxygen saturation are reported for each bone in Table 2.2. For the humerus, femur, and tibia, the mean and standard deviation of oxyhemoglobin was respectively 35.4 (16.8), 31.6 (16.3), and 27.9 (11.9)  $\mu\text{M}$  while deoxyhemoglobin was respectively 11.7 (3.3), 10.5 (3.1), and 10.9 (3.1)  $\mu\text{M}$ . Mean water concentration for the humerus, femur, and tibia was respectively 12.8 (3.1), 15.2 (3.8), and 27.7 (12.1) % while lipid concentration was 37.3 (14.0), 29.4 (14.3), and 25.2 (10.0) %.

**Table 2.2:** Mean and standard deviation for chromophore concentrations in bones.

	Humerus	Femur	Tibia
HbO <sub>2</sub> ( $\mu\text{M}$ )	35.4 (16.8)	31.6 (16.3)	27.9 (11.9)
HHb ( $\mu\text{M}$ )	11.7 (3.3)	10.5 (3.1)	10.9 (3.1)
Water (%)	12.8 (3.1)	15.2 (3.8)	27.7 (12.1)
Lipids (%)	37.3 (14.0)	29.4 (14.3)	25.2 (10.0)
THC ( $\mu\text{M}$ )	47.1 (19.1)	42.1 (18.2)	38.9 (12.9)
StO <sub>2</sub> (%)	73.1 (6.0)	72.7 (7.9)	69.8 (9.5)

The distribution of chromophores for each bone is shown in the boxplots of Figure 2-4. The humerus, femur, and tibia are statistically different from each other in water and lipid concentrations (Figure 2-4c–d). The humerus is different in total hemoglobin concentration (Figure 2-4e) while the tibia is different in tissue oxygen



saturation (Figure 2·4f). The humerus and tibia statistically differ in oxyhemoglobin (Figure 2·4a) while the humerus and femur differ in deoxyhemoglobin (Figure 2·4b).

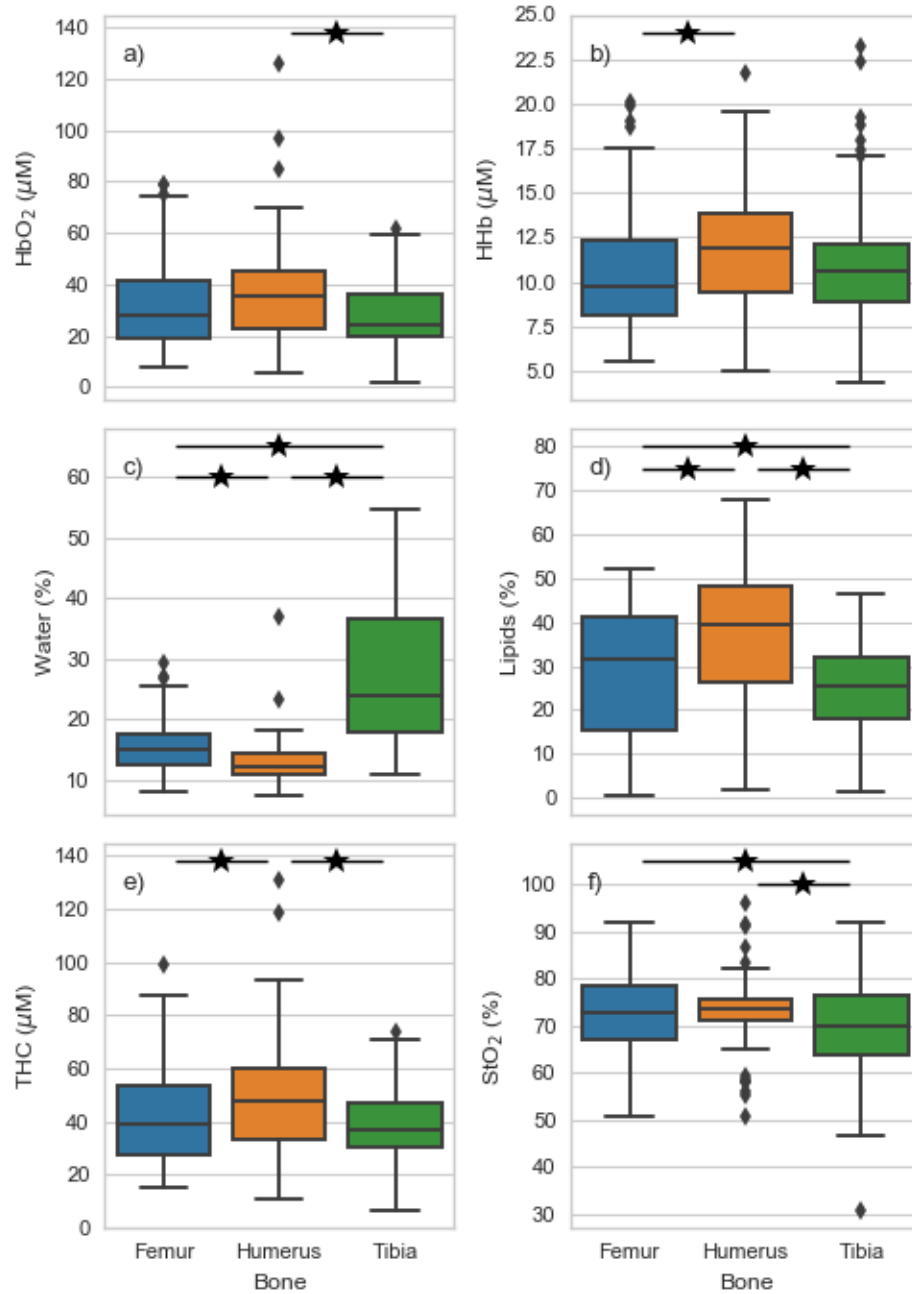


**Figure 2-4:** Concentrations of (a) oxyhemoglobin, (b) deoxyhemoglobin, (c) water, (d) lipids, (e) total hemoglobin, and (f) tissue oxygen saturation for the humerus (orange), femur (blue), and tibia (green). The box shows the interquartile range and the whiskers extend to 1.5 the interquartile range of the lower and upper quartile.

Differences in chromophore concentrations were compared between left and right tissues. At the population level, only water is significantly different between right and left sides at the femur ( $p = 0.003$ ). Within individuals, of the 24 subjects, 21 had some statistical difference in chromophore concentration between the left and right humerus. The most common differences occurred in oxyhemoglobin ( $n = 16$ ) or water ( $n = 15$ ). The least common chromophore to be statistically different was deoxyhemoglobin ( $n = 7$ ). Seventeen subjects had statistical differences in the femur. Water was the most frequently statistically different chromophore for subjects ( $n = 12$ ). Deoxyhemoglobin ( $n = 5$ ) and lipid ( $n = 5$ ) were the least frequently significant. The left and right tibia were most similar for subjects, with only 13 individuals having some statistical difference. Oxyhemoglobin was the most frequently statistically different ( $n = 5$ ), while lipid ( $n = 1$ ) and tissue oxygen saturation ( $n = 1$ ) were the least frequently different.

The mean and absolute maximum changes for optical properties and chromophore values between left and right sides within an individual are shown in Table 2.3. With the exception of  $\mu'_s$  amplitude, the average mean difference is close to 0. The absolute maximum change of an individual for the  $\mu'_s$  slope was largest in the humerus and smallest in the femur. The humerus had the largest maximum change in oxyhemoglobin, deoxyhemoglobin, and total hemoglobin concentration. The tibia had the smallest maximum change in oxyhemoglobin and total hemoglobin concentration while the femur had the smallest maximum change in deoxyhemoglobin. Water and tissue oxygen saturation had the smallest maximum changes in the femur. Maximum changes in lipids were largest in the humerus and smallest in the tibia.

**Table 2.3:** Mean and absolute maximum changes for optical properties and chromophore values between left and right sides within an individual.

	Humerus		Femur		Tibia	
	Mean	Max	Mean	Max	Mean	Max
$\mu'_s$ slope ( $\text{mm}^{-1}$ )	0.1	2.0	0.0	0.4	0.0	1.0
$\mu'_s$ amplitude	-2.86E7	-5.72E8	-4.56E4	-1.01E6	-1.20E5	-2.61E6
HbO <sub>2</sub> ( $\mu\text{M}$ )	-1.2	47.3	-0.6	26.3	-1.0	12.3
HHb ( $\mu\text{M}$ )	0.5	10.5	0.1	3.7	0.8	6.9
Water (%)	-1.1	21	1.5	10.5	1.7	22.3
Lipids (%)	-2.0	31.5	2.3	23.5	0.1	10.9
THC ( $\mu\text{M}$ )	-0.9	36.8	-0.5	26.1	-0.2	14.8
StO <sub>2</sub>	-0.3	13.1	0.0	8.1	-1.7	16.3

Within an individual, differences between the humerus, femur, and tibia were also compared. Statistical differences between bones were found most frequently in the concentration of water (Figure 2-6). Of the 24 subjects, 19 had differences in water between the humerus and tibia, and 15 had differences between the femur and tibia. Only 2 had a statistical difference between the femur and humerus. While the tibia was most different in water concentration, all bones had some differences in lipid concentration (Figure 2-6). The tibia and humerus were different for 13 subjects and the femur and tibia were different for 9 subjects. The fewest differences were in deoxyhemoglobin (Figure 2-5). Nine subjects had a difference between the femur and humerus. Five subjects had a difference between the humerus and tibia, and 4 subjects had a difference between the femur and tibia.

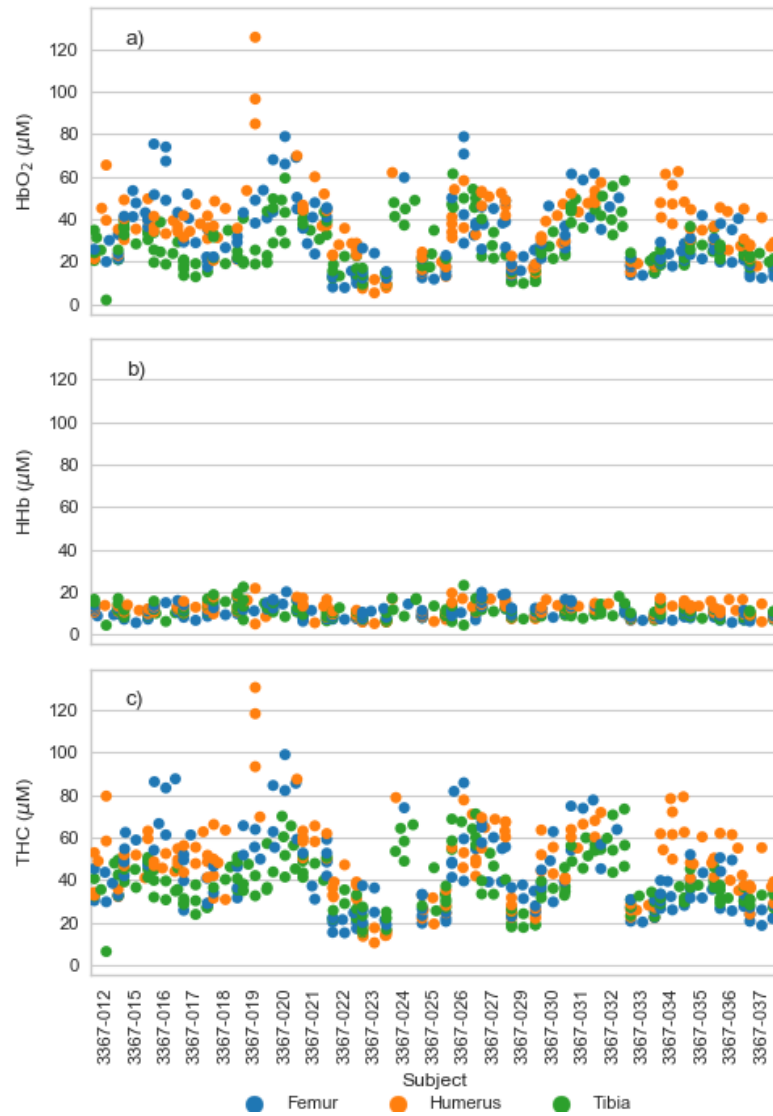


**Figure 2.5:** Comparison of (a) oxyhemoglobin, (b) deoxyhemoglobin, and (c) total hemoglobin concentration for the femur (blue), humerus (orange), and tibia (green).

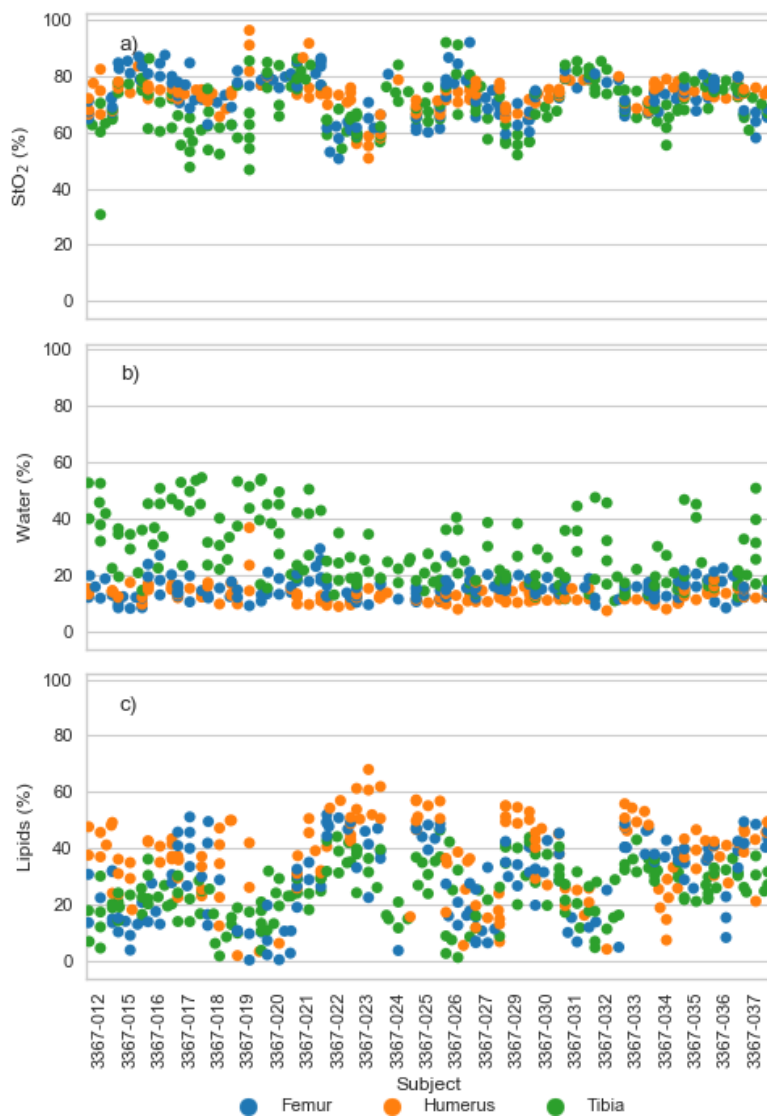


**Figure 2-6:** Comparison of (a) tissue oxygen saturation, (b) water, and (c) lipids for the femur (blue), humerus (orange), and tibia (green).

As shown in Figure 2-7, Pearson's correlation coefficient was calculated for body fat estimates from skin fold measurements and lipid concentration from DOSI measurements. The humerus, femur, and tibia had a Pearson correlation coefficient 0.6 ( $p = 0.007$ ), 0.6 ( $p = 0.01$ ), and 0.7 ( $p = 0.001$ ), respectively. The p-value indicates the probability of an uncorrelated system producing data set that has a Pearson correlation at least as extreme as the one computed from the body fat estimate and lipid

concentration (Jones et al., 2001).

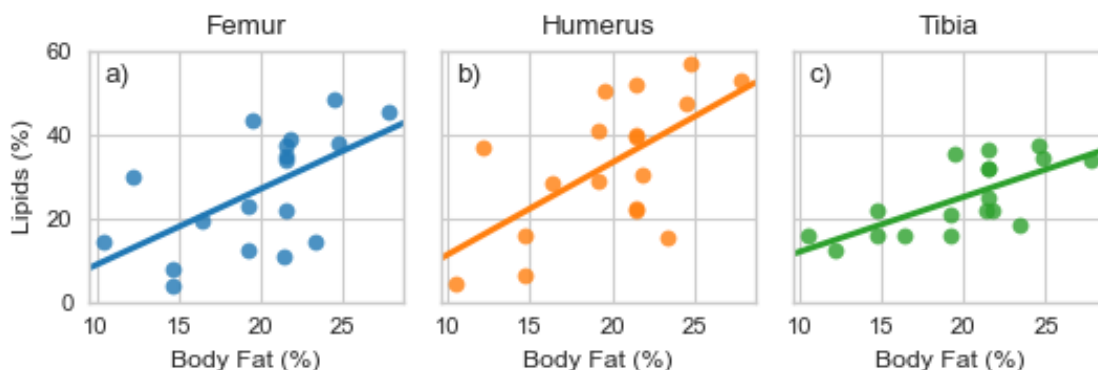


**Figure 2.7:** Linear correlation between body fat percentage (%) and DOSI lipid concentration (%) for the (a) femur, (b) humerus, and (c) tibia.

Optical properties and chromophore values for each bone were compared for adult and pediatric populations. In the humerus, the only statistically difference was in the scattering slope. The tibia and femur both had statistical differences in deoxyhemoglobin and tissue oxygen saturation. The femur also had a statistical difference in water concentration.

### 2.3.4 Longitudinal measurements

A 26 year old female was measured four times in two weeks, as shown in Figure 2.8. Three of the four measurements were at the same time of day. The mean and standard deviation from the four measurements of oxyhemoglobin, deoxyhemoglobin, water, lipids, total hemoglobin, and tissue oxygen saturation for the humerus was 43.4 (9.6)  $\mu\text{M}$ , 14.5 (2.6)  $\mu\text{M}$ , 13.5 (2.1) %, 30.0 (9.2) %, 58.0 (12.1)  $\mu\text{M}$ , and 74.7 (1.7) %. For the femur, the chromophore concentrations are 48.3 (16.1)  $\mu\text{M}$ , 14.7 (3.2)  $\mu\text{M}$ , 17.6 (3.5) %, 20.5 (10.4) %, 63.0 (17.9)  $\mu\text{M}$ , and 75.6 (5.3) %. For the tibia, the chromophore concentrations are 28.1 (5.4)  $\mu\text{M}$ , 10.8 (2.2)  $\mu\text{M}$ , 32.4 (12.8) %, 24.0 (6.7) %, 38.8 (5.7)  $\mu\text{M}$ , and 71.9 (5.7) %, respectively.

The mean and maximum change from the four measurements are shown in Table 2.4. The femur has the largest average and maximum changes for the scattering slope and amplitude while the humerus has the least. For chromophores, the largest mean and maximum change occurred in the same bone. The greatest mean and maximum changes in oxyhemoglobin, deoxyhemoglobin, and total hemoglobin concentration were in the femur, humerus, and femur respectively. The smallest changes in hemoglobin concentrations were in the tibia. The changes for water are the largest for tibia and the smallest for lipids. For lipids, the largest changes are in the humerus and the smallest are in the femur. The femur has the largest changes in tissue oxygen saturation and the smallest changes are in the humerus.

**Table 2.4:** Mean and absolute maximum changes in optical properties and chromophore values between visits.

	Humerus		Femur		Tibia	
	Mean	Max	Mean	Max	Mean	Max
$\mu'_s$ slope ( $\text{mm}^{-1}$ )	-0.2	0.2	-0.6	0.8	-0.2	0.4
$\mu'_s$ amplitude	39.2	43.8	24599.6	24681.6	7271.3	19322.9
HbO <sub>2</sub> ( $\mu\text{M}$ )	-9.7	13.5	17	26.3	-1.8	2.9
HHb ( $\mu\text{M}$ )	-2.8	3.8	-2.1	2.3	0.4	1.4
Water (%)	2.8	3.7	3.6	5.5	8.7	13
Lipids (%)	13.3	16.2	1.6	1.8	1	4.6
THC ( $\mu\text{M}$ )	-12.5	17.3	15	24.3	-1.3	3.7
StO <sub>2</sub>	-0.3	1.4	8.6	13.3	-2.7	4.4



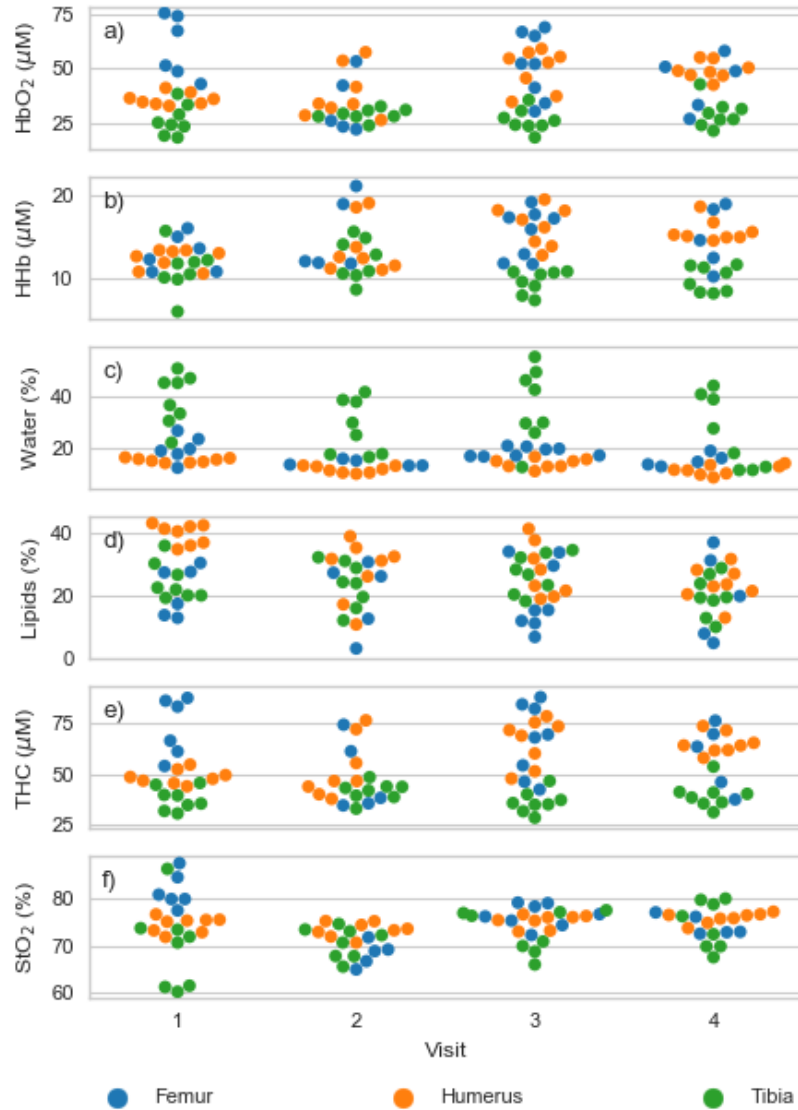


**Figure 2-8:** A 26 year old female measured on four separate days with DOSI. Concentrations of (a) oxyhemoglobin, (b) deoxyhemoglobin, (c) water, (d) lipids, (e) total hemoglobin, and (f) oxygen saturation are shown for the femur (blue), humerus (orange), and tibia (green).

Left and right sides of of the body was compared for each bone. On the first visit, the humerus had statistical differences in scattering slope and amplitude, oxyhe-

moglobin, water, lipids, and tissue oxygen saturation. The only statistical difference in the tibia was scattering amplitude. The femur had no statistical differences in optical properties or chromophores.

Comparisons between bones were made for each visit. On the first visit, the femur and humerus statistically differed in scattering slope, oxyhemoglobin, deoxyhemoglobin, lipids, and tissue oxygen saturation. The femur and tibia differed in oxyhemoglobin, total hemoglobin concentration, and tissue oxygen saturation. The humerus and tibia differed in scattering slope, oxyhemoglobin, lipids, and total hemoglobin concentration. No bones differed from each other in scattering amplitude of deoxyhemoglobin.

Chromophore concentrations were compared for different bones on different visits. The tibia was the most similar from visit to visit, having only 1 statistical difference in deoxyhemoglobin between visits 2–3. The humerus statistically differed in lipid and water concentrations over the visits. Lipid content differed once between days 2–3. Water concentration differed between visits 1–3, 1–4, 2–3, and 2–4.

## 2.4 Discussion

This normal volunteer study provides the first DOSI measurements of the distal humerus, distal femur, and proximal tibia. These results suggest that DOSI is capable of measuring and characterizing bony tissues.

The bones measured in this study presented a large variation of chromophore concentrations between subjects and within subjects. Compared to literature values for bony anatomic locations, the chromophore values in this study resemble chromophore measurements of the manubrium (Sekar et al., 2015a).

Thus far, the only frequency-domain DOS bony measurements have been in the patella (Farzam et al., 2013) where water concentration was assumed to be 15%, and

the total hemoglobin concentration and tissue oxygenation was measured to be  $18\pm 4$   $\mu\text{M}$  and  $65\pm 9\%$ , respectively. From those values, it can be calculated that oxyhemoglobin has a concentration of  $11.7$   $\mu\text{M}$  and deoxyhemoglobin has concentration of  $6.3$   $\mu\text{M}$ . The chromophore values for water, oxyhemoglobin, and deoxyhemoglobin for the patella (Farzam et al., 2013) are all lower than the mean chromophore concentrations measured in this study.

Another study used a diffuse optical time resolved transmittance system to measure chromophores for the proximal femur (trochanter), distal and proximal radius, distal and proximal ulna, and calcaneus (Sekar et al., 2015b). Once again, chromophore measurements are very different, even when comparing the proximal femur to the distal femur. Of the bony locations measured in Sekar et. al., the proximal ulna is most similar to chromophores reported in Table 2.2. In general, the most similar chromophore is water concentration ( $17.4\%$  (Sekar et al., 2015b) compared to  $15.2\%$ ), while the lipid concentrations are much higher and the oxyhemoglobin, deoxyhemoglobin, and total hemoglobin concentrations are lower than the results reported in Table 2.2. Sekar et. al. included collagen and a background variable as additional chromophores which could contribute to some of the differences.

Few studies report means and standard deviations for both sides of the body or for variation within an individual over time. With the exception of tissue oxygen saturation, standard deviations of chromophores for normal tissue were greater than those reported for normal tissue in a 57 person breast cancer study (Cerussi et al., 2006). Generally speaking, the boniest locations had the most symmetry within an individual. Statistically the humerus and tibia are most different from each other.

#### **2.4.1 Limitations**

There are several limitations in this study. Subject enrollment may be one: bone cancers predominantly affect children, however, minors only represented  $12\%$  of the

enrolled subjects. While sample sizes are small and there is such variability in the data, more pediatric subjects would need to be measured to know if there are differences in chromophore concentrations between the populations. This study serves as the first documentation of the optical characterization of these sites.

The measurement locations are a potential limitation. Sarcomas are diverse diseases that can form anywhere in the body. This study chose to focus on three of the most common anatomic locations that would be expected to present in a clinical setting—the distal humerus, distal femur, and proximal tibia account for 66% of osteosarcoma locations (Bielack et al., 2002). While measurement points are aligned to bones and bony landmarks, the bone depth and underlying tissue structure is unknown for the normal volunteers. Measurements on the humerus and the tibia were taken at an absolute distance from a bony landmark on all volunteers and differences in height and bone length could cause measurement locations to be on different parts of the bone or on different vascular beds (Meertens et al., 2018). Reported optical properties and functional information are an averaged value for the underlying tissues including the tissue of interest (bone).

The next potential limitation includes the choice of chromophores for this work. For this investigation, oxyhemoglobin, deoxyhemoglobin, water, and lipids were fit to measured broadband absorption spectra. In muscular area, myoglobin is a likely contributor to absorption. However, the spectra for myoglobin and hemoglobin are so similar they cannot be separated in this context (Chance et al., 1988). Collagen is also an important component in bone, tendon, cartilage, muscle, and skin (Lodish et al., 2000) and several groups have added collagen to their fitting procedures (Pifferi et al., 2004; Zhao et al., 2017; Taroni et al., 2007; Sekar et al., 2015a; Sekar et al., 2015b). The use of collagen as a contributing absorber is relatively recent, and there are limited experimental methods to validate the accuracy of collagen fits. For example,

there are no known reports demonstrating the fabrication of tissue mimicking optical phantoms that incorporate collagen at physiologically relevant concentrations at the volume scales needed for diffuse optical measurements. These reasons contributed to the decision not to include collagen in this work.

An additional potential limitation involves the use of the specific light propagation model. In this work, the P1 diffusion approximation of the Boltzmann transport equation was used. This model assumes a homogeneous optically diffusive media, and the specific boundary conditions used for solving the analytical diffusion equation assume a semi-infinite media (Haskell et al., 1994; Pham et al., 2000). It has not been validated that in vivo measurements of bone, which is porous and highly structured, meet these criteria. It is notable that available NIR absorption spectra of bone indicate that reduced scattering is at least an order of magnitude larger than absorption, providing support that bone is an optically diffusive media (Pifferi et al., 2004). In vivo measurements, however, involve multiple chromophores, layered tissue, and complex microarchitecture.

#### **2.4.2 Conclusions**

The data indicate that bony locations common to sarcomas are amenable to measurement with diffuse optical technologies. Improvements in instrumentation, including the ability to measure more highly absorbing tissue at deeper imaging depths, will be key to collecting future high-quality data sets.

This study demonstrated the ability of DOSI to measure optical properties and functional information at the distal femur, distal humerus, and proximal tibia. DOSI was able to measure healthy tissue, although there was substantial variation among subjects and within subjects. Going forward, technological developments to the probe design would facilitate measurements at these anatomic locations.

## Chapter 3

# Determine if DOSI can detect differences between normal and sarcoma tissue

### 3.1 Introduction

DOSI has not been used previously to evaluate sarcomas. These tumors present several challenges due to the varied anatomic locations where they develop, their depth within tissue, and the substantial differences in tissue composition compared to breast tissue. The goals of this work are to establish that sarcomas can be measured in a variety of anatomic locations, and to quantify DOSI performance for these measurements, including signal levels and imaging depth. Due to the rarity of this disease, these initial measurements represent a crucial step in laying the groundwork for future studies of this patient population, and point towards improvements in DOSI technology likely needed to achieve optimal results. The work presented in this chapter is based on manuscript published by H.M. Peterson, B.H. Hoang, D. Geller, R. Yang, R. Gorlick, J. Berger, J. Tingling, M. Roth, J. Gill, and D. Roblyer in “In vivo, non-invasive functional measurements of bone sarcoma using diffuse optical spectroscopic imaging”, *Journal of Biomedical Optics*, December 2017.

## **3.2 Methods**

### **3.2.1 Subject eligibility and enrollment**

All subjects currently diagnosed with a sarcoma and scheduled to undergo neoadjuvant chemotherapy were eligible. Pregnant females were excluded from the study. Informed consent was obtained from all subjects. Minors (<18 years) gave assent to the best of their ability to understand, and their parent or guardian gave written informed consent. This project was approved by the Institutional Review Boards at Boston University and Montefiore Medical Center.

### **3.2.2 DOSI instrumentation**

The DOSI system used for this study is the same as described in Section 1.2.1. The system is compact and fits on a medical cart, allowing bedside access during chemotherapy. All measurements for this study were taken with a source-detector separation of 28 mm.

### **3.2.3 Imaging procedures**

The measurement procedure used is the same as Section 2.2.3. However, instead of four point measurements, a grid of fiducial markers with 1 cm spacing was transferred onto the skin surface overlying or immediately adjacent to the underlying tumor using a transparency and nonpermanent surgical marker. The transparency included landmarks to identify the same region of interest for any subsequent measurements and to identify the DOSI measurement location on the MRI. An operator scanned the handheld probe over the grid, taking a point measurement at each location. A single point measurement typically took 15 to 30 s, which includes the time it takes to position the probe, ensure good contact between the probe and the skin, and acquire data. After processing the data using the methods described in Section

1.2.2, a 2-D map of chromophore values is created by a linear interpolation between measurement points. A typical measurement area for this study contained an average of 35 individual point measurements on both the tumor and on the contralateral normal tissue.

### **3.2.4 Data quality**

To be included in the dataset, the 90th percentile of the SNR must be greater than 3 for three of the four lasers. It was determined that under this threshold, data were not of sufficient quality for accurate optical property extraction. This requirement ensures that there are at least three data points for the power law fit of  $\mu'_s$ . If the SNR did not meet this condition, the subject was excluded from analysis.

### **3.2.5 Estimates of signal-to-noise ratio**

The experimental signal-to-noise ratio (SNR) was calculated as the raw amplitude divided by a dark measurement. The dark measurement was calculated as the average of five measurements taken on a highly absorbing black phantom. The SNR was calculated for all measurements. For each subject, the median SNR and 10 to 90 percentile range are reported from the average SNR of all measurements as a function of the modulation frequency.

### **3.2.6 Estimates of tumor depth**

All subjects had at least one MRI before the start of treatment. A bone landmark near the DOSI measurement site, clearly identifiable by the operator during the DOSI measurement as well as on the corresponding MRI, was used to correlate DOSI measurement regions on the patient's MRI. More specifically, the distance from a bone landmark to a specific DOSI measurement location was recorded on the DOSI transparency. Using the subject's most recent MRI to the DOSI measurement, this distance



was measured from the same bone landmark along the surface of the skin using the ruler tool in Centricity Enterprise Web (General Electric Company, Chicago, Illinois). Once the DOSI measurement location was found on the MRI, the ruler tool was used to measure the distance perpendicular from the surface of the skin to the edge of the tumor margin, providing an estimate of tumor depth.

### **3.2.7 Estimates of imaging depth**

DOSI imaging depth was estimated from the photon hitting density (PHD) determined at a line perpendicular to the tissue surface emanating from the geometric midpoint between the source and detector locations. The peak PHD and the 90%, 50%, and 10% of the peak PHD are also recorded. A visual representation of the imaging depths is shown in Figure 3-1. The PHD was calculated based on the definition described by Schotland et al., (Schotland et al., 1993) using the Virtual Photonics Simulator (Virtual Photonics Initiative, Irvine, California) with the analytic solution to the standard diffusion approximation and assuming a homogenous media and an isotropic point source. Simulation optical properties were determined from the optical properties of a DOSI measurement that was colocated with MRI for each subject.

### **3.2.8 Comparison of optical properties and chromophore concentrations**

The two-sided Mann-Whitney test was used to statically compare the distribution of point measurements for tumor and contralateral normal tissue using SciPy 1.0.0 in Python version 2.7.13 (Python Software Foundation, 2015; Jones et al., 2001).

## **3.3 Results**

### **3.3.1 Subject enrollment and tumor characteristics**

Nine subjects diagnosed with osteosarcoma (n=6), Ewing's sarcoma (n=2), or round cell sarcoma (n=1) were enrolled in the study. Subjects are identified with a four digit

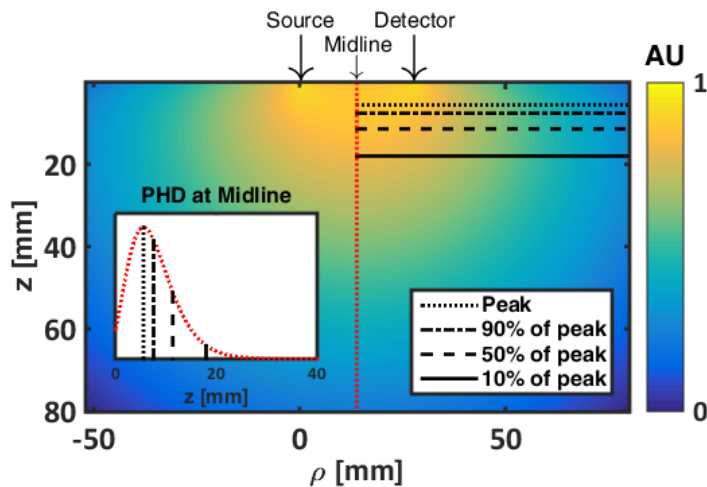


**Figure 3-1:** DOSI imaging depth estimates from the PHD. At a line perpendicular to the tissue surface emanating from the geometric midpoint between the source and detector locations (red dotted line), the peak PHD (black dotted), and the 90%, 50%, and 10% of the peak PHD (black dash-dot, dashed, and solid lines, respectively) are calculated. The inset shows the PHD profile along the midline.

identifier, the first being designated as 1001, the second as 1002, etc. The subject and tumor characteristics of the nine subjects are shown in Table 3.1. Locations measured were the femur ( $n=3$ ), tibia ( $n=3$ ), humerus ( $n=1$ ), ribs ( $n=1$ ), and calf ( $n=1$ ).

Three subjects were excluded from analysis. For one subject diagnosed with osteosarcoma of the distal femur, the tumor location was too sensitive to touch and therefore could not be measured with DOSI. For two other subjects both diagnosed with osteosarcoma of the proximal tibia, the DOSI signal was determined to be too low for analysis, likely because of a highly attenuating tumor. Of the remaining six subjects, five were measured with DOSI before neoadjuvant chemotherapy and one was measured on the 9th day of treatment. Of the six subjects included in the analysis group, five were determined to have a good pathologic response to neoadjuvant chemotherapy, and one had a poor response.

**Table 3.1:** Subject and tumor characteristics.

Variable	Group		
	Analysis	Excluded	All
Subjects	6	3	9
Age (median and range (years))	12 [9–19]	16 [14–30]	14 [9–30]
Sex			
Male	5	3	7
Female	2	0	2
Race			
White	2	0	2
Black/African-American	0	2	2
Hispanic	4	0	4
Other	0	1	1
Site			
Trunk	1	0	1
Extremity	5	3	8
Location			
Left	4	0	4
Right	2	3	5
Disease			
Osteosarcoma	3	3	6
Ewing’s sarcoma	2	0	2
Round cell sarcoma	1	0	1
Median tumor depth (mm)	9.70	5.15	9.40
Percent necrosis (median and range (%))	97 [85–99]	80 [30–95]	95 [30–99]
Pathologic response			
Good	5	1	6
Poor	1	2	3
Mean number of DOSI data points at baseline	73	64	70

### 3.3.2 Estimates of signal-to-noise ratio at baseline

For subjects 1004, 1006, and 1007, poor SNR was achieved at higher modulation frequencies so data was processed from 50–300 MHz. For all subjects, the frequency domain data taken at the shortest wavelength, 659 nm, had the lowest SNR while data taken at 781 nm had the highest SNR, as seen in Table 3.2. For the frequency domain data taken at 659 nm, the median SNR and 10–90 percentiles for subjects 1001, 1002, 1004, 1005, 1006, 1007, 1008, and 1009 were 82 [29, 149], 41 [13, 68], 9 [3, 11], 2 [1, 2], 6 [3, 8], 12 [6, 15], 19 [8, 31], and 2 [1, 2] respectively. The median SNR taken at 781 nm were 296 [118, 441], 165 [71, 247], 58 [41, 68], 16 [11, 20], 59 [38, 74], 67 [48, 79], 99 [44, 145], and 24 [17, 29] respectively for subjects 1001, 1002, 1004, 1005, 1006, 1007, 1008, and 1009.

**Table 3.2:** Median SNR with 10–90 percentiles from average SNR of all measurements as a function of the modulation frequency.

Subject	Wavelength (nm)			
	659	689	781	829
1001	82 [29, 149]	89 [37, 152]	296 [118, 441]	162 [56, 390]
1002	41 [13, 68]	44 [18, 75]	165 [71, 247]	108 [37, 233]
1003	†	†	†	†
1004	9 [3, 11]	13 [9, 17]	58 [41, 68]	41 [20, 67]
1005	2 [1, 2]	3 [2, 3]	16 [11, 20]	15 [8, 26]
1006	6 [3, 8]	10 [6, 13]	59 [38, 74]	46 [23, 81]
1007	12 [6, 15]	19 [13, 24]	67 [48, 79]	39 [21, 64]
1008	19 [8, 31]	28 [12, 47]	99 [44, 145]	51 [19, 110]
1009	2 [1, 2]	3 [2, 4]	24 [17, 29]	20 [11, 36]

† DOSI measurement not taken

Tables 3.4 and 3.3 respectively compare the SNR for tumor and contralateral normal tissue measurements. Tumor measurements had a lower SNR compared to the

contralateral normal measurements for all wavelengths for subjects 1002, 1005, 1007, and 1009. With the exception of SNR measurements at 658 nm, tumor measurements had a lower SNR for subjects 1001 and 1004. For subjects 1006 and 1008, the SNR for tumor and contralateral normal tissues are similar.

To be included in the dataset, the 90th percentile of the SNR must be greater than 3 for three of the four lasers (Section 3.2.4). However, for subjects 1005 and 1009, the tumor measurements did not meet this threshold (Table 3.4), and the subjects were excluded from further analysis.

**Table 3.3:** Median SNR with 10–90 percentiles from average SNR of contralateral normal measurements as a function of the modulation frequency.

Subject	Wavelength (nm)			
	659	689	781	829
1001	77 [28, 134]	91 [40, 146]	316 [132, 454]	177 [63, 417]
1002	43 [14, 72]	47 [19, 79]	179 [77, 267]	116 [39, 250]
1003	†	†	†	†
1004	10 [3, 12]	15 [10, 19]	63 [44, 74]	44 [22, 73]
1005	2 [1, 2]	3 [2, 4]	20 [13, 26]	19 [10, 35]
1006	6 [3, 8]	10 [6, 13]	58 [38, 72]	44 [23, 77]
1007	16 [8, 20]	24 [16, 30]	86 [62, 103]	50 [27, 83]
1008	18 [8, 30]	28 [11, 46]	99 [44, 147]	51 [18, 114]
1009	2 [1, 3]	5 [3, 6]	36 [25, 43]	30 [16, 54]

† DOSI measurement not taken

### 3.3.3 Estimates of tumor and imaging depths at baseline

The tumor depth for each of the subjects is shown in Table 3.5. The peak intensity of the PHD halfway between the source and detector was calculated as 5.8, 5.6, 4.5, and 5.5 mm for subjects 1001, 1002, 1004, and 1006 respectively. As seen in Table

**Table 3.4:** Median SNR with 10–90 percentiles from average SNR of tumor measurements as a function of the modulation frequency.

Subject	Wavelength (nm)			
	659	689	781	829
1001	86 [30, 161]	88 [35, 156]	279 [108, 430]	149 [51, 368]
1002	39 [13, 65]	42 [17, 71]	152 [65, 227]	101 [35, 215]
1003	†	†	†	†
1004	8 [3, 9]	12 [8, 14]	52 [37, 62]	38 [19, 61]
1005	2 [1, 2]	2 [2, 3]	12 [9, 13]	10 [6, 16]
1006	6 [3, 8]	10 [6, 13]	60 [38, 76]	47 [24, 85]
1007	8 [4, 10]	14 [10, 18]	48 [35, 56]	27 [15, 45]
1008	19 [8, 31]	28 [12, 47]	98 [44, 142]	50 [19, 107]
1009	1 [1, 1]	2 [1, 2]	12 [8, 15]	10 [5, 16]

† DOSI measurement not taken

3.5, the estimated peak intensity of the PHD does not reach the tumor for any of the measured subjects. The 50% of the peak PHD was calculated as 12.8, 11.4, 9.8, and 10.8 mm for subjects 1001, 1002, 1004, and 1006 respectively. The 50% of the peak PHD reaches the tumor for subjects 1001 and 1002. For subject 1004, the 50% of the peak PHD is beyond the layer of subcutaneous fat but not within the tumor. However, for three of the four tumors included in the analysis group, 10% of the peak PHD reached the tumor, suggesting some photons are probing the tumor tissue. For subject 1006, the depth at 10% of the peak PHD is within the subcutaneous fat layer.

### 3.3.4 Optical properties at baseline

Optical properties were compared for measurements taken on the tumor and contralateral normal tissues for each subject (Figures 3-2 and 3-3). The median and interquartile ranges in Figures 3-2 and 3-3 show a high degree of variability between subjects and within subjects, and the shape of the absorption and the reduced scat-

**Table 3.5:** Tumor and imaging depths.

Variable	Subject								
	1001	1002	1003	1004	1005	1006	1007	1008	1009
Tumor depth (mm)	5.89	9.40	9.85	9.99	5.15	32.23	7.80	26.70	1.90
Subcutaneous fat thickness (mm)	5.89	5.70	4.46	4.64	5.15	25.04	6.10	11.70	1.90
Imaging depth in tumor (mm)									
Peak intensity	5.8	5.6	†	4.5	‡	5.5	4.90	5.8	‡
90% of the peak PHD	21.4	18.0	†	15.5	‡	16.6	16.1	18.4	‡
50% of the peak PHD	12.8	11.4	†	9.8	‡	10.8	10.3	11.7	‡
10% of the peak PHD	8.2	7.6	†	6.3	‡	7.4	6.8	7.9	‡

† DOSI measurement not taken

‡ DOSI measurement not processed

tering coefficient spectra differ substantially between subjects. Between subjects, the differences in absorption magnitude may be caused by differences in intrinsic properties, tumor size, or tumor depth (Figure 3-2). Within subjects, there are clear differences between tumor and contralateral normal tissues, especially in subjects 1001, 1004, and 1007 (Figure 3-2a, 3-2c, and 3-2e respectively). Subjects 1002, 1006, and 1008 have subtle spectral differences between tumor and normal tissue, with the strongest differences appearing in absorption spectra near 980 nm.

There are statistical differences between tumor and contralateral normal scattering amplitude for subject 1001 ( $p = 0.004$ ) and 1007 ( $p < 0.001$ ). There are statistical differences in scattering slope for subjects 1001 and 1007 ( $p < 0.001$  and  $p < 0.001$  respectively). The scattering slope and amplitude look different for subject 1004 but the p-values are not statistically different ( $p = 0.051$  and  $p = 0.110$ ). In subjects

1002, 1006, and 1008 the scattering amplitude and slope are not statistically different ( $p = 0.512$  and  $p = 0.674$  for subject 1002,  $p = 0.830$  and  $p = 0.888$  for subject 1006, and  $p = 0.290$  and  $p = 0.341$  for subject 1008). Subjects 1002, 1006, and 1008 all have osteosarcoma of the distal femur.



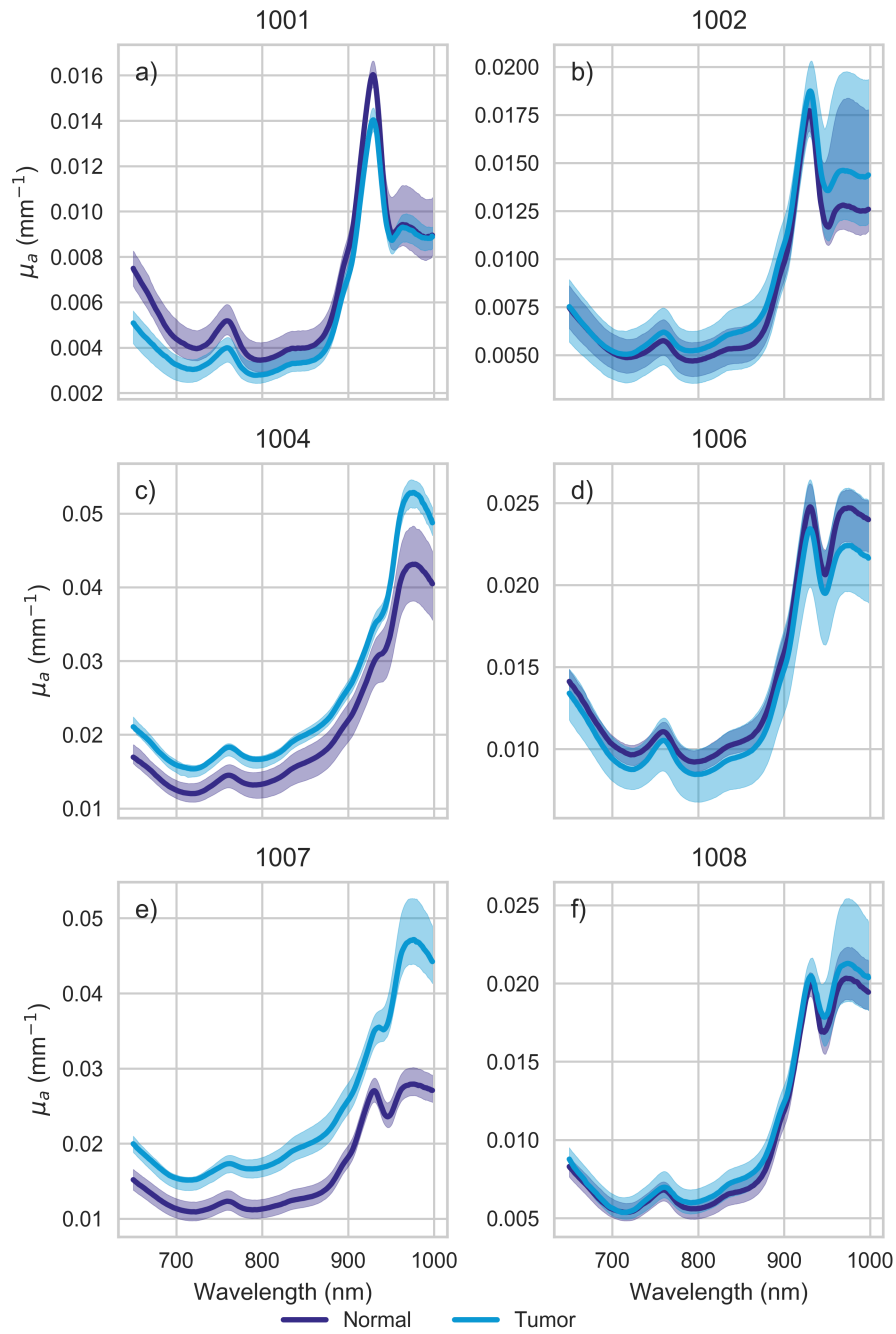


**Figure 3.2:** Median (solid line) and interquartile range (shaded) of  $\mu_a$  versus source wavelength obtained at tumor (blue) and contralateral normal (dark blue) locations for six sarcoma patients (a–f).

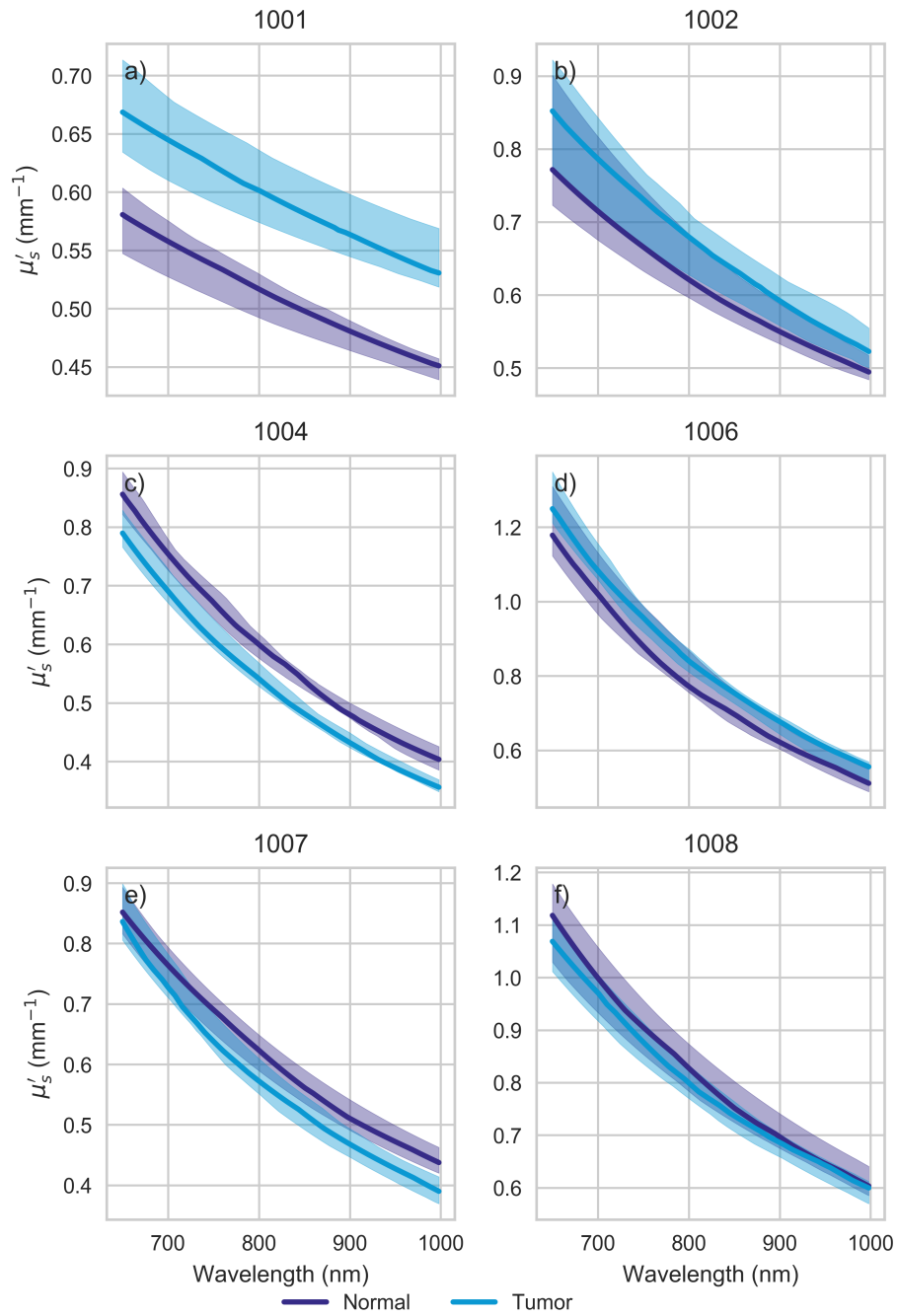


**Figure 3-3:** Median (solid line) and interquartile range (shaded) of  $\mu'_s$  versus source wavelength obtained at tumor (blue) and contralateral normal (dark blue) locations for six sarcoma patients (a-f).

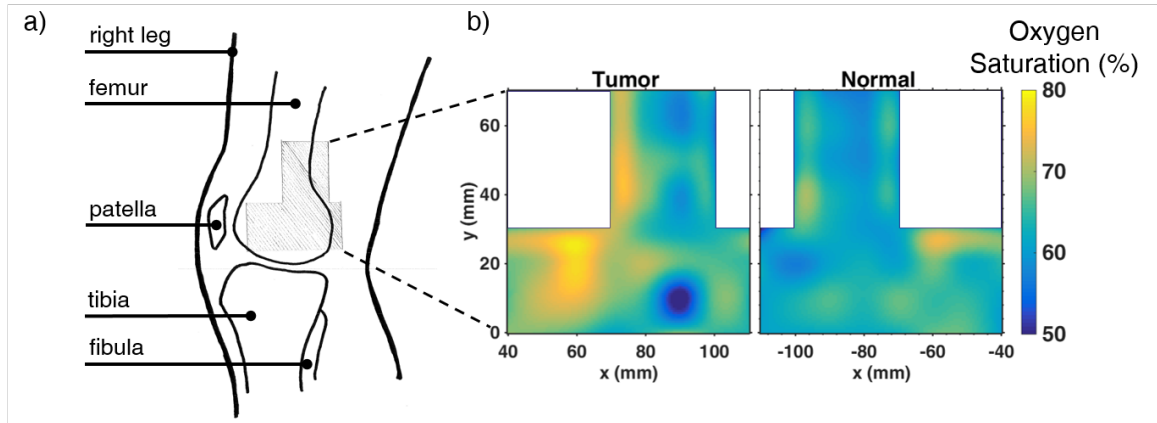


**Figure 3-4:** A 10 year old male with osteosarcoma in the right distal femur was measured with DOSI before neoadjuvant chemotherapy. (a) Diagram of bones in the right knee. The measurement area is the shaded region with the origin being the bottom tip of the patella. (b) Oxygen saturation maps for tumor and contralateral normal tissue.

### 3.3.5 Chromophore concentrations at baseline

There are differences in chromophore concentrations between tumor and contralateral tissue for all subjects in the analysis group. For example, Figure 3-4 shows a DOSI measurement of subject 1002 taken prior to neoadjuvant treatment. The measurement area, shown in Fig. 3-4a, was a “T” shape with a 1 cm spaced grid containing 48 points that covered a 7 x 7 cm area. For this region of interest, the total DOSI measurement time was 24 min. Despite the fact that 50% of the peak PHD did not reach the tumor (Table 3.5), oxygen saturation maps reveal differences between normal and sarcoma tissue, as seen in Fig. 3-4b ( $p < 0.001$ ). There is a strong visible correlation between oxygen saturation and tumor location, especially at the most superficial bone locations.

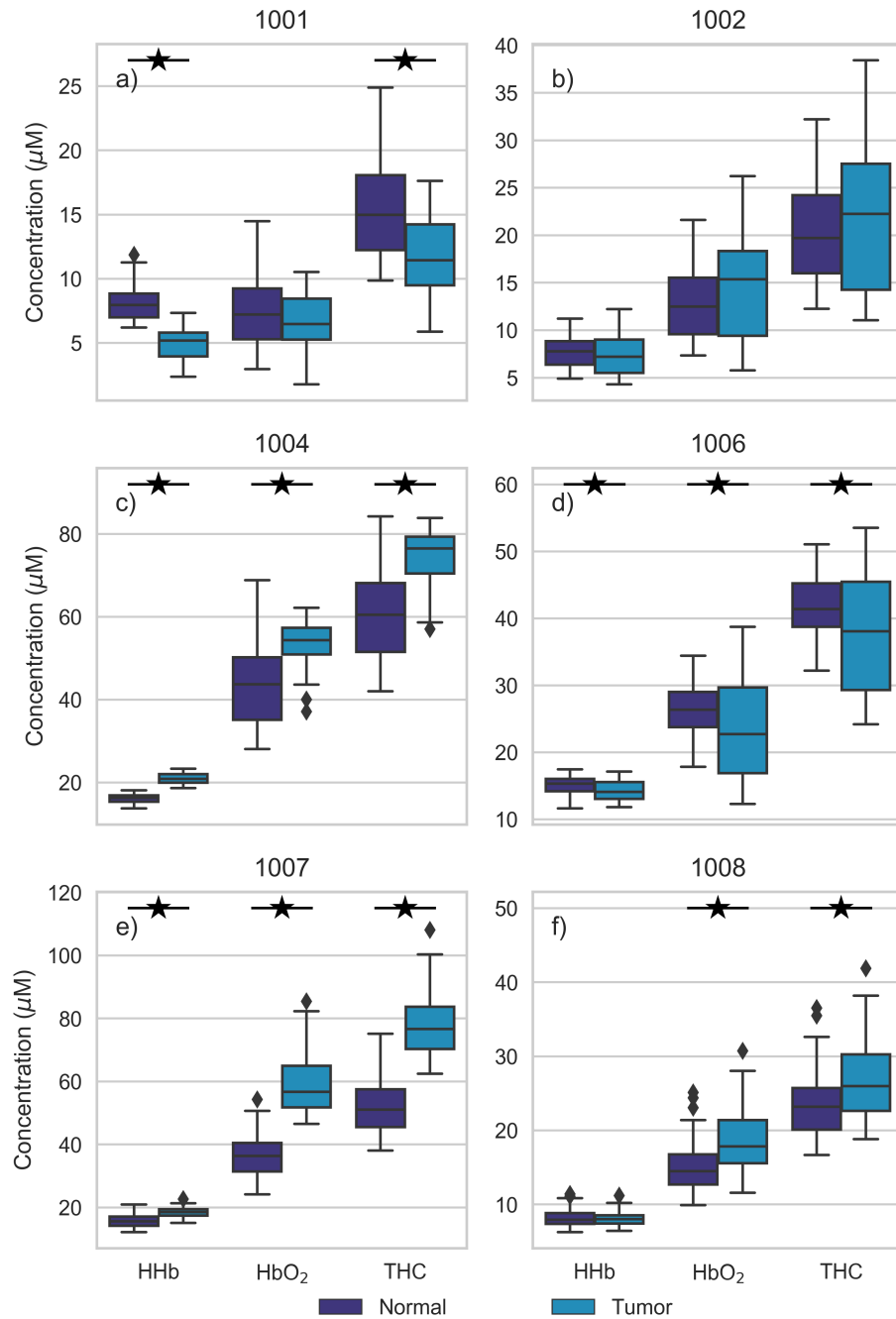


**Figure 3-5:** Hemoglobin concentrations ( $\mu\text{M}$ ) for tumor (blue) and contralateral normal (dark blue) tissue for six sarcoma subjects (a-f).  $\star$  represent a statistical significance between tumor and contralateral normal tissue at  $p = 0.05$ .

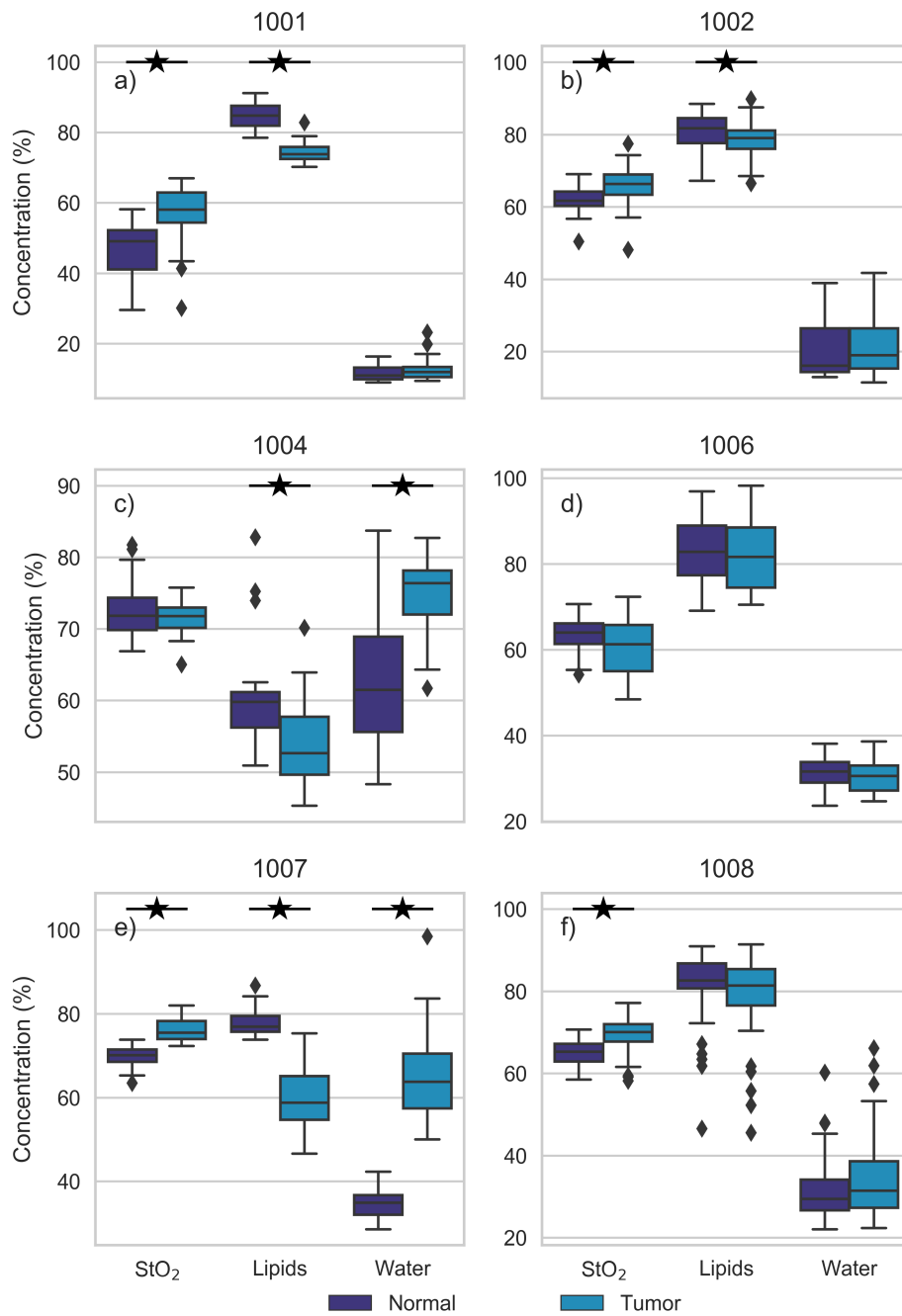


**Figure 3-6:** Water, lipid, and oxygen saturation (% concentration) for tumor (blue) and contralateral normal (dark blue) tissue for six sarcoma subjects (a-f). ★ represent a statistical significance between tumor and contralateral normal tissue at  $p = 0.05$ .

Chromophore information is summarized for each subject analyzed in Figures 3-5 and 3-6. As shown in Figure 3-5, tumor and contralateral normal tissue statistically differed in total hemoglobin concentration for five of the six subjects ( $p < 0.001$ ,  $p < 0.001$ , and  $p = 0.035$ ,  $p < 0.001$ , and  $p = 0.013$ , for subjects 1001, 1004, 1006, 1007, and 1008, respectively).

Subjects 1002, 1004, 1007, and 1008 had a higher median total hemoglobin concentration in the tumor compared to the contralateral normal, whereas subjects 1001 and 1006 had the opposite trend. For subject 1001, differences in total hemoglobin were driven by deoxyhemoglobin ( $p < 0.001$ ). For subjects 1004, 1006, and 1007, both deoxyhemoglobin ( $p < 0.001$ ,  $p = 0.037$ , and  $p < 0.001$ , respectively) and oxyhemoglobin ( $p = 0.007$ ,  $p = 0.038$ , and  $p < 0.001$ , respectively) contributed to differences in total hemoglobin concentration. Subject 1008 has a statistically higher oxyhemoglobin concentration in the tumor compared to the contralateral normal tissue ( $p = 0.003$ ).

Oxygen saturation was higher in the tumor compared to the contralateral normal tissue for subjects 1001, 1002, 1007, and 1008 ( $p < 0.001$  for all). For subjects 1004 and 1006, oxygen saturation is about the same or lower in the tumor ( $p = 0.643$  and  $p = 0.057$ , respectively). At the end of neoadjuvant treatment, subjects 1001, 1002, 1007, and 1008 also had a good response to treatment ( $>90\%$  tumor-cell necrosis).

As seen in Figure 3-6, lipid concentrations were lower in tumor tissue compared to contralateral normal tissue for four of the six subjects ( $p < 0.001$ ,  $p = 0.015$ , and  $p = 0.001$ , and  $p < 0.001$  for subjects 1001, 1002, 1004, and 1007, respectively). Water concentrations varied greatly between subjects. The median water concentration was higher in tumor tissue compared to contralateral normal tissue for all except subject 1006. However, only subjects 1004 and 1007 had statistical differences in water concentration ( $p < 0.001$  for both). Subjects 1004 and 1007 also had a substantially higher water concentration in both tumor and normal tissue compared to the other

subjects.

The Tissue Optical Index (TOI) is a commonly used contrast function in DOSI breast cancer measurements (Cerussi et al., 2006; Tromberg et al., 2016). TOI is defined as deoxyhemoglobin\*water/lipids, it has been used to identify tumor location (Cerussi et al., 2006). For subjects 1001, 1004, and 1007, the TOI is statistically different between tumor and contralateral normal tissue ( $p < 0.001$  for all subjects). This difference in TOI is not present for subjects 1002, 1006, and 1008.

### 3.4 Discussion

This feasibility study presents the first measurements of optical properties and chromophore concentrations of bone sarcomas using DOSI. In three of the nine enrolled subjects, DOSI measurements could not be taken due to touch sensitivity ( $n = 1$ ) or could not be analyzed due to high tissue attenuation ( $n = 2$ ). In the remaining six subjects, DOSI measurements demonstrated contrast between tumor and contralateral normal tissue in both optical properties and chromophore concentrations. These results suggest that DOSI is capable of measuring and characterizing sarcoma tumors, although improvements in DOSI probe technology are needed to acquire accurate measurements in a larger portion of this patient population.

The sarcomas measured in this study presented a diverse pattern of chromophore concentrations. Despite this diversity, several commonalities were noted. For example, three of the four subjects had statistically lower lipid concentrations in the tumor compared with the contralateral normal tissue. Of these, subjects 1001, 1004, 1007 had the largest differences in tumor lipid concentration compared with contralateral normal. Subjects 1001 and 1004 and both had Ewings sarcoma with a soft tissue component and subject 1007 had round cell sarcoma in the calf. For these subjects, the tumor may have displaced lipids content as it grew. Subject 1006 also had a soft

tissue component; however, there was no discernible difference in lipid concentration between the tumor and contralateral normal side, likely because the tumor was so deep (33.23 mm below the skin surface). It is also of note that the extracted lipid concentrations for subjects 1001, 1002, 1006, and 1008 are higher than those previously reported for bony locations on the limbs, although these prior reports were from more superficial locations (Pifferi et al., 2004).

While lipids were generally different in tumor compared with contralateral normal regions, only subjects 1004 and 1007 had significantly different water concentrations between tumor and contralateral normal tissue. It is of note that the magnitude of the water concentration for subject 1004 was much greater than the other subjects, and subject 1004 had the only measurement location not on the limbs (the tumor was on the ribs). Subject 1007 is the only subject with a tumor in the muscle. Literature values for water concentrations in tissue vary greatly (Taroni et al., 2007; Sekar et al., 2015b; Pifferi et al., 2004) but with the exception of subjects 1004 and 1007, the water concentrations in this study are similar to those previously reported for other bony locations on the limbs.

Hemoglobin levels varied to a large extent over subjects, but the concentrations of oxyhemoglobin and deoxyhemoglobin are generally comparable with other literature values for bony tissue. (Sekar et al., 2015b; Sekar et al., 2015a; Farzam et al., 2013; Pifferi et al., 2004; Doornbos et al., 1999) Median oxygen saturation values ranged from 50% to 70%, which fall on the low end of values reported in literature for other diffuse measurements performed on bone (Figure 3-6) (Sekar et al., 2015b; Farzam et al., 2013; Farzam et al., 2014). It is of note that the bone measurements in this study were not as superficial nor from the same locations as those in literature.

An interesting result from this study is that subjects 1001, 1002, 1007, and 1008 had a higher oxygen saturation in the tumor compared with the contralateral normal



tissue. Higher oxygen saturation could be from shunting or the increased metabolic demand of the tumor (Vaupel et al., 1989). As a static measurement, DOSI cannot distinguish differences between oxygen delivery and consumption, but adding a measure of blood flow may shed light on the specific physiology of these tumors (Cochran et al., 2017). The TOI showed contrast between tumor and contralateral normal tissue for the subjects with Ewings sarcoma. Both of these subjects had a soft tissue component that was more superficial to the surface of the skin. The subjects without TOI contrast had osteosarcoma of the distal femur.

Another exciting result is the statically different scattering slope for tumor and contralateral normal tissue in subjects 1001, 1004, and 1007. These subjects have Ewing’s sarcoma or round cell sarcoma. Small round cells is a hallmark feature of these diseases (Bernstein et al., 2006). Scattering slope is correlated with differences in particle size.

For five of the nine subjects, tumor measurements had a lower SNR compared to the contralateral normal measurements for all wavelengths. For subjects 1001 and 1008, tumor measurements had a higher SNR than contralateral normal tissue at 659 nm. Subjects 1006 and 1008 have similar SNR for tumor and contralateral normal tissues at all wavelengths, likely because the tumors were too deep to measure. Due to low SNR, the DOSI instrumentation could not measure the majority of non-responding tumors. It is likely these tumors were highly attenuating, but with improved instrumentation, it is hoped that measurements will lead to a prognostic marker.

### **3.4.1 Limitations**

There were several notable limitations of this clinical study. First, due largely to the rarity of the disease, the number of subjects is small and the anatomic sites measured are diverse. For these reasons, the data shown serve as the first documentation of the

optical characterization of this patient population, but it is not possible to make generalized statements about sarcoma optical properties and chromophore concentrations without more data.

Imaging depth is a challenge for some bone sarcomas. Photons must travel through skin, subcutaneous lipids, muscle, and bone to reach many of these tumors. For four of the six subjects analyzed in this study, the tumor depth overlapped with imaging depths (Table 3.5), but in two subjects, it is suspected that the tumor was too deep to be measured with the current probe geometry (subject 1006, 32.23 mm below the surface and subject 1008, 26.7 mm below the surface). Based on simulations of PHD for subject 1006 using matched optical properties in this region, a source-detector separation of 88 mm would be required for the 10% of the PHD peak to reach the tumor margin, whereas the current probe used a 28-mm source-detector separation. It is possible that the measured differences between tumor and normal tissue for these subjects arise from inflammation or other peritumoral effects. To better match tumor and imaging depths for cases like this, increased source-detector separations could be implemented, transmission geometries could be explored, or the use of late-photon gating could be used in time-domain systems to preferentially emphasize the contribution of photons that have traveled more deeply.

Improvements in signal level would greatly assist for measurements in this patient population. Tumors measured in the study had a large range of overall optical attenuation, and for some subjects the measured hemoglobin concentrations were very high (e.g., subject 1004 had an average tumor total hemoglobin level  $>70 \mu\text{M}$ ), presenting a challenge for achieving adequate SNR. In another subject (subject 1005), the SNR was determined to be too low for accurate optical property extractions. Additionally, if a larger source-detector separation were implemented to measure deeper tissues, increased detector sensitivity would also be required to avoid low SNR. To increase

the SNR, larger area APDs or photomultiplier tubes (PMTs) could be utilized, but each of these design choices involve tradeoffs. For example, larger area APDs generally have reduced modulation bandwidth, and PMTs have limited dynamic range and linear operating regions (Zhao et al., 2017).

Improvements to probe geometry and materials would also assist in measuring this patient population. For example, subject 1003 could not be measured because the tumor region was too tactile sensitive for a contact probe. A smaller probe footprint or different, softer, probe materials may alleviate this, but it is possible that subject tactile sensitivity could be a limitation of the technology for a portion of this patient population. Additionally, while the majority of bone sarcomas form in the long bones of the body (Bielack et al., 2002) sarcomas can form anywhere, and the probe needs to accommodate a wide range of anatomic sites. A smaller probe footprint or a flexible probe geometry may help facilitate measurements on angular and bony surfaces. Additionally, larger source-detector separations may be necessary to access deep tumors.

Additional limitations including the choice of chromophores and the light propagation model have been previously discussed in Section 2.4.1.

### **3.4.2 Conclusions**

Despite several potential limitations of this work, the data indicate that bone sarcomas are amenable to measurement with diffuse optical technologies and that optical contrast exists between tumor and contralateral normal regions. Improvements in instrumentation, including the ability to measure more highly absorbing tissue at deeper imaging depths, will be key to collecting future high-quality data sets.

This clinical study demonstrated the ability of DOSI to measure optical properties and functional information at several common sarcoma locations throughout the course of treatment. DOSI was able to differentiate between healthy and sarcoma tis-

sue, although there was substantial variation among subjects. Going forward, several key technological developments are required to better measure this patient population, including more flexible probes and more sensitive detection. Additionally, larger datasets are needed to characterize and quantify sarcoma optical properties and treatment response dynamics.

## Chapter 4

# Optimize DOSI instrumentation for sarcoma

### 4.1 Introduction

In order to accommodate the angular, rigid, and highly attenuating bony tissues that are common to sarcomas, the current DOSI instrumentation needs modifications. This chapter focuses on the simulation, creation, and experimental validation of an optimized DOSI probe that accurately measures common sarcoma locations.

### 4.2 Methods

#### 4.2.1 Literature review of optical properties

To create physiologic simulations, an extensive literature review of optical properties in the near-infrared wavelength range of 600–1000 nm for bone, muscle, and lipids was conducted. As discussed in Section 1.2.4, there is limited information about diffuse optics in bone. Due to the scarcity of available data, bone optical properties were expanded to include bony anatomic locations.

The literature search for lipid optical properties included all tissues described as having fat, adipose, or lipids. While breast tissue is a fatty tissue, it was excluded from the literature review unless the paper specified “adipose” in the tissue description, i.e. optical properties from “breast tissue” were excluded but “breast adipose tissue” were included. Optical properties from intralipids were excluded because the choice

of intralipid concentration was often not justified. Data from purified lipids were excluded since they do not represent physiological concentrations. A paper was also excluded for failing to account for lateral light loss in their measurements which may have lead to an overestimation of the absorption coefficient (Bashkatov et al., 2011; Bashkatov et al., 2005). In addition, another paper was excluded as theirs were the only samples that were hydrated with saline and sealed between a microscopic slide and a coverslip (Salomatina et al., 2006).

The literature review specifically focused on optical properties at 658 nm, in hopes of improving DOSI measurements at the wavelength with the lowest signal levels (Subsection 3.3.2). Given the limited data at 658 nm, optical properties were pooled from 630–670 nm. Due to the orders of magnitude variation, the median and 10 to 90 percentile ranges of  $\mu_a$  and  $\mu'_s$  were calculated for fatty tissues, bone, muscle, and combined bone-muscle for the pooled data.

For a full list of optical properties, please see Appendix A.

#### 4.2.2 Selection of optical property test set

Frequency-domain DOSI does not directly measure optical properties—it measures amplitude and phase (Pham et al., 2000). While high  $\mu_a$  and  $\mu'_s$  values may be a reason for low SNR, poor data quality may be from limitations in measuring amplitude and phase.

Aware that optical properties may not linearly map to instrumentation space (Erickson et al., 2010), the optical properties from Section 4.2.1 were used as inputs to the forward simulation of the P1 approximation to calculate phase and amplitude. The amplitude at 50 MHz from a calibrated measurement taken with a 28 mm source-detector separation on a highly absorbing black phantom provided an estimate of the amplitude noise floor.

Using data from Section 4.2.1, the median and 10 to 90 percentile range were

combined in such a way to create the most extreme cases of optical property pairs that might be seen in the clinic. Thus low scattering with high absorption and high scattering with low absorption case studies were created. After plotting the phase and amplitude in the forward stimulation, ten optical property pairs were chosen as a test set for simulations and tissue-mimicking phantoms to test the dynamic range of the DOSI instrumentation and validate the DOSI probe optimization. Among these ten optical property pairs, some are expected to be quite easy to measure while others will be impossible.

### **4.2.3 Creation of tissue-mimicking phantoms**

Silicone tissue-mimicking phantoms were created using nigrosin as the absorbing agent and titanium dioxide ( $\text{TiO}_2$ ) as the scattering agent. A 1.5g/L  $\text{H}_2\text{O}$  nigrosin solution was mixed into 600 mL of uncured silicone. Titanium dioxide and 60 mL of curing agent were mixed and sonicated for 30 min before being blended into the silicone-nigrosin mixture. The mixture was sealed in a vacuum chamber to remove air bubbles before being poured into a mold. The phantom cures and hardens within the vacuum chamber. For each phantom created, the quantities of nigrosin and  $\text{TiO}_2$  used are shown in Table 4.1.

### **4.2.4 DOSI instrumentation**

The BOTLab identified an APD with a 3-mm active area (S11519-30-Hamamatsu Photonics, Hamamatsu, Japan). The DOSI system used to test and validate the APD is the same system used in Chapter 2.2.2. The amplitude modulated light is detected by either the APD with a 0.5-mm active area (C5658 with detector S-6045, Hamamatsu Photonics, Hamamatsu, Japan) or with a 3-mm active area (S11519-30-Hamamatsu Photonics, Hamamatsu, Japan).

**Table 4.1:** Tissue-mimicking phantom recipes.

Phantom	Nigrosin (mL of 1.5g/L H <sub>2</sub> O solution)	TiO <sub>2</sub> (g)
all10	0.567	0.231
muscle10	1.368	0.274
bone10	0.453	0.325
all50	3.526	0.551
muscle50	7.204	0.166
bone50	0.772	1.540
bone90	3.085	2.682
bone1090-2	0.529	2.682
bone9010	2.956	0.565
muscle1090	1.322	3.008

#### 4.2.5 Calculation of signal-to-noise ratio

The experimental SNR was calculated the same way as the patient data SNR in Section 3.2.5: the raw amplitude divided by a dark measurement using modulation frequencies from 50–400 MHz. The dark measurement was calculated as the average of five measurements taken on a highly absorbing black phantom. For each phantom, the median SNR and the 10 to 90 percentile range is reported.

#### 4.2.6 Calculation of accuracy and precision

The  $\mu_a$  and  $\mu'_s$  values of on phantoms were measured with the 0.5-mm APD and 3-mm APD. Bland-Altman plots tested the interchangeability of the detectors.

With such attenuating phantoms, the choice of calibration phantom could impact the calculation of optical properties. To inform the choice of calibration phantom, percent difference in optical properties calibrated with ACRIN9 and INO9 were calculated using the 0.5-mm APD at 22 mm source-detector separation.



#### 4.2.7 Monte Carlo estimates of imaging depth

Imaging depth was estimated from maximum photon penetration depth. The maximum photon penetration depth was calculated as the maximum depth a collected photon traveled during a simulation in the Monte Carlo Multi Layered tissue simulator (MCML) (Calabro, 2013).

The simulation is a two layer model with the first layer mimicking subcutaneous fat and the second layer a sarcoma-like tissue. Simulation optical properties were determined from literature review (Section 4.2.1) and the sarcoma test set (Section 4.2.2). Given the wide range of  $\mu_a$  values for fatty tissues, simulations were conducted for a high ( $\mu_a=0.013 \text{ mm}^{-1}$ ) and low ( $\mu_a=0.003 \text{ mm}^{-1}$ ) absorbing fatty tissue layer. For both simulation conditions, the fatty layer was constant at  $\mu'_s=1.2 \text{ mm}^{-1}$ . The total simulation thickness remained constant at 100 cm with the first layer varying from from 0 to 10 cm thick. The simulation collected 10,000 photons and recorded the maximum penetration depth.

The numerical aperture ( $NA$ ) for the simulations was calculated with the following equation

$$NA = n \sin \theta \quad (4.1)$$

where  $n$  is the index of refraction of air at 658 nm ( $n = 1$ ) and  $\theta$  is the angle of collection ( $\theta = 56.3^\circ$ ).  $\theta$  was calculated using dimensions from the 3-mm APD datasheet (Hamamatsu Photonics, ).

For each fatty layer thickness and sarcoma-like tissue, the proportion of photons reaching the underlying layer was calculated.

#### 4.2.8 Optimal source-detector separation

One way to increase imaging depth is by increasing the source detector separation. Using the sarcoma optical properties, calculated the phase and amplitude at differ-

ent source-detector separations using the forward simulation. As an experimental validation, the sarcoma phantom set was measured with source-detector separations from 34–88 mm. The SNR for each measurement was calculated using the methods described in section 4.2.5.

#### **4.2.9 Probe housing considerations**

Improvements in the handheld probe geometry would assist in measuring the angular and rigid anatomic locations common to sarcomas. The probe needs to accommodate a wide range of anatomic sites and have adequate contact on both sides of the body while maintaining the same source-detector orientation. The source-detector separation needs to be adjustable. In addition, the probe housing material must be lightweight, temperature-insensitive (not cold or hot to the touch), and disinfectant compatible.

### **4.3 Results**

#### **4.3.1 Literature review of optical properties**

Optical properties from literature review for bone, muscle, and lipid are show in Figure 4-1. Even with the expanded literature search to include bony locations, only nine papers were identified citing  $\mu_a$  and  $\mu'_s$  (including a paper citing results in Chapter 3). The 23 data points included *in vivo* and *ex vivo* measurements from six animal sources (including humans) and fourteen different bony locations. Optical properties for muscle were reported in eleven papers; the 76 data points were from six animal sources (including humans) for least eight different muscles. After removing papers for quality control, ultimately seven papers with optical properties for lipids were identified in the review, yielding 24 data points from three sources and six types of lipids.

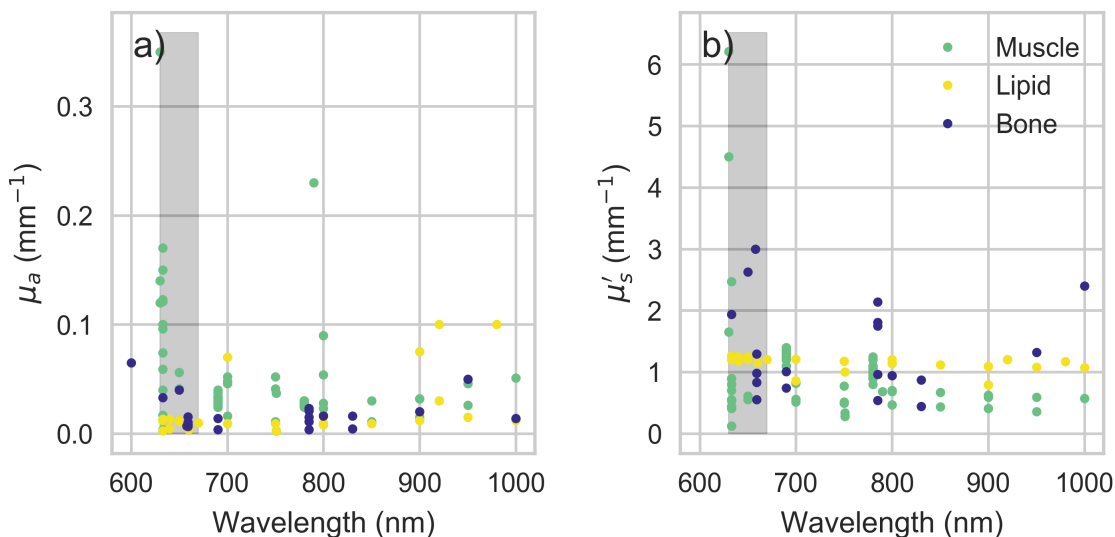


**Figure 4.1:** Literature values for  $\mu_a$  (a) and  $\mu'_s$  (b) for lipid (gold), muscle (green), bone (dark blue). Optical properties from 630–670 nm used for further analysis are shaded in grey.

Given the scarcity of data and the variation of  $\mu_a$  and  $\mu'_s$  values at 658 nm, optical properties were pooled from 630–670 nm. The median and 10 to 90 percentile ranges of  $\mu_a$  and  $\mu'_s$  were calculated for fatty tissues, bone, muscle, and combined bone-muscle for the pooled data and reported in Table 4.2. The median  $\mu_a$  values for lipid, muscle, and bone were respectively 0.110, 0.085, and 0.010 mm<sup>-1</sup> and the  $\mu'_s$  values were respectively 1.20, 0.66, and 1.29 mm<sup>-1</sup>. Values for  $\mu_a$  ranged from 0.003 to 0.013 mm<sup>-1</sup> for lipids, 0.016 to 0.16 mm<sup>-1</sup> for muscle, and 0.007 to 0.036 mm<sup>-1</sup> for bone. Values for  $\mu'_s$  ranged from 1.17 to 1.26 mm<sup>-1</sup> for lipids, 0.42 to 3.08 mm<sup>-1</sup> for muscle, and 0.72 to 2.78 mm<sup>-1</sup> for bone. For combined muscle and bone optical properties,  $\mu_a$  ranged from 0.007 to 0.146 mm<sup>-1</sup> and  $\mu'_s$  from 0.43 to 2.85 mm<sup>-1</sup>.

For a full list of optical properties used in analysis, please see Appendix A.

**Table 4.2:** Median and 10 to 90 percentile ranges of optical properties from literature 630–670 nm.

Tissue	$\mu_a$ ( $\text{mm}^{-1}$ )	$\mu'_s$ ( $\text{mm}^{-1}$ )
Lipid	0.011 [0.003, 0.013]	1.20 [1.17, 1.26]
Muscle	0.085 [0.016, 0.16]	0.66 [0.42, 3.08]
Bone	0.010 [0.007, 0.036]	1.29 [0.72, 2.78]
Muscle and bone	0.041 [0.007, 0.146]	0.83 [0.43, 2.85]

#### 4.3.2 Selection of optical property test set

The literature review optical properties pairs from 630–670 nm were used as inputs to the forward simulation of the P1 approximation to calculate the phase and amplitude at 50 MHz with a 28 mm source-detector separation. As shown in Figure 4-2, when plotted in the phase and amplitude space, lipid and muscle separate themselves along the x-axis. With the 0.5-mm APD, 71.5% of the optical properties pairs fall below the noise floor. The 3-mm APD has a lower noise floor than the 0.5-mm APD, potentially allowing the measurement of and additional 43% of the optical property pairs from the literature review.

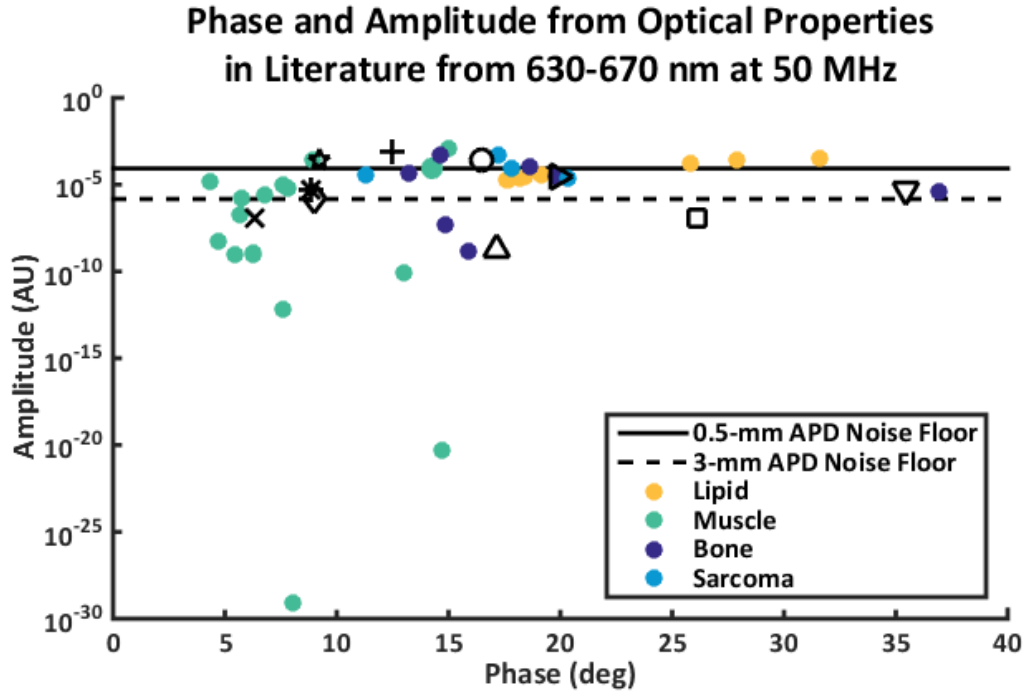


**Figure 4.2:** The phase and amplitude from the P1 diffusion approximation of the radiative transport equation for optical properties in literature from 630–670 nm for lipid (gold), muscle (green), bone (dark blue), and sarcoma (blue) is shown. Black markers are the test set optical properties defined in 4.3. The implementation of the 3-mm diameter area detector will lower the noise floor (dashed line) and allow a greater range of optical properties to be measured.

For simulations and experimental validation, ten optical property pairs (Table 4.3) were chosen as a test set. These optical properties span the phase and amplitude space of the DOSI instrumentation. The following three optical property pairs ( $\mu_a$ ,  $\mu'_s$ ) are below the noise floor for both APDs: (0.016, 3.08), (0.036, 2.78), and (0.085, 0.66)  $\text{mm}^{-1}$ . The following four optical property pairs are below the 0.5-mm APD’s noise floor: (0.007, 2.78), (0.010, 1.29), (0.036, 0.72), and (0.041, 0.83)  $\text{mm}^{-1}$ . Three optical property pairs are above the noise floor for both APDs: (0.007, 0.43), (0.007, 0.72), and (0.016, 0.42)  $\text{mm}^{-1}$ .

**Table 4.3:** Optical property test set.

$\mu_a$ (mm <sup>-1</sup> )	$\mu'_s$ (mm <sup>-1</sup> )	Marker
0.007	0.43	+
0.007	0.72	○
0.007	2.78	▽
0.010	1.29	▷
0.016	0.42	★
0.016	3.08	□
0.036	0.72	*
0.036	2.78	△
0.041	0.83	◇
0.085	0.66	×

### 4.3.3 Signal-to-noise ratio

Compared to the 0.5-mm APD (C5658 with detector S-6045, Hamamatsu Photonics, Hamamatsu, Japan), the 3-mm APD has a 16-fold increase in active area for more light collection. Testing the 3-mm APD fiber has shown that the noise floor is comparable to 0.5-mm APD. As seen in Figure 4-3, the 3-mm APD has a higher SNR than the 0.5-mm APD across all modulation frequencies.

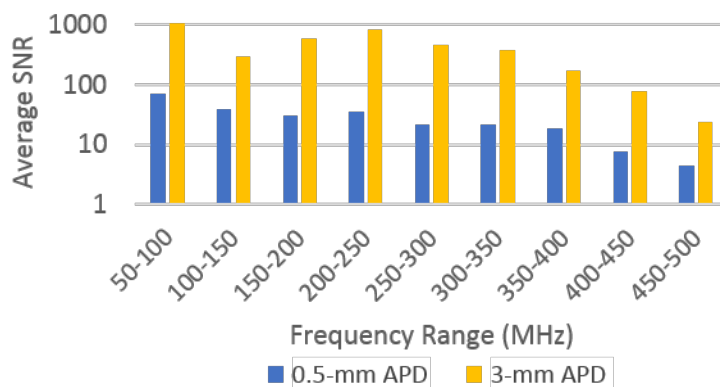


**Figure 4.3:** The SNR averaged across modulation frequencies for the 0.5-mm APD (dark blue) and the 3-mm APD (yellow).

On average from 50–400 MHz, the 3-mm APD has a median SNR 18 times greater than the 0.5-mm APD at a source-detector separation of 34 mm. For the individual wavelengths 650, 690, 785, 808, 830, and 850 nm, the median SNR was 8, 12, 20, 16, 22, and 29 times greater, respectively. The 3-mm APD has a higher SNR than the 0.5-mm APD and can measure more attenuating optical properties at longer source-detector separations.

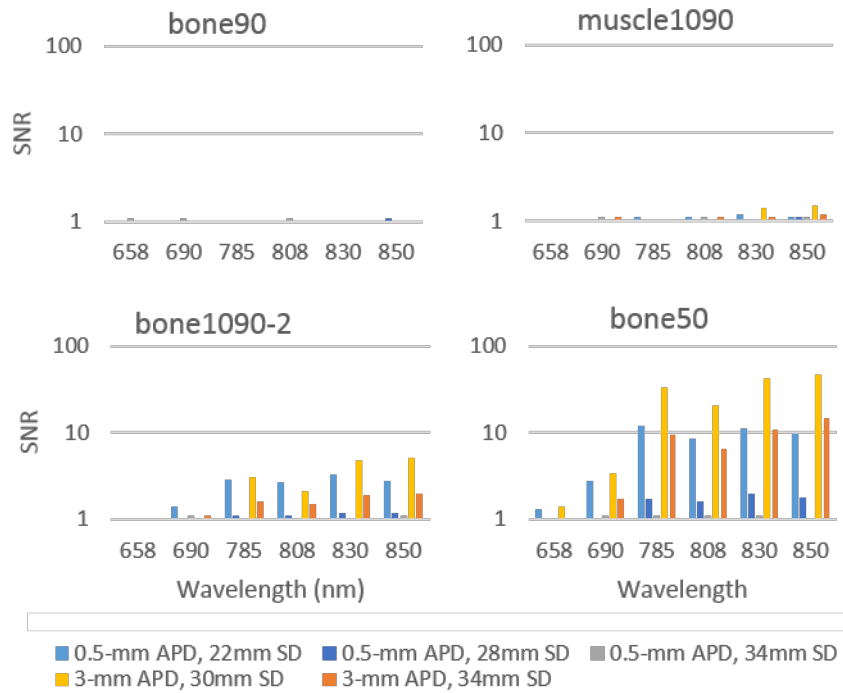


**Figure 4-4:** The median SNR at each wavelength for different source-detector (SD) separations for a phantom for the 0.5-mm APD (blue, dark blue, grey) and the 3-mm APD (yellow, orange).



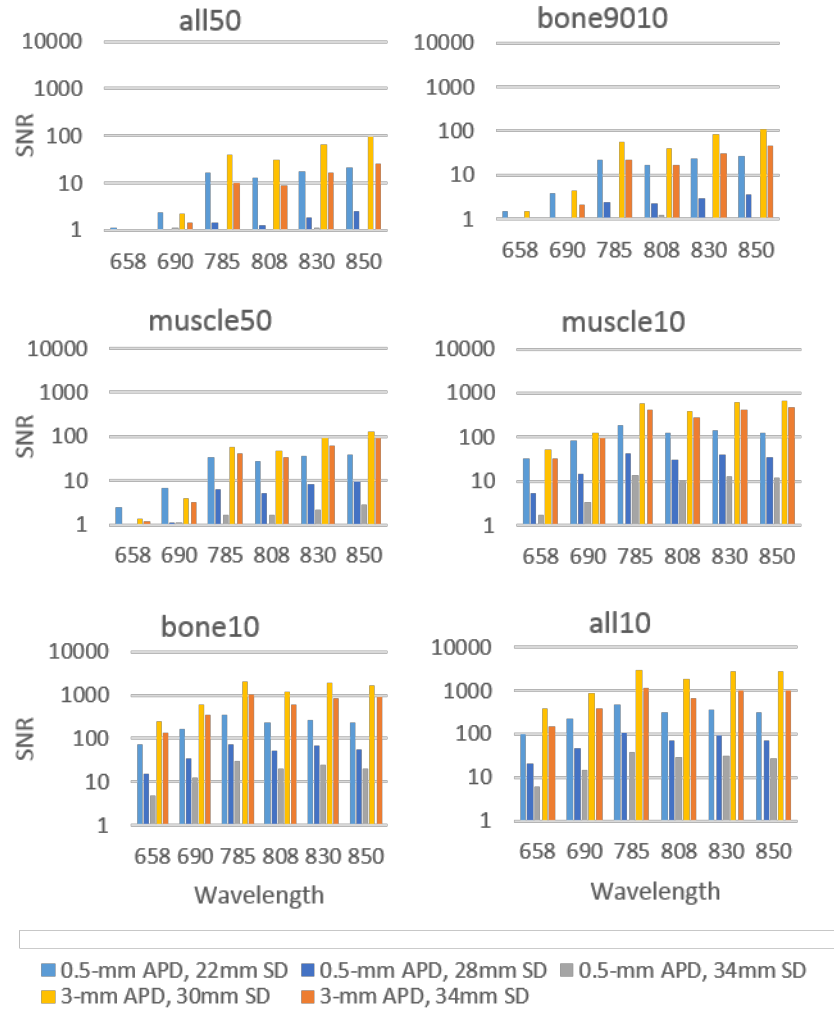


**Figure 4-5:** The median SNR at each wavelength for different source-detector separations for a phantom for the 0.5-mm APD (blue, dark blue, grey) and the 3-mm APD (yellow, orange).

#### 4.3.4 Accuracy and precision

Bland-Altman plots compared the difference and means of  $\mu_a$  and  $\mu'_s$  from phantom measurements using the 0.5-mm APD and the 3-mm APD in Figures 4-6 and 4-7, respectively. For all wavelengths, measurements both  $\mu_a$  and  $\mu'_s$ , the vast majority of measurements lay within  $\pm 1.96$  standard deviations. The largest deviations from the average occur with increasing  $\mu_a$  and  $\mu'_s$  values.

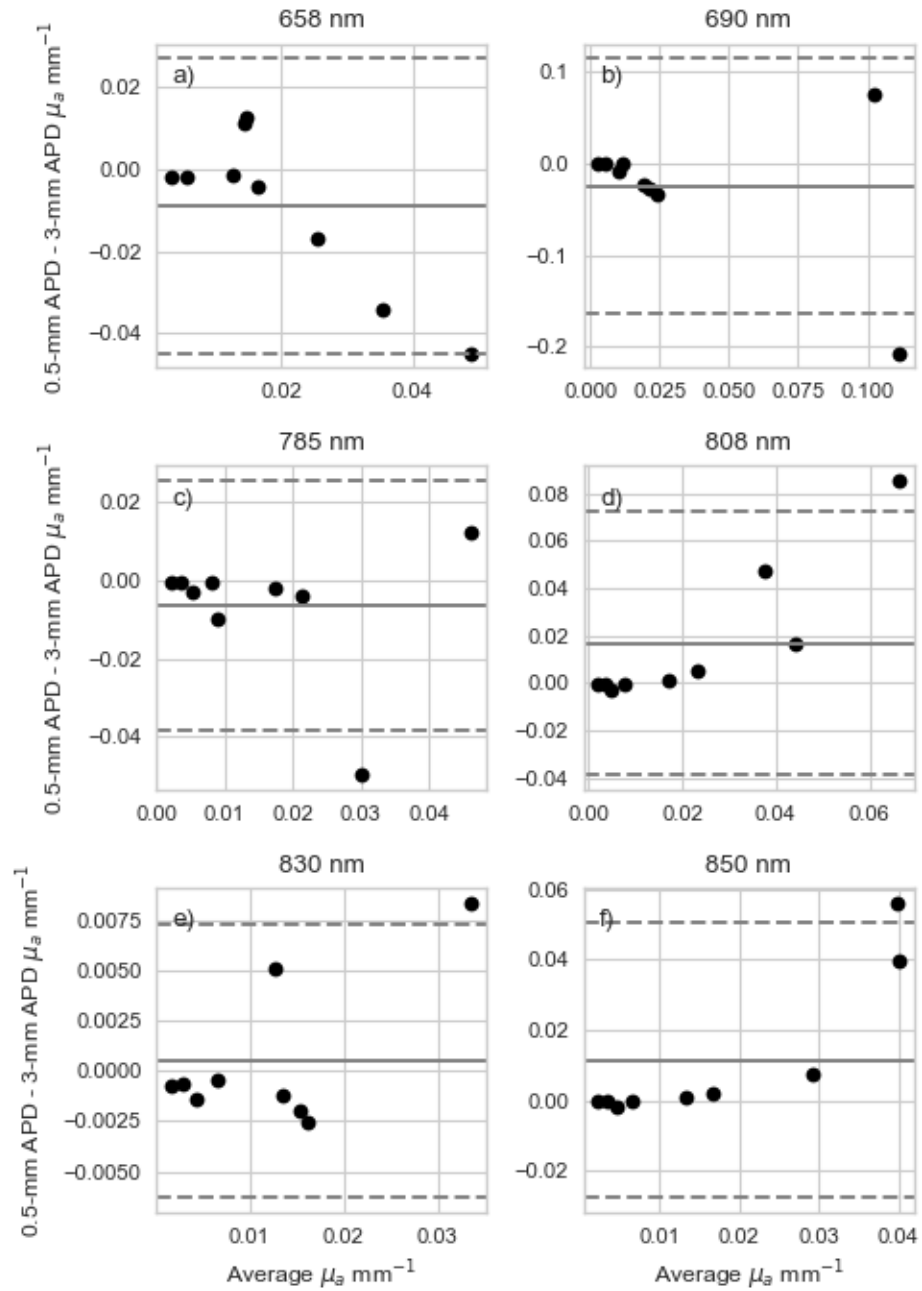


**Figure 4.6:** Bland-Altman plots comparing measurements of  $\mu_a$  at (a) 658, (b) 690, (c) 785, (d) 808, (e) 830, and (f) 850 nm. The mean (solid line) and  $\pm 1.96$  standard deviations (dashed lines) of the data are shown.

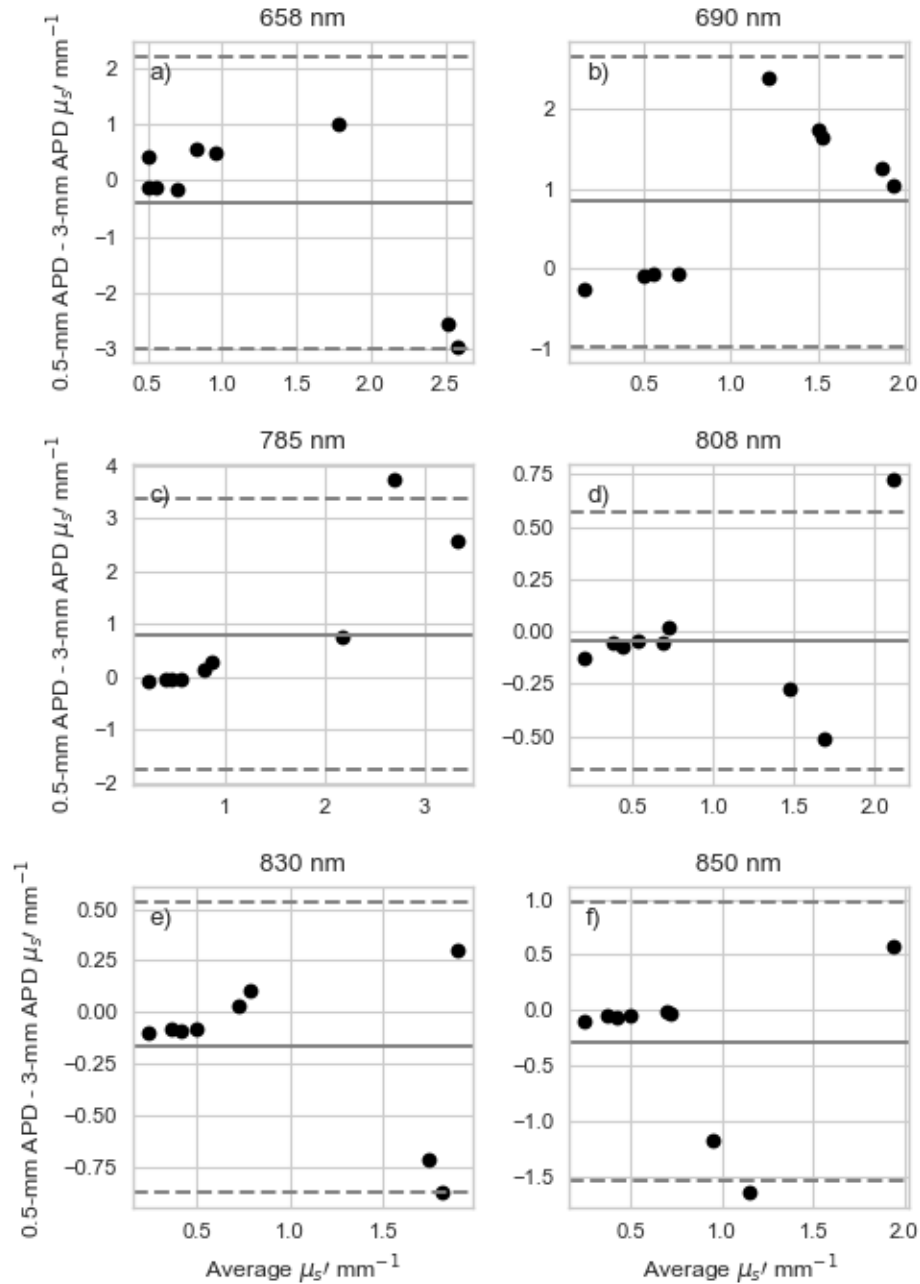


**Figure 4.7:** Bland-Altman plots comparing measurements of  $\mu_s'$  at (a) 658, (b) 690, (c) 785, (d) 808, (e) 830, and (f) 850 nm. The mean (solid line) and  $\pm 1.96$  standard deviations (dashed lines) of the data are shown.

INO9. Median percent differences in  $\mu'_s$  were 2.5%, ranging from 1.1 to 4.4%. Percent differences in  $\mu_a$  were greater, the the median percent difference was 5.9% with a range from 2.8% to 15.2%. Seven of the phantoms (54%) had  $<5\%$  difference in  $\mu_a$  values and four (31%) had differences between 5–10%. The two phantoms that had the largest percent difference were the phantoms with the smallest  $\mu_a$  values.

#### 4.3.5 Estimates of imaging depth

MCML simulations estimated the photon imaging depth for sarcoma-like optical properties under a fatty layer. The proportion of photons that reach the underlying sarcoma layer are shown in Figure 4-8.

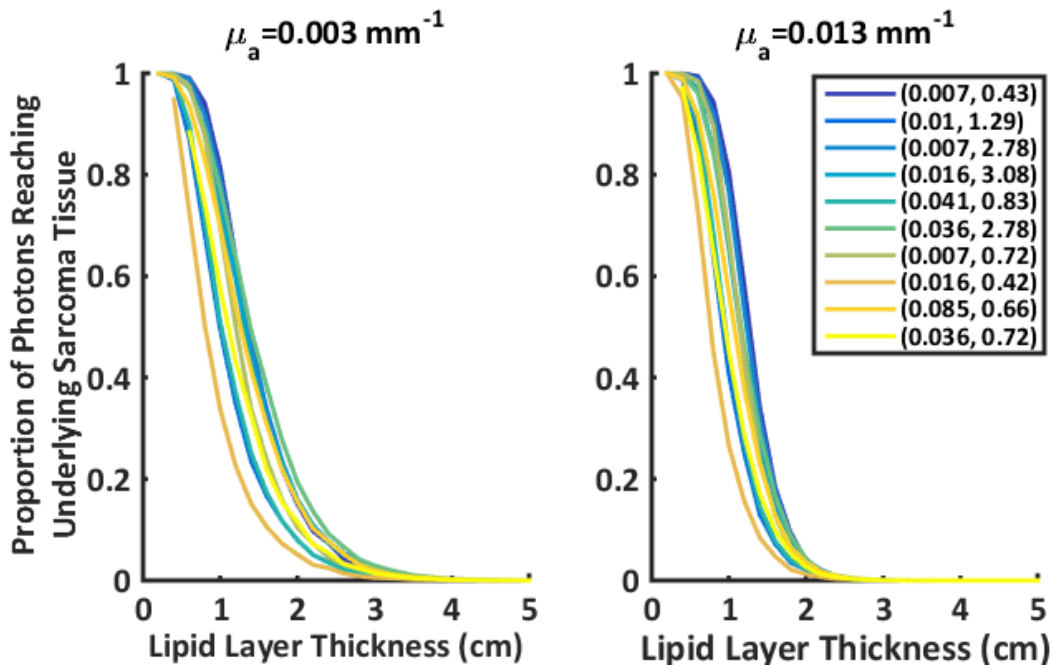


**Figure 4-8:** Proportion of photons reaching an underlying sarcoma-like tissue with varying lipid layer thicknesses. Simulations are for a (a) low and (b) high absorbing lipid layer.

Both simulation situations had similar responses—50% of the photons reached beyond a 0.8 cm lipid layer into the underlying tissue. In the low absorbing lipid layer simulation, photons penetrated more deeply, with 50% of photons reaching

beyond a 1.4 cm lipid layer compared to a 1.2 cm lipid layer in the high absorbing simulation. In the low absorbing simulation, 10% of photons passed beyond a lipid layer of 1.6–2.4 cm thick and 90% passed a lipid layer 0.4–0.8 cm thick. In the high absorbing simulation, 10% of photons passed beyond a lipid layer of 1.4–1.8 cm thick and 90% passed a lipid layer 0.4–0.8 cm thick.

#### **4.3.6 Optimal source-detector separation**

Simulations from the P1 diffusion approximation show that as the source-detector separation increases from 22 to 40 mm, the amplitude approaches the noise floor of the 0.5-mm and 3-mm APDs (Figure 4-9). Four test optical properties are above the 0.5-mm APD noise floor at the shortest source-detector separation; in comparison, there are nine above the 3-mm APD noise floor. At a source-detector separation of 40 mm, only one remains above the 0.5-mm noise floor compared to three above the 3-mm APD noise floor.

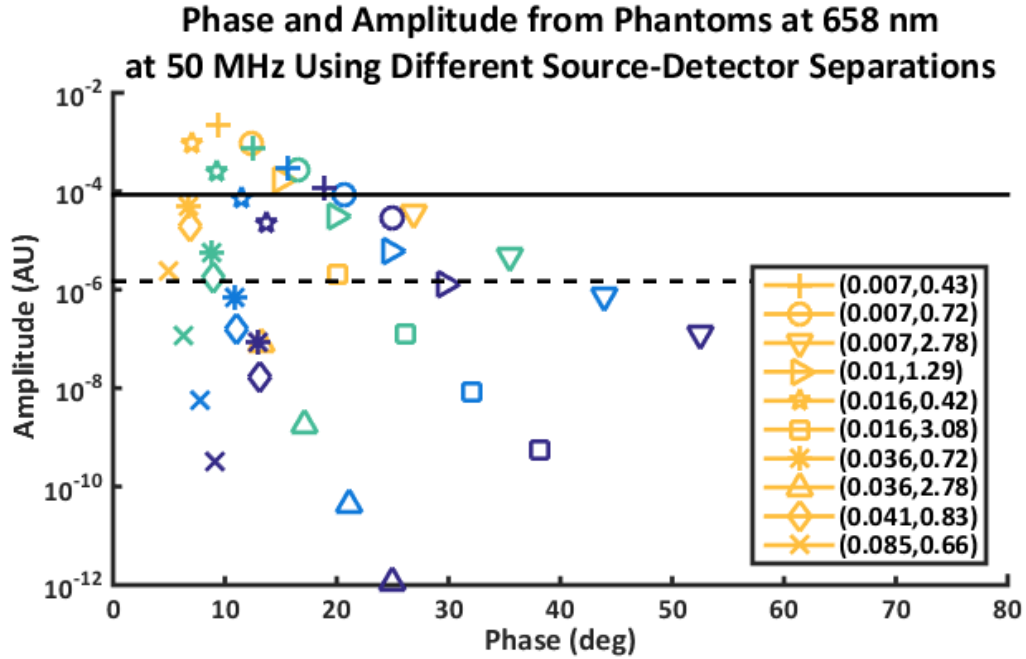


**Figure 4-9:** The phase and amplitude from the P1 diffusion approximation of the radiative transport equation for optical properties in sarcoma test set at 22 (gold), 28 (green), 34 (blue), and 40 mm (dark blue) source-detector separation. The noise floor for the 0.5-mm APD (solid line) and the 3-mm APD (dashed line) are shown for reference.

The simulations in Figure 4-9 were validated experimentally with phantoms in Figure 4-10. For all wavelengths, the SNR decreased as the source-detector separation increased. At the shortest source-detector separation, the 3-mm APD could measure seven of the ten sarcoma-like phantoms at 658 nm (Figure 4-10a). However after 46 mm, the 3-mm APD could only measure three phantoms.

In Figure 4-10b, the SNR at 690 nm is greater, but after 52 mm, only three phantoms could be measured. Figure 4-10c–f shows the SNR of wavelengths 785, 808, 830, and 850 nm are an order of magnitude greater than the SNR at 658 nm (Figure 4-10a).

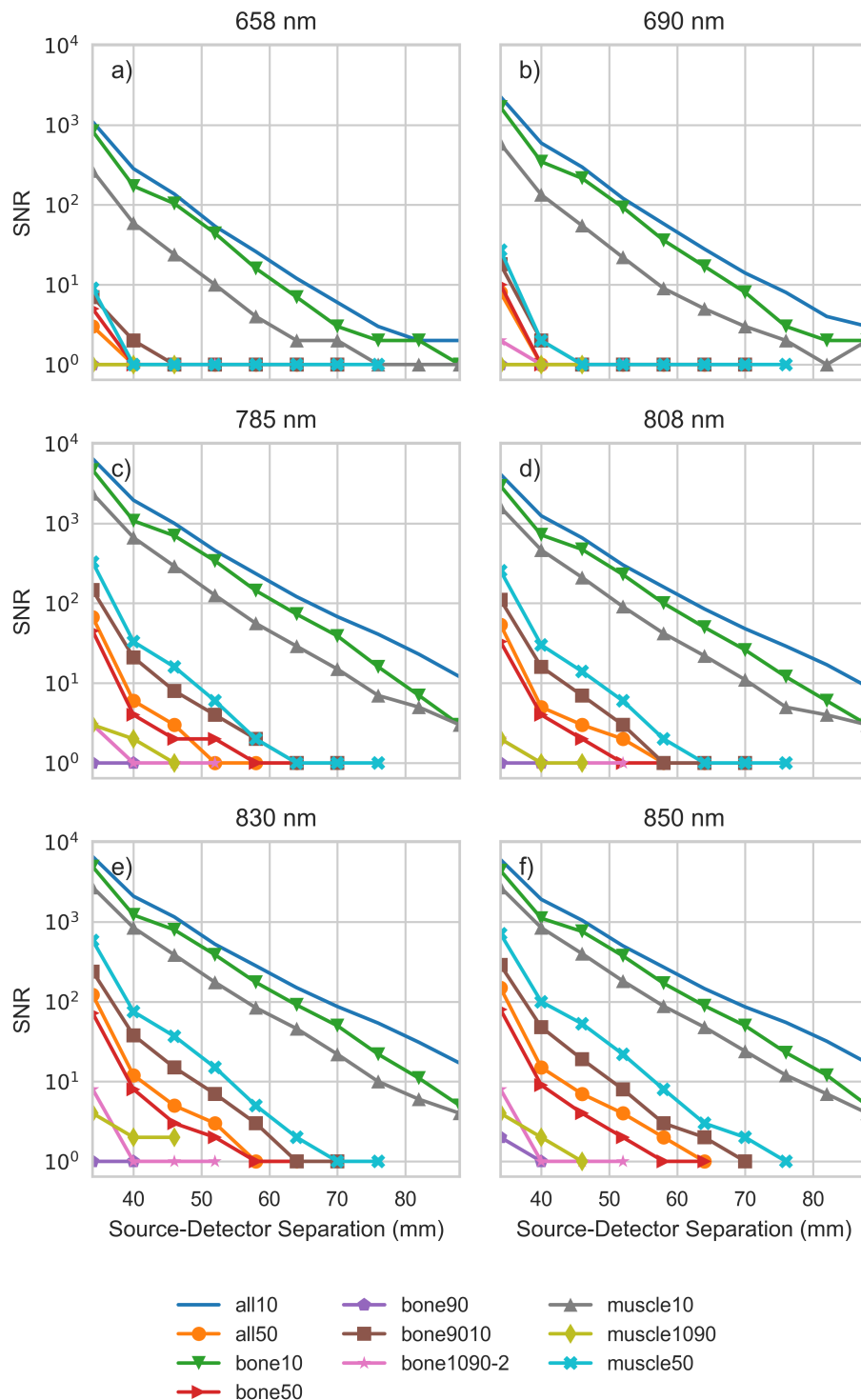


**Figure 4-10:** 3-mm APD SNR for sarcoma-like phantoms at wavelengths (a) 658, (b) 690, (c) 785, (d) 808, (e) 830, and (f) 850 nm at source-detector separations from 34–88 mm.

### 4.3.7 Probe housing

The probe housing for the 3-mm APD is 3D-printed from ABS. The material is lightweight, temperature-invariant, and disinfectant compatible. The source-detector separation is adjustable and can be moved to either side of the APD housing. There are many air holes for ventilation so the electronics do not overheat. The handheld 3-mm APD probe is 66% smaller than the 0.5-mm APD probe.

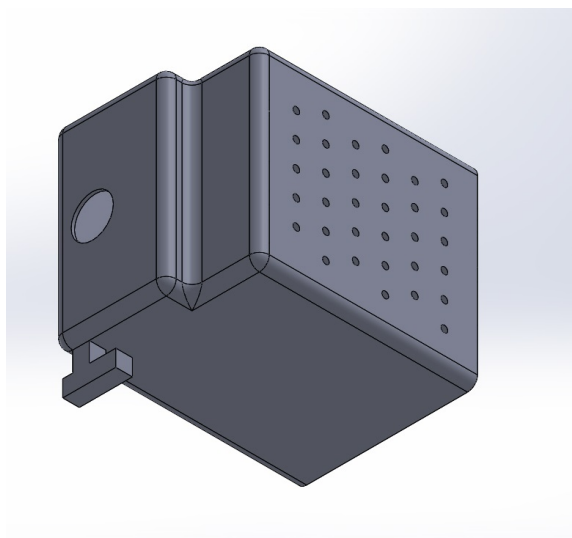


**Figure 4-11:** Designed probe housing for 3-mm APD.

## 4.4 Discussion

These simulations and experimental results are an important step towards measuring sarcomas.

Optical properties from literature for bone, muscle, and lipid were quite diverse. Values of  $\mu_a$  and  $\mu'_s$  from 630–670 nm spanned an order of magnitude. Averaging across 40 nm and the diversity of biological samples, methods, and instrumentation likely contributed to the wide range of values.

Sample preparations and measurements differed, which accounted for some of the variation in optical properties seen. Especially in muscle, sample preparations vastly



differed with samples being frozen, thawed, fresh, chopped, ground, or *in vivo*. For muscle, this sample preparation appeared to affect scattering, with more “processed” samples having lower  $\mu'_s$  values. In fatty tissues, fresh samples taken from surgery and used within hours had the highest absorption, likely because water content was still retained within the sample.

When comparing the choice of calibration phantom, the two phantoms that had the largest percent difference in  $\mu_a$  were the phantoms with the smallest  $\mu_a$  values. They were likely most affected by the optical property differences in the calibration phantoms—at 658 nm, INO9  $\mu_a=0.008 \text{ mm}^{-1}$  whereas ACRIN9  $\mu_a=0.018 \text{ mm}^{-1}$ . Given high absorbing tissues are the most likely to be encountered in a clinical setting, ACRIN9 is the best choice for a calibration phantom.

As the laser wavelength with the worst SNR during volunteer and clinical measurements (section 3.3.2), this chapter has used laser 658 nm as a benchmark for improvements and optimization of the DOSI instrumentation. The 3-mm APD seems like a promising detector to improve the SNR of the DOSI system. While the 3-mm APD has a much larger surface area, the bandwidth is still broad enough that measurements are not impacted. Not only does the 3-mm APD have a higher SNR across all frequency ranges and optical property pairs, it can measure optical properties the 0.5-mm APD couldn't.

While 50% of photons reach 1 cm into tissue with the 0.5-mm APD at a 28 mm source-detector separation, it would be beneficial to probe more deeply into tissues. With the 3-mm APD, the SNR is higher at longer source-detector separations than with the 0.5-mm APD. Based on the experimental results from Figure 4-10, source-detector separations would be limited to <34 mm if choosing to optimize 658 nm. However, this wavelength clearly struggles with such extreme optical property pairs, and it would be better not to include it. At 690 nm, half of the phantoms can be

measured with a source-detector separation of 40 mm. Repeating the simulations from Section 4.3.5, 50% of photons would travel 0.5 cm deeper using a 40 mm source-detector separation. In literature, diffuse optic probe source-detector spacing for bony measurements ranged from 10–40 mm (Meertens et al., 2018).

The smaller, symmetric probe footprint may facilitate access and adequate skin contact to bony locations on both sides of the body while maintaining the same source-detector orientation. To further decrease the contact area of the probe, the detector could be fiber coupled. If the 3-mm APD was fiber coupled, the average median SNR would only be 2 higher than the 0.5-mm APD. As shown in 4.3.3, the 3-mm APD has an average median SNR 18 time greater. A larger contact area was kept in favor of the increased signal levels.

Another option would be to use a PMT instead of an APD. PMTs have a large active areas with a large dynamic range. However the BOTLab group has discovered nonlinearities in dynamic range and signal level for several PMTs. Due to these nonlinearities, calibrations for each wavelength and each measurement would be required. The additional calibrations would increase measurement time and the time necessary with the subject. Using fiber coupled system, a separate PMT for each wavelength could reduce the number of calibrations necessary, however, this solution still assumes a linearity for each PMT over a wide range of optical properties.

#### **4.4.1 Limitations**

Bone is a complex and highly organized tissue with many components including calcium, hydroxyapatite, collagen, marrow, cartilage, nerves, and blood (Lodish et al., 2000). Values reported from DOSI measurements represent an average of the tissue, though it is still unknown how the optical properties of bone change throughout the body or from cancerous growth. Fatty tissue optical properties also vary with anatomic location (Salomatina et al., 2006). Simulations tried to account for these

variations by running under a variety of optical property conditions.

Frequency-domain diffuse optical spectroscopic simulations were not performed. Binzoni et al. showed that for modulation frequencies  $<200$  MHz, frequency-domain and continuous wave measurements had equivalent depth sensitivities (Binzoni et al., 2017). Estimates of imaging depth were not experimentally validated.

#### **4.4.2 Conclusions**

The simulations and experimental data indicate that the 3-mm APD will improve measurements on more highly attenuating tissues at deeper imaging depths. A housing was designed so the 3-mm APD can be incorporated as a hand held probe to facilitate measurements at bony locations.

## Chapter 5

# Conclusions

This project developed and validated DOSI as a non-invasive measurement modality to track treatment for sarcomas. For the first time, the optical properties and functional hemodynamic information of the distal femur, tibia, and humerus were characterized in normal volunteers. DOSI demonstrated the ability to measure optical properties and functional information at several sarcoma locations throughout the course of treatment. It was able to differentiate between healthy and sarcoma tissues within a patient. Improvements made to the instrumentation will facilitate future measurements in this patient population. In the future, DOSI may provide a way to monitor treatment response and improve patient outcomes.

### 5.1 Discussion

Of the 9 sarcoma subjects measured in Chapter 3, 7 had a sarcoma in a location measured in by the normal volunteer study in Chapter 2. In general, the chromophore concentrations are similar between the sarcoma subjects (Figures 3-5 and 3-6) and the normal volunteers (Figure 2-4). Normal volunteers and sarcoma subjects were measured with the same detector and hand held probe, but different instrumentation systems, which could be a source of bias when comparing across populations.

All sarcoma subjects had a substantially higher lipid concentration than the normal volunteers. With the exception of subject 1001, all sarcoma subjects also had a higher water concentration than the normal volunteers.

Subject 1001 had Ewing's sarcoma at the humerus. The oxyhemoglobin, total hemoglobin, and tissue oxygen saturation values were below one standard deviation of the average from the volunteer study. For deoxyhemoglobin concentrations, the contralateral normal tissue was within one standard deviation of the volunteer study while the tumor tissue was below.

Subjects 1002, 1006, and 1008 all had osteosarcoma of distal femur. Compared to the normal volunteer femur data, all contralateral normal tissue and the tumor for subject 1006 was more than one standard deviation outside the mean for tissue oxygen saturation; the tumors for subjects 1002 and 1008 were inside one standard deviation of the normal volunteer mean. Tumor and contralateral normal tissues had oxyhemoglobin concentrations within one standard deviation of volunteer femur data for subjects 1006 and 1008, while subject 1002 was outside one standard deviation. For deoxyhemoglobin concentration, subject 1008 was inside one standard deviation, subject 1006 was outside one standard deviation, and the contralateral normal side of subject 1002 was inside while the tumor was outside one standard deviation. For total hemoglobin concentration, subject 1006 and the tumor side of subject 1008 were within one standard deviation while subject 1002 and the contralateral normal side of subject 1008 was outside.

Of the normal volunteers, 64% had statistical differences between the left and right distal humerus tissue. The magnitude of the chromophore differences at the humerus between tumor and normal tissue is similar to differences between left and right tissues in normal volunteers. Tissue oxygen saturation had the most notable difference between tumor and normal tissue (10.7% difference) compared to left and right tissues (2.5% difference). Average absolute value differences for volunteers in oxyhemoglobin, deoxyhemoglobin, and total hemoglobin concentration are 8.4, 2.0, and 9.2  $\mu\text{M}$ , respectively. Average differences for volunteers in water, lipids, and tissue

oxygen saturation are 2.6, 7.9, and 2.5 %, respectively. For subject 1001, differences for in oxyhemoglobin, deoxyhemoglobin, and total hemoglobin concentration are 0.8, 3.2, and 3.9  $\mu\text{M}$ , respectively, while differences in water, lipids, and tissue oxygen saturation are respectively 0.7, 10.5, and 10.7 %.

Of the normal volunteers, 48% had statistical differences between left and right distal femur tissue. The magnitude of the chromophore differences at the femur between tumor and normal tissue is similar to differences between left and right tissues in normal volunteers. Average absolute value differences for volunteers in oxyhemoglobin, deoxyhemoglobin, and total hemoglobin concentration are 6.8, 1.5, and 7.7  $\mu\text{M}$ , respectively. Average differences for volunteers in water, lipids, and tissue oxygen saturation are 3.3, 5.2, and 3.3 %, respectively. For subjects 1002, 1006, and 1008, average absolute value differences for in oxyhemoglobin, deoxyhemoglobin, and total hemoglobin concentration are 2.9, 0.4, and 3.0  $\mu\text{M}$ , respectively, while differences in water, lipids, and tissue oxygen saturation are respectively 1.9, 2.0, and 3.7 %.

From Figure 4-8, photons do not reach the underlying tissue with a lipid layer thickness of 4 cm or more. If the tumor is below 1 cm or less of subcutaneous fat, 50% of photons have a maximum depth within the tumor tissue. This supports the results in Section 3.3.3 that photons are reaching the underlying tumor for the majority of subjects. However, for tumors deeper than 2.5 cm of lipids, it is unlikely the detector is measuring anything but subcutaneous fat at a source-detector separation of 28 mms.

In Chapter 3, subject 1006 showed contrast between tumor and contralateral normal tissue (Figures 3-2d, 3-3d, 3-5d, 3-6d) despite having a tumor 32.23 mm below the surface of the skin (Table 3.5). While it is possible that a few far-reaching photons contributed to the contrast, the PHD estimates and Monte Carlo simulations in Sections 3.3.3 and 4.3.5 show that it is unlikely. The contrast could be from peritumoral

effects surrounding the tumor, such as inflammation and edema, which may also be important indicators of treatment response.

Three subjects could not be measured with DOSI. For one subject, the tumor location was too sensitive to touch. Tactile sensitivity will be a limitation of the technology. For two other subjects both diagnosed with osteosarcoma of the proximal tibia, the DOSI SNR was too low. Unfortunately, these subjects were nonresponders. Normal volunteer measurements did not have low SNR at the tibia. It is possible that some characteristic of the nonresponding tumor is causing the low signal.

The 3-mm APD shows promising results for measuring more attenuating tumors that are deeper within tissue. With the implementation of the 3-mm APD with the new handheld probe, hopefully a larger portion of the sarcoma population can be measured and characterized.

## **5.2 Future directions**

### **5.2.1 Instrumentation and measurement procedures**

After normal volunteer and clinical measurements, simulations, and testing, it is not recommended to include 658 nm as a wavelength in future iterations of DOSI technology. Even though the more sensitive 3-mm APD shows improvements for 658 nm in SNR, source-detector separation, and optical property measurements, hemoglobin absorbs so strongly at wavelengths  $<700$  nm it is recommended to use longer wavelengths for better SNR and deeper imaging.

Point measurements are time consuming and labor intensive. While the proposed instrumentation suggests another point-scanning hand held device, recent technology advances could make grid and point-by-point measurements obsolete. Digital Diffuse Optical Spectroscopic Imaging (dDOSI) is a newer DOSI technology platform developed by the BOTLab that uses direct digital synthesizers (DDS) and analog to

digital converters (ADC) to generate and measure frequency amplitude modulated signals. dDOSI eliminates the need for sequential laser modulation, using wavelength multiplexing to acquire measurements at 97 Hz (Torjesen et al., 2017). With better detectors and faster measurement acquisition speeds, new scanning methods are possible. For example, a mechanical gear system scanned a fiber coupled source and detector about a single point (Applegate and Roblyer, 2018). Translations of the gear system allowed for 3D tomographic imaging. Not only is the instrumentation speeds improving, but the data processing speeding are too: acquiring optical properties and chromophore concentrations in real-time is now possible using neural networks (Zhao et al., 2018; Zhao et al., 2019). Wearable technology is proliferative, and the BOTLab has created a continuous wave wearable device for continuous monitoring during neoadjuvant chemotherapy (Teng et al., 2017). Given that absolute concentrations may not set prognostic thresholds, the continuous wave wearable may be a new direction for noninvasive monitoring in the clinic.

Even without these advances in measurement acquisition and scanning, a grid may not be necessary to detect relevant changes between normal and affected tissue. A few measurements at the most clinically relevant points may be enough to establish differences in tissue and monitor response.

### **5.2.2 Processing model**

As previously discussed in Sections 2.4.1 and 3.4.1, the choice of chromophores and light propagation model are potential limitations to this project.

The current model assumes a homogeneous sample and reported optical properties and functional information are an averaged value for the underlying tissues. A two-layer model could improve measurements of tumor optical properties and hemodynamics (Tabassum et al., 2018). Given the diversity of anatomic locations common to sarcomas and body types, it is recommended to use a model where lipid layer thick-



ness does not need to be known (Pifferi et al., 2001).

Choice of chromophores was a potential limitation of this project. The main constituents of bone is hydroxyapatite (mineral), collagen, and water (Gul-E-Noor et al., 2015). Methemoglobin has been observed in osteosarcomas using MRI (Hosalkar and Dormans, 2004). Inclusion of additional chromophores might improve the prognostic capabilities of DOSI during neoadjuvant chemotherapy monitoring. However, if collagen is to be included as a chromophore, careful studies showing validating diffuse optical measurements with physiologically relevant concentrations will be necessary.

### **5.2.3 Clinical studies**

Until the recent advances in technology are ready for the clinic, there are still questions to be answered with the hand held probe. This project suffers from small sample sizes. While being one of the most comprehensive studies with 25 normal volunteers and 9 sarcoma subjects, large subject variability necessitates larger sample sizes in order to establish the generalizability of DOSI results for different ethnicities, ages, and genders. Establishing the generalizability of DOSI measurements could elucidate important chromophore similarities and differences between populations of interest (Meertens et al., 2018).

Results from Chapter 2 show pediatric and adult populations have different chromophore concentrations and preliminary results suggest sex differences in chromophore concentrations. These results could be sample bias stemming from the small number of volunteers measured or reflective of underlying biological differences, such as fat storage and metabolism (Shi and Clegg, 2009; Power and Schulkin, 2008). The study in Chapter 2 is not powered to answer these questions. However, preliminary results show a strong correlation between lipid and hemoglobin concentration. Future analyses should explore using lipids as a covariate which may explain variation within the population and eliminate the need for different prognostic standards between

pediatric and adult populations or between men and women.

Chapter 2 is the first study to quantify chromophore variation within individuals and populations. This information will be a powerful tool for creating future studies. For example, Chapter 3 shows that local optical contrast exists between tumor and contralateral normal regions in sarcomas, however, it is still unclear if contrast exists between sarcomas and the normal population.

### **5.3 Concluding remarks**

Identification of a prognostic marker to improve sarcoma patient survival is a priority. This project is an important step toward that objective. DOSI can measure bony locations and sarcomas. While diffuse optical technologies have incredible potential, development of useful NIR diagnostic thresholds have been hampered by wide variation in results (Meertens et al., 2018). This project quantifies and characterizes functional hemodynamic information which will serve future researchers in study design and analysis. With the instrumentation improvements developed in this project and further characterization of tissues, I remain optimistic that a prognostic marker will be found.

## Appendix A

# Optical properties from literature

Table A.1: Bone optical properties.

Tissue Location	Species	Wavelength (nm)	$\mu_a$ ( $\text{mm}^{-1}$ )	$\mu'_s$ ( $\text{mm}^{-1}$ )	Reference
bone	horse	600	0.065	N/A	(Ugryumova et al., 2004)
cartilage	rabbit	632.8	0.033	1.94	(Beek et al., 1997)
skull	porcine	650	0.04	2.625	(Firbank et al., 1993)
bone matrix	bovine	658	0.007	3	(Pifferi et al., 2004)
humerus	human	659	0.006	0.55	(Peterson et al., 2017)
femur	human	659	0.008	0.98	(Peterson et al., 2017)
rib	human	659	0.015	0.83	(Peterson et al., 2017)
femur	human	659	0.01	1.29	(Peterson et al., 2017)
patella	human	690	0.0038	0.74	(Farzam et al., 2013)
manubrium	human	690	0.014	1.01	(Farzam et al., 2014)
bone	chicken	785	0.021	1.75	(Xu et al., 2001)
patella	human	785	0.0035	0.54	(Farzam et al., 2013)
manubrium	human	785	0.015	0.96	(Farzam et al., 2014)
PIP finger bones	human	785	0.023	2.14	(Xu et al., 2001)
PIP joint	human	785	0.011	1.81	(Xu et al., 2001)
head	human	800	0.016	0.94	(Matcher et al., 1997)
patella	human	830	0.0044	0.44	(Farzam et al., 2013)
manubrium	human	830	0.016	0.87	(Farzam et al., 2014)
bone	horse	900	0.02	N/A	(Ugryumova et al., 2004)
skull	porcine	950	0.05	1.32	(Firbank et al., 1993)
bone matrix	bovine	1000	0.0138	2.4	(Pifferi et al., 2004)

**Table A.2:** Muscle optical properties.

Tissue Location	Species	Wavelength (nm)	$\mu_a$ (mm <sup>-1</sup> )	$\mu'_s$ (mm <sup>-1</sup> )	Reference
striated muscle	human	515	1.12	N/A	(Marchesini et al., 1989)
muscle	bovine	630	0.35	4.5	(McKenzie and Byrne, 1988)
muscle	porcine	630	0.12	6.21	(Beek et al., 1997)
muscle	rabbit	630	0.14	1.65	(Beek et al., 1997)
muscle	porcine	632.8	0.059	2.47	(Beek et al., 1997)
muscle	rabbit	632.8	0.074	0.44	(Beek et al., 1997)
muscle	bovine	633	0.04	0.553	(Cheong et al., 1990)
muscle	bovine	633	0.15	0.7	(Wilson et al., 1986)
muscle	bovine	633	0.17	0.44	(Karagiannes et al., 1989)
muscle	bovine	633	0.096	0.53	(Kienle et al., 1996)
breast	chicken	633	0.0038	0.42	(Kienle et al., 1996)
muscle	chicken	633	0.012	0.8	(Wilson et al., 1986)
muscle	chicken	633	0.017	0.41	(Cheong et al., 1990)
muscle	chicken	633	0.012	0.8	(Wilson et al., 1986)
abdomen	human	633	0.121	0.89	(Simpson et al., 1998)
abdomen	human	633	0.123	0.894	(Bashkatov et al., 2011)
muscle	porcine	633	0.1	0.12	(Cheong et al., 1990)
psoas major and semimembranosus	bovine	650	0.041	0.611	(Bashkatov et al., 2011)
femoral muscle	rat	650	0.056	0.553	(Bashkatov et al., 2011)
gastrocnemius (lateral distal)	human	690	0.033	1.25	(Torricelli et al., 2004)

*Continued on next page*

Table A.2 – Continued from previous page

Tissue Location	Species	Wavelength (nm)	$\mu_a$ (mm <sup>-1</sup> )	$\mu'_s$ (mm <sup>-1</sup> )	Reference
gastrocnemius (lateral distal)	human	690	0.0307	1.2	(Torriceili et al., 2004)
gastrocnemius (lateral distal)	human	690	0.034	1.25	(Torriceili et al., 2004)
gastrocnemius (lateral distal)	human	690	0.04	1.1	(Torriceili et al., 2004)
gastrocnemius (lateral proximal)	human	690	0.032	1.2	(Torriceili et al., 2004)
gastrocnemius (lateral proximal)	human	690	0.037	1.1	(Torriceili et al., 2004)
gastrocnemius (lateral proximal)	human	690	0.033	1.35	(Torriceili et al., 2004)
gastrocnemius (lateral proximal)	human	690	0.038	1.3	(Torriceili et al., 2004)
gastrocnemius (medial distal)	human	690	0.027	1.35	(Torriceili et al., 2004)
gastrocnemius (medial distal)	human	690	0.03	1.3	(Torriceili et al., 2004)
gastrocnemius (medial distal)	human	690	0.026	1.4	(Torriceili et al., 2004)
gastrocnemius (medial distal)	human	690	0.033	1.3	(Torriceili et al., 2004)
gastrocnemius (medial proximal)	human	690	0.024	1.2	(Torriceili et al., 2004)
gastrocnemius (medial proximal)	human	690	0.0275	1.1	(Torriceili et al., 2004)
gastrocnemius (medial proximal)	human	690	0.024	1.4	(Torriceili et al., 2004)
gastrocnemius (medial proximal)	human	690	0.03	1.3	(Torriceili et al., 2004)
psoas major and semimembranosus	bovine	700	0.016	0.556	(Bashkatov et al., 2011)
abdomen	human	700	0.046	0.83	(Simpson et al., 1998)
abdomen	human	700	0.048	0.818	(Bashkatov et al., 2011)
femoral muscle	rat	700	0.052	0.515	(Bashkatov et al., 2011)
psoas major and semimembranosus	bovine	750	0.011	0.511	(Bashkatov et al., 2011)
abdomen	human	750	0.041	0.771	(Bashkatov et al., 2011)

*Continued on next page*

Table A.2 – Continued from previous page

Tissue Location	Species	Wavelength (nm)	$\mu_a$ (mm <sup>-1</sup> )	$\mu'_s$ (mm <sup>-1</sup> )	Reference
femoral muscle	rat	750	0.052	0.492	(Bashkatov et al., 2011)
muscle	bovine	751	0.037	0.34	(Kienle et al., 1996)
breast	chicken	751	0.0027	0.28	(Kienle et al., 1996)
gastrocnemius (lateral distal)	human	780	0.0275	1.05	(Torriceili et al., 2004)
gastrocnemius (lateral distal)	human	780	0.03	1	(Torriceili et al., 2004)
gastrocnemius (lateral distal)	human	780	0.0275	1	(Torriceili et al., 2004)
gastrocnemius (lateral distal)	human	780	0.03	0.9	(Torriceili et al., 2004)
gastrocnemius (lateral proximal)	human	780	0.026	0.95	(Torriceili et al., 2004)
gastrocnemius (lateral proximal)	human	780	0.03	0.9	(Torriceili et al., 2004)
gastrocnemius (lateral proximal)	human	780	0.027	1.1	(Torriceili et al., 2004)
gastrocnemius (lateral proximal)	human	780	0.029	1	(Torriceili et al., 2004)
gastrocnemius (medial distal)	human	780	0.025	1.25	(Torriceili et al., 2004)
gastrocnemius (medial distal)	human	780	0.027	1.05	(Torriceili et al., 2004)
gastrocnemius (medial distal)	human	780	0.024	1.2	(Torriceili et al., 2004)
gastrocnemius (medial distal)	human	780	0.027	1.1	(Torriceili et al., 2004)
gastrocnemius (medial proximal)	human	780	0.026	0.9	(Torriceili et al., 2004)
gastrocnemius (medial proximal)	human	780	0.03	0.8	(Torriceili et al., 2004)
gastrocnemius (medial proximal)	human	780	0.025	1.2	(Torriceili et al., 2004)
gastrocnemius (medial proximal)	human	780	0.027	1.1	(Torriceili et al., 2004)
muscle	rabbit	790	0.23	0.68	(Beek et al., 1997)
psoas major and semimembranosus	bovine	800	0.09	0.471	(Bashkatov et al., 2011)

*Continued on next page*

Table A.2 – Continued from previous page

Tissue Location	Species	Wavelength (nm)	$\mu_a$ ( $\text{mm}^{-1}$ )	$\mu'_s$ ( $\text{mm}^{-1}$ )	Reference
abdomen	human	800	0.028	0.704	(Bashkatov et al., 2011)
calf	human	800	0.017	0.94	(Matcher et al., 1997)
forearm	human	800	0.023	0.68	(Matcher et al., 1997)
femoral muscle	rat	800	0.054	0.467	(Bashkatov et al., 2011)
psoas major and semimembranosus	bovine	850	0.011	0.435	(Bashkatov et al., 2011)
abdomen	human	850	0.03	0.667	(Bashkatov et al., 2011)
psoas major and semimembranosus	bovine	900	0.015	0.409	(Bashkatov et al., 2011)
abdomen	human	900	0.032	0.59	(Simpson et al., 1998)
abdomen	human	900	0.032	0.621	(Bashkatov et al., 2011)
psoas major and semimembranosus	bovine	950	0.026	0.357	(Bashkatov et al., 2011)
abdomen	human	950	0.046	0.59	(Bashkatov et al., 2011)
abdomen	human	1000	0.051	0.573	(Bashkatov et al., 2011)
muscle	porcine	1060	0.2	N/A	(Cheong et al., 1990)
muscle	bovine	1064	0.12	0.28	(Karagiannes et al., 1989)



**Table A.3:** Lipid optical properties.

Tissue Location	Species	Wavelength (nm)	$\mu_a$ ( $\text{mm}^{-1}$ )	$\mu'_s$ ( $\text{mm}^{-1}$ )	Reference
abdominal subdermal tissue (fat)	human	640	0.013	1.25	(Simpson et al., 1997)
abdominal subdermal tissue (fat)	human	650	0.011	1.2	(Simpson et al., 1997)
abdominal subdermal tissue (fat)	human	670	0.01	1.2	(Simpson et al., 1997)
abdominal subdermal tissue (fat)	human	800	0.01	1.2	(Simpson et al., 1997)
adipose	bovine	633	0.0026	1.2	(Kienle et al., 1996)
adipose	bovine	751	0.0021	1	(Kienle et al., 1996)
adipose breast	human	640	0.0045	1.18	(Taroni et al., 2009)
adipose breast	human	660	0.0035	1.15	(Taroni et al., 2009)
adipose breast	human	700	0.07	0.86	(Peters et al., 1990)
adipose breast	human	900	0.075	0.79	(Peters et al., 1990)
fat tissue	simulation	920	0.03	1.2	(Wassmer et al., 2009)
fat tissue	simulation	920	0.1	1.2	(Wassmer et al., 2009)
fat tissue	simulation	980	0.1	1.17	(Wassmer et al., 2009)
fat tissue	simulation	1064	0.08	1.15	(Wassmer et al., 2009)
subcutaneous adipose tissue	human	633	0.013	1.26	(Simpson et al., 1998)
subcutaneous adipose tissue	human	650	0.012	1.25	(Simpson et al., 1998)
subcutaneous globular fat cells	human	633	0.012	1.258	(Bashkatov et al., 2011)
subcutaneous globular fat cells	human	700	0.009	1.21	(Bashkatov et al., 2011)
subcutaneous globular fat cells	human	750	0.009	1.175	(Bashkatov et al., 2011)
subcutaneous globular fat cells	human	800	0.008	1.14	(Bashkatov et al., 2011)

*Continued on next page*

Table A.3 – *Continued from previous page*

Tissue Location	Species	Wavelength (nm)	$\mu_a$ ( $\text{mm}^{-1}$ )	$\mu'_s$ ( $\text{mm}^{-1}$ )	Reference
subcutaneous globular fat cells	human	850	0.009	1.117	(Bashkatov et al., 2011)
subcutaneous globular fat cells	human	900	0.012	1.095	(Bashkatov et al., 2011)
subcutaneous globular fat cells	human	950	0.015	1.081	(Bashkatov et al., 2011)
subcutaneous globular fat cells	human	1000	0.012	1.071	(Bashkatov et al., 2011)

## Appendix B

### Phantom recipe

The following recipes were developed to create phantoms with specific  $\mu_a$  and  $\mu'_s$  values. The  $\mu_a$  and  $\mu'_s$  values of all phantoms in the Biomedical Optical Technologies Lab (BOTLab) taller than 2 cm with recorded nigrosin and TiO<sub>2</sub> concentrations were measured by the 0.5-mm APD with a 22 mm source-detector separation 3 times. Phantoms with a negative scattering slope when fit to a power law and with a 90th percentile SNR greater than 3 at 658 nm were included in the dataset.

As shown in Figure B.1, the average  $\mu_a$  and  $\mu'_s$  were plotted against their corresponding nigrosin-to-silicone and TiO<sub>2</sub>-to-silicone ratios. From linear regressions, the following equations were identified and used to calculate the appropriate concentrations of nigrosin and TiO<sub>2</sub> for a given silicone volume ( $V$ ),  $\mu_a$  (equation B.1), and  $\mu'_s$  (equation B.2).

$$nigrosin = V(0.1382\mu_a + 0.0001) \quad (\text{B.1})$$

$$TiO_2 = V(0.0009\mu'_s + 0.00005) \quad (\text{B.2})$$

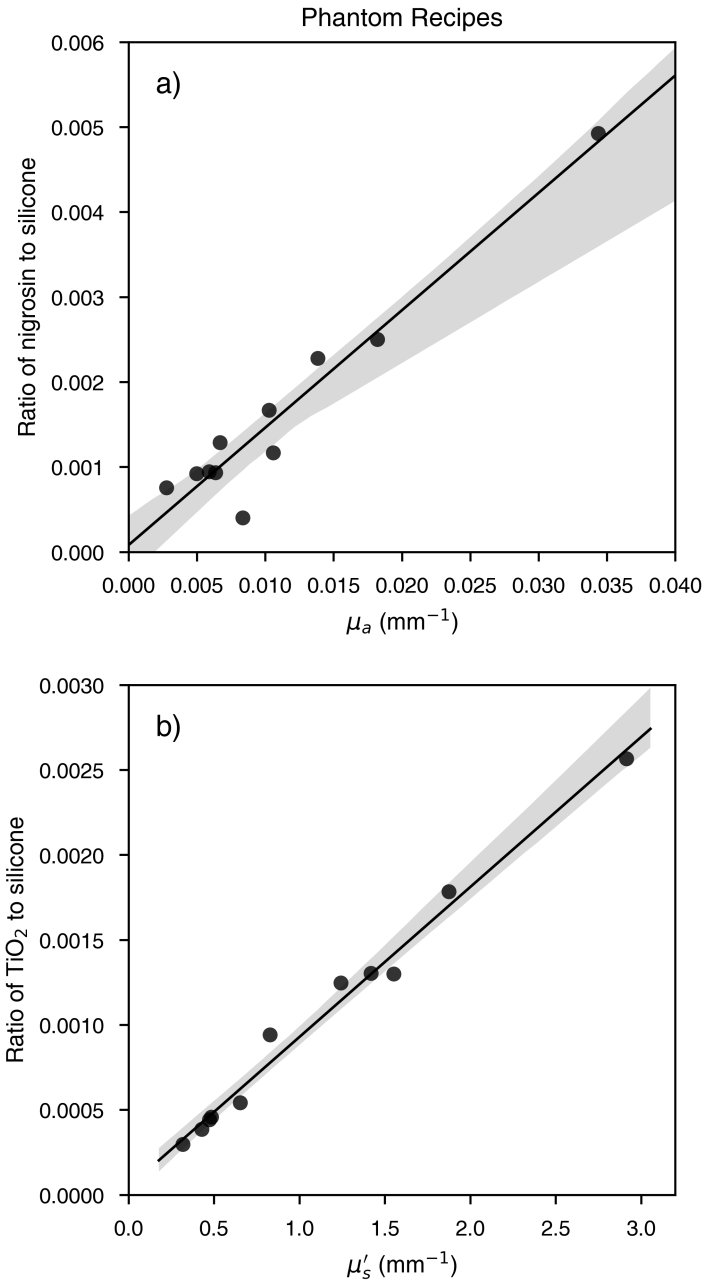


**Figure B.1:** Recipes (line) with a 95% confidence interval for silicone tissue-mimicking with specific (a)  $\mu_a$  and (b)  $\mu'_s$  values at 658 nm.

The protocol for phantom making is the following:

Materials:

- 1.5 g/L H<sub>2</sub>O nigrosin solution
- titanium dioxide (TiO<sub>2</sub>)
- curing agent
- uncured silicone
- easy release
- mixing container
- mold container
- hand-held power tool
- vacuum chamber
- sonicator

Instructions:

1. Calculate and measure quantities of 1.5 g/L H<sub>2</sub>O nigrosin solution and TiO<sub>2</sub>
2. Manually mix TiO<sub>2</sub> and 60 mL of curing agent
3. Sonicate TiO<sub>2</sub> mixture for 1–3 hours
4. Ten minutes prior to end of sonication, pour 600 mL of uncured silicone into mixing container
5. Add desired amount of 1.5 g/L H<sub>2</sub>O nigrosin solution to uncured silicon and mix for 10 min using a hand-held power tool
6. Add TiO<sub>2</sub> mixture to silicone/nigrosin mixture and mix for 5 min

7. Place mixture into vacuum chamber for maximum of 30 min (surface of mixture should be smooth with no bubbles)
8. Spray mold with easy release
9. Pour bubble-free mixture into mold
10. Place mold back in vacuum chamber, and let sit 24 hours

## References

- Applegate, M. B. and Roblyer, D. (2018). Multi-distance diffuse optical spectroscopy with a single optode via hypotrochoidal scanning. *Optics Letters*, 43(4):747–750.
- Asha, K., Sachin, A., and Muzammil, S. (2012). Chemotherapy in Osteosarcoma. In Agarwal, M., editor, *Osteosarcoma*. InTech.
- Bacci, G., Bertoni, F., Longhi, A., Ferrari, S., Forni, C., Biagini, R., Bacchini, P., Donati, D., Manfrini, M., Bernini, G., and Lari, S. (2003). Neoadjuvant chemotherapy for high-grade central osteosarcoma of the extremity. *Cancer*, 97(12):3068–3075.
- Bacci, G., Longhi, A., Fagioli, F., Briccoli, A., Versari, M., and Picci, P. (2005). Adjuvant and neoadjuvant chemotherapy for osteosarcoma of the extremities: 27 year experience at Rizzoli Institute, Italy. *European Journal of Cancer*, 41(18):2836–2845.
- Bacci, G., Longhi, A., Versari, M., Mercuri, M., Briccoli, A., and Picci, P. (2006). Prognostic factors for osteosarcoma of the extremity treated with neoadjuvant chemotherapy. *Cancer*, 106(5):1154–1161.
- Bajpai, J., Shivanand Gammagatti, Rakesh Kumar, Vishnubhatla Sreenivas, Mehar Chand Sharma, Shah Alam Khan, Shishir Rastogi, Arun Malhotra, Rajni Safaya, and Sameer Bakhshi (2011). Role of MRI in osteosarcoma for evaluation and prediction of chemotherapy response: correlation with histological necrosis. *Pediatric Radiology*, 41(4):441–450.
- Bashkatov, A. N., Genina, E. A., Kochubey, V. I., and Tuchin, V. V. (2005). Optical properties of human skin, subcutaneous and mucous tissues in the wavelength range from 400 to 2000 nm. *Journal of Physics D: Applied Physics*, 38:2543–2555.
- Bashkatov, A. N., Genina, E. A., and Tuchin, V. V. (2011). Optical properties of skin, subcutaneous, and muscle tissues: a review. *Journal of Innovative Optical Health Sciences*, 04(01):9–38.
- Beek, J. F., Blokland, P., Posthumus, P., Aalders, M., Pickering, J. W., Sterenborg, H. J., and van Gemert, M. J. (1997). In vitro double-integrating-sphere optical properties of tissues between 630 and 1064 nm. *Physics in Medicine and Biology*, 42(11):2255–2261.

- Bernstein, M., Kovar, H., Paulussen, M., Randall, R. L., Schuck, A., Teot, L. A., and Juergens, H. (2006). Ewings Sarcoma Family of Tumors: Current Management. *The Oncologist*, 11(5):503–519.
- Beta Technology (2008). Lange Skinfold Caliper Operators Manual. Technical report, Beta Technology, Santa Cruz, CA, USA.
- Bevilacqua, F., Berger, A. J., Cerussi, A. E., Jakubowski, D., and Tromberg, B. J. (2000). Broadband absorption spectroscopy in turbid media by combined frequency-domain and steady-state methods. *Applied Optics*, 39(34):6498–6507.
- Bielack, S. S., Kempf-Bielack, B., Delling, G., Exner, G. U., Flege, S., Helmke, K., Kotz, R., Salzer-Kuntschik, M., Werner, M., Winkelmann, W., Zoubek, A., Jrgens, H., Winkler, K., and Group, f. t. C. G.-A.-S. O. S. (2002). Prognostic Factors in High-Grade Osteosarcoma of the Extremities or Trunk: An Analysis of 1,702 Patients Treated on Neoadjuvant Cooperative Osteosarcoma Study Group Protocols. *Journal of Clinical Oncology*, 20(3):776–790.
- Bieling, P., Rehan, N., Winkler, P., Helmke, K., Maas, R., Fuchs, N., Bielack, S., Heise, U., Jurgens, H., Treuner, J., Romanowski, R., Exner, U., Kotz, R., and Winkler, K. (1996). Tumor size and prognosis in aggressively treated osteosarcoma. *Journal of Clinical Oncology*, 14(3):848–858.
- Biermann, J. S., Adkins, D. R., Agulnik, M., Benjamin, R. S., Brigman, B., Butrynski, J. E., Cheong, D., Chow, W., Curry, W. T., Frassica, D. A., Frassica, F. J., Hande, K. R., Hornicek, F. J., Jones, R. L., Mayerson, J., McGarry, S. V., McGrath, B., Morris, C. D., O’Donnell, R. J., Randall, R. L., Santana, V. M., Satcher, R. L., Siegel, H. J., Mehren, M. v., Bergman, M. A., and Sundar, H. (2013). Bone Cancer. *Journal of the National Comprehensive Cancer Network*, 11(6):688–723.
- Binzoni, T., Sassaroli, A., Torricelli, A., Spinelli, L., Farina, A., Durduran, T., Cavalieri, S., Pifferi, A., and Martelli, F. (2017). Depth sensitivity of frequency domain optical measurements in diffusive media. *Biomedical Optics Express*, 8(6):2990–3004.
- Calabro, K. W. (2013). *Improved mathematical and computational tools for modeling photon propagation in tissue*. PhD thesis, Boston University, Boston, MA.
- Carrle, D. and Bielack, S. S. (2006). Current strategies of chemotherapy in osteosarcoma. *International Orthopaedics*, 30(6):445–451.
- Cerussi, A., Shah, N., Hsiang, D., Durkin, A., Butler, J., and Tromberg, B. J. (2006). In vivo absorption, scattering, and physiologic properties of 58 malignant breast tumors determined by broadband diffuse optical spectroscopy. *Journal of Biomedical Optics*, 11(4):044005–044005–16.



- Cerussi, A. E., Tanamai, V. W., Hsiang, D., Butler, J., Mehta, R. S., and Tromberg, B. J. (2011). Diffuse optical spectroscopic imaging correlates with final pathological response in breast cancer neoadjuvant chemotherapy. *Philosophical Transactions of the Royal Society of London A: Mathematical, Physical and Engineering Sciences*, 369(1955):4512–4530.
- Chance, B., Nioka, S., Kent, J., McCully, K., Fountain, M., Greenfeld, R., and Holtom, G. (1988). Time-resolved spectroscopy of hemoglobin and myoglobin in resting and ischemic muscle. *Analytical Biochemistry*, 174(2):698–707.
- Cheong, W. F., Prael, S. A., and Welch, A. J. (1990). A review of the optical properties of biological tissues. *IEEE Journal of Quantum Electronics*, 26(12):2166–2185.
- Cochran, J. M., Chung, S. H., Leproux, A., Baker, W. B., Busch, D. R., DeMichele, A. M., Tchou, J., Tromberg, B. J., and Yodh, A. G. (2017). Longitudinal optical monitoring of blood flow in breast tumors during neoadjuvant chemotherapy. *Physics in Medicine & Biology*, 62(12):4637.
- Dahlin, D. C. and Coventry, M. B. (1967). Osteogenic Sarcoma. *J Bone Joint Surg Am*, 49(1):101–110.
- Davis, A. M., Bell, R. S., and Goodwin, P. J. (1994). Prognostic factors in osteosarcoma: a critical review. *Journal of Clinical Oncology*, 12(2):423–431.
- Doornbos, R. M. P., Lang, R., Aalders, M. C., Cross, F. W., and Sterenberg, H. J. C. M. (1999). The determination of in vivo human tissue optical properties and absolute chromophore concentrations using spatially resolved steady-state diffuse reflectance spectroscopy. *Physics in Medicine and Biology*, 44(4):967.
- Erickson, T. A., Mazhar, A., Cuccia, D. J., Durkin, A. J., and Tunnell, J. W. (2010). Lookup-table method for imaging optical properties with structured illumination beyond the diffusion theory regime. *Journal of Biomedical Optics*, 15(3):036013.
- Facey, K., Bradbury, I., Laking, G., and Payne, E. (2007). Overview of the clinical effectiveness of positron emission tomography imaging in selected cancers. *Health Technology Assessment*, 11(44).
- Farzam, P., Lindner, C., Weigel, U. M., Suarez, M., Urbano-Ispizua, A., and Durduran, T. (2014). Noninvasive characterization of the healthy human manubrium using diffuse optical spectroscopies. *Physiological Measurement*, 35(7):1469.
- Farzam, P., Zirak, P., Binzoni, T., and Durduran, T. (2013). Pulsatile and steady-state hemodynamics of the human patella bone by diffuse optical spectroscopy. *Physiological Measurement*, 34(8):839.

- Firbank, M., Hiraoka, M., Essenpreis, M., and Delpy, D. T. (1993). Measurement of the optical properties of the skull in the wavelength range 650-950 nm. *Physics in Medicine and Biology*, 38(4):503–510.
- Gul-E-Noor, F., Singh, C., Papaioannou, A., Sinha, N., and Boutis, G. S. (2015). The Behavior of Water in Collagen and Hydroxyapatite Sites of Cortical Bone: Fracture, Mechanical Wear, and Load Bearing Studies. *The journal of physical chemistry. C, Nanomaterials and interfaces*, 119(37):21528–21537.
- Hamamatsu Photonics. IR-enhanced Si APD S11519-30. Technical report, Hamamatsu Photonics, Ichino-cho, Higashi-ku, Hamamatsu City, Japan.
- Haskell, R. C., Svaasand, L. O., Tsay, T.-T., Feng, T.-C., McAdams, M. S., and Tromberg, B. J. (1994). Boundary conditions for the diffusion equation in radiative transfer. *Journal of the Optical Society of America A*, 11(10):2727.
- Hauben, E. I., Weeden, S., Pringle, J., Van Marck, E. A., and Hogendoorn, P. C. W. (2002). Does the histological subtype of high-grade central osteosarcoma influence the response to treatment with chemotherapy and does it affect overall survival? A study on 570 patients of two consecutive trials of the European Osteosarcoma Intergroup. *European Journal of Cancer*, 38(9):1218–1225.
- Hosalkar, H. S. and Dormans, J. P. (2004). Limb sparing surgery for pediatric musculoskeletal tumors. *Pediatric Blood & Cancer*, 42(4):295–310.
- Howlander, N., Noone, A., Krapcho, M., Miller, D., Bishop, K., Kosary, C., Yu, M., Ruhl, J., Tatalovich, Z., Mariotto, A., Lewis, D., Chen, H., Feuer, E., and Cronin, K. (2016). SEER Cancer Statistics Review, 1975-2013. Technical report, National Cancer Institute. Bethesda, MD, Bethesda, MD.
- Jacques, S. L. (2013). Optical properties of biological tissues: a review. *Physics in Medicine & Biology*, 58(11):R37.
- Jones, E., Travis Oliphant, Pearu Peterson, and others (2001). SciPy: Open source scientific tools for Python.
- Karagiannes, J. L., Zhang, Z., Grossweiner, B., and Grossweiner, L. I. (1989). Applications of the 1-D diffusion approximation to the optics of tissues and tissue phantoms. *Applied Optics*, 28(12):2311–2317.
- Kienle, A., Lilge, L., Patterson, M. S., Hibst, R., Steiner, R., and Wilson, B. C. (1996). Spatially resolved absolute diffuse reflectance measurements for noninvasive determination of the optical scattering and absorption coefficients of biological tissue. *Applied Optics*, 35(13):2304–2314.

- Klein, M. J. and Siegal, G. P. (2006). Osteosarcoma: Anatomic and Histologic Variants. *American Society for Clinical Pathology*, 125:555–581.
- Kou, L., Labrie, D., and Chylek, P. (1993). Refractive indices of water and ice in the 0.65- to 2.5- $\mu$ m spectral range. *Applied Optics*, 32(19):3531–3540.
- Kreuter, M., Bieker, R., Bielack, S. S., Auras, T., Buerger, H., Gosheger, G., Jurgens, H., Berdel, W. E., and Mesters, R. M. (2004). Prognostic Relevance of Increased Angiogenesis in Osteosarcoma. *Clinical Cancer Research*, 10(24):8531–8537.
- Levine, A. M. and Rosenberg, S. A. (1979). Alkaline phosphatase levels in osteosarcoma tissue are related to prognosis. *Cancer*, 44(6):2291–2293.
- Link, M. P., Goorin, A. M., Miser, A. W., Green, A. A., Pratt, C. B., Belasco, J. B., Pritchard, J., Malpas, J. S., Baker, A. R., Kirkpatrick, J. A., Ayala, A. G., Shuster, J. J., Abelson, H. T., Simone, J. V., and Vietti, T. J. (1986). The Effect of Adjuvant Chemotherapy on Relapse-Free Survival in Patients with Osteosarcoma of the Extremity. *New England Journal of Medicine*, 314(25):1600–1606.
- Lodish, H., Berk, A., Zipursky, S. L., Matsudaira, P., Baltimore, D., and Darnell, J. (2000). Collagen: The Fibrous Proteins of the Matrix.
- Marchesini, R., Bertoni, A., Andreola, S., Melloni, E., and Sichirollo, A. E. (1989). Extinction and absorption coefficients and scattering phase functions of human tissues in vitro. *Applied Optics*, 28(12):2318–2324.
- Marina, N., Gebhardt, M., Teot, L., and Gorlick, R. (2004). Biology and Therapeutic Advances for Pediatric Osteosarcoma. *The Oncologist*, 9(4):422–441.
- Markus Uhl, Ulrich Saueressig, Gabriele Koehler, Udo Kontny, Charlotte Niemeyer, Wilfried Reichardt, Kamil Ilyasof, Thorsten Bley, and Mathias Langer (2006). Evaluation of tumour necrosis during chemotherapy with diffusion-weighted MR imaging: preliminary results in osteosarcomas. *Pediatric Radiology*, 36(12):1306–1311.
- Matcher, S. J., Cope, M., and Delpy, D. T. (1997). In vivo measurements of the wavelength dependence of tissue-scattering coefficients between 760 and 900 nm measured with time-resolved spectroscopy. *Applied Optics*, 36(1):386–396.
- McKenzie, A. L. and Byrne, P. O. (1988). Can photography be used to measure isodose distributions of space irradiance for laser photodynamic therapy? *Physics in Medicine and Biology*, 33(1):113–131.
- Meertens, R., Casanova, F., Knapp, K. M., Thorn, C., and Strain, W. D. (2018). Use of near-infrared systems for investigations of hemodynamics in human in vivo bone tissue: A systematic review. *Journal of Orthopaedic Research*, 36(10):2595–2603.

- Mehren, M. v., Randall, R. L., Benjamin, R. S., Boles, S., Bui, M. M., Casper, E. S., Conrad, E. U., DeLaney, T. F., Ganjoo, K. N., George, S., Gonzalez, R. J., Heslin, M. J., Kane, J. M., Mayerson, J., McGarry, S. V., Meyer, C., O'Donnell, R. J., Pappo, A. S., Paz, I. B., Pfeifer, J. D., Riedel, R. F., Schuetze, S., Schupak, K. D., Schwartz, H. S., Tine, B. A. V., Wayne, J. D., Bergman, M. A., and Sundar, H. (2014). NCCN Guidelines Soft Tissue Sarcoma, Version 2.2014. *Journal of the National Comprehensive Cancer Network*, 12(4):473–483.
- Meyers, P. A., Heller, G., Healey, J., Huvos, A., Lane, J., Marcove, R., Applewhite, A., Vlamis, V., and Rosen, G. (1992). Chemotherapy for nonmetastatic osteogenic sarcoma: the Memorial Sloan-Kettering experience. *Journal of Clinical Oncology*, 10(1):5–15.
- Mirabello, L., Troisi, R. J., and Savage, S. A. (2009). Osteosarcoma incidence and survival rates from 1973 to 2004. *Cancer*, 115(7):1531–1543.
- Moffat, B. A., Chenevert, T. L., Meyer, C. R., Mckeever, P. E., Hall, D. E., Hoff, B. A., Johnson, T. D., Rehemtulla, A., and Ross, B. D. (2006). The Functional Diffusion Map: An Imaging Biomarker for the Early Prediction of Cancer Treatment Outcome. *Neoplasia (New York, N. Y.)*, 8(4):259–267.
- National Cancer Institute. SEER Cancer Statistics Factsheets: Bone and Joint Cancer. <http://seer.cancer.gov/statfacts/html/bones.html>, Bethesda, MD.
- National Cancer Institute. SEER Cancer Statistics Factsheets: Soft Tissue including Heart Cancer. <http://seer.cancer.gov/statfacts/html/soft.html>, Bethesda, MD.
- No, K.-S., Kwong, R., Chou, P. H., and Cerussi, A. (2008). Design and testing of a miniature broadband frequency domain photon migration instrument. *Journal of biomedical optics*, 13(5):050509.
- Peters, V. G., Wyman, D. R., Patterson, M. S., and Frank, G. L. (1990). Optical properties of normal and diseased human breast tissues in the visible and near infrared. *Physics in Medicine and Biology*, 35(9):1317–1334.
- Peterson, H. M., Hoang, B. H., Geller, D., Yang, R., Gorlick, R., Berger, J., Tingling, J., Roth, M., Gill, J., and Roblyer, D. (2017). In vivo, noninvasive functional measurements of bone sarcoma using diffuse optical spectroscopic imaging. *Journal of Biomedical Optics*, 22(12):121612.
- Pham, T. H., Coquoz, O., Fishkin, J. B., Anderson, E., and Tromberg, B. J. (2000). Broad bandwidth frequency domain instrument for quantitative tissue optical spectroscopy. *Review of Scientific Instruments*, 71(6):2500–2513.

- Pifferi, A., Torricelli, A., Taroni, P., Bassi, A., Chikoidze, E., Giambattistelli, E., and Cubeddu, R. (2004). Optical biopsy of bone tissue: a step toward the diagnosis of bone pathologies. *Journal of Biomedical Optics*, 9(3):474–480.
- Pifferi, A., Torricelli, A., Taroni, P., and Cubeddu, R. (2001). Reconstruction of absorber concentrations in a two-layer structure by use of multidistance time-resolved reflectance spectroscopy. *Optics Letters*, 26(24):1963–1965.
- Pope, R. M. and Fry, E. S. (1997). Absorption spectrum (380700 nm) of pure water. II. Integrating cavity measurements. *Applied Optics*, 36(33):8710–8723.
- Power, M. L. and Schulkin, J. (2008). Sex differences in fat storage, fat metabolism, and the health risks from obesity: possible evolutionary origins. *British Journal of Nutrition*, 99(5):931–940.
- Provisor, A. J., Ettinger, L. J., Nachman, J. B., Krailo, M. D., Makley, J. T., Yunis, E. J., Huvos, A. G., Betcher, D. L., Baum, E. S., Kisker, C. T., and Miser, J. S. (1997). Treatment of nonmetastatic osteosarcoma of the extremity with preoperative and postoperative chemotherapy: a report from the Children’s Cancer Group. *Journal of Clinical Oncology*, 15(1):76–84.
- Python Software Foundation (2015). Python.
- Rakheja, R., Makis, W., Tulbah, R., Skamene, S., Holcroft, C., Nahal, A., Turcotte, R., and Hickeyson, M. (2013). Necrosis on FDG PET/CT Correlates With Prognosis and Mortality in Sarcomas. *American Journal of Roentgenology*, 201(1):170–177.
- Roblyer, D., Ueda, S., Cerussi, A., Tanamai, W., Durkin, A., Mehta, R., Hsiang, D., Butler, J. A., McLaren, C., Chen, W.-P., and Tromberg, B. (2011). Optical imaging of breast cancer oxyhemoglobin flare correlates with neoadjuvant chemotherapy response one day after starting treatment. *Proceedings of the National Academy of Sciences*, 108(35):14626–14631.
- Rosen, G., Marcove, R. C., Caparros, B., Nirenberg, A., Kosloff, C., and Huvos, A. G. (1979). Primary osteogenic sarcoma. The rationale for preoperative chemotherapy and delayed surgery. *Cancer*, 43(6):2163–2177.
- Salomatina, E. V., Jiang, B., Novak, J., and Yaroslavsky, A. N. (2006). Optical properties of normal and cancerous human skin in the visible and near-infrared spectral range. *Journal of Biomedical Optics*, 11(6):064026.
- Sanchez, R. B., Quinn, S. F., Walling, A., Estrada, J., and Greenberg, H. (1990). Musculoskeletal neoplasms after intraarterial chemotherapy: correlation of MR images with pathologic specimens. *Radiology*, 174(1):237–240.

- Sandell, J. L. and Zhu, T. C. (2011). A review of in-vivo optical properties of human tissues and its impact on PDT. *Journal of Biophotonics*, 4(11-12):773–787.
- Schotland, J. C., Haselgrove, J. C., and Leigh, J. S. (1993). Photon hitting density. *Applied Optics*, 32(4):448.
- Sekar, S. K. V., Dalla Mora, A., Bargigia, I., Martinenghi, E., Lindner, C., Farzam, P., Pagliazzi, M., Durduran, T., Taroni, P., Pifferi, A., and Farina, A. (2015a). Broadband (600-1350 nm) Time Resolved Diffuse Optical Spectrometer for Clinical Use. *IEEE Journal of Selected Topics in Quantum Electronics*, PP(99):1–1.
- Sekar, S. K. V., Farina, A., Martinenghi, E., Dalla Mora, A., Taroni, P., Pifferi, A., Negro, E., Puig, J., Escrig, R., Rosales, Q., Lindner, C., Pagliazzi, M., and Durduran, T. (2015b). Time-resolved diffused optical characterization of key tissue constituents of human bony prominence locations. volume 9538, pages 95380X–95380X–5.
- Shi, H. and Clegg, D. J. (2009). Sex differences in the regulation of body weight. *Physiology & Behavior*, 97(2):199–204.
- Simpson, C. R., Kohl, M., Essenpreis, M., and Cope, M. (1998). Near-infrared optical properties of ex vivo human skin and subcutaneous tissues measured using the Monte Carlo inversion technique. *Physics in Medicine & Biology*, 43(9):2465.
- Simpson, R., Laufer, J. G., Kohl-Bareis, M., Essenpreis, M., and Cope, M. (1997). Near-infrared optical properties of ex-vivo human skin and subcutaneous tissues using reflectance and transmittance measurements. In *Optical Tomography and Spectroscopy of Tissue: Theory, Instrumentation, Model, and Human Studies II*, volume 2979, pages 307–314. International Society for Optics and Photonics.
- Tabassum, S., Pera, V., Greening, G., Muldoon, T. J., and Roblyer, D. (2018). Two-layer inverse model for improved longitudinal preclinical tumor imaging in the spatial frequency domain. *Journal of Biomedical Optics*, 23(7):076011.
- Taroni, P., Bassi, A., Comelli, D., Farina, A., Cubeddu, R., and Pifferi, A. (2009). Diffuse optical spectroscopy of breast tissue extended to 1100 nm. *Journal of Biomedical Optics*, 14(5):054030.
- Taroni, P., Comelli, D., Pifferi, A., Torricelli, A., and Cubeddu, R. (2007). Absorption of collagen: effects on the estimate of breast composition and related diagnostic implications. *Journal of Biomedical Optics*, 12(1):014021.
- Teng, F., Cormier, T., Sauer-Budge, A., Chaudhury, R., Pera, V. E., Istfan, R., Chargin, D. A., Brookfield, S., Ko, N. Y., and Roblyer, D. M. (2017). Wearable near-infrared optical probe for continuous monitoring during breast cancer neoadjuvant chemotherapy infusions. *Journal of Biomedical Optics*, 22(1):014001.

- The ESMO/European Sarcoma Network Working Group (2014). Bone sarcomas: ESMO Clinical Practice Guidelines for diagnosis, treatment and follow-up. *Annals of Oncology*, 25(suppl 3):iii113–iii123.
- The MathWorks Inc. (2014). MATLAB.
- Torjesen, A., Istfan, R., and Roblyer, D. (2017). Ultrafast wavelength multiplexed broad bandwidth digital diffuse optical spectroscopy for in vivo extraction of tissue optical properties. *Journal of Biomedical Optics*, 22(3):036009.
- Torricelli, A., Quaresima, V., Pifferi, A., Biscotti, G., Spinelli, L., Paola Taroni, Ferrari, M., and Cubeddu, R. (2004). Mapping of calf muscle oxygenation and haemoglobin content during dynamic plantar flexion exercise by multi-channel time-resolved near-infrared spectroscopy. *Physics in Medicine & Biology*, 49(5):685.
- Tromberg, B. J., Zhang, Z., Leproux, A., O’Sullivan, T. D., Cerussi, A. E., Carpenter, P. M., Mehta, R. S., Roblyer, D., Yang, W., Paulsen, K. D., Pogue, B. W., Jiang, S., Kaufman, P. A., Yodh, A. G., Chung, S. H., Schnall, M., Snyder, B. S., Hylton, N., Boas, D. A., Carp, S. A., Isakoff, S. J., and Mankoff, D. (2016). Predicting Responses to Neoadjuvant Chemotherapy in Breast Cancer: ACRIN 6691 Trial of Diffuse Optical Spectroscopic Imaging. *Cancer Research*, 76(20):5933–5944.
- Ueda, S., Roblyer, D., Cerussi, A., Durkin, A., Leproux, A., Santoro, Y., Xu, S., O’Sullivan, T. D., Hsiang, D., Mehta, R., Butler, J., and Tromberg, B. J. (2012). Baseline Tumor Oxygen Saturation Correlates with a Pathologic Complete Response in Breast Cancer Patients Undergoing Neoadjuvant Chemotherapy. *Cancer Research*, 72(17):4318–4328.
- Ugryumova, N., Matcher, S. J., and Attenburrow, D. P. (2004). Measurement of bone mineral density via light scattering. *Physics in Medicine & Biology*, 49(3):469.
- Uribe-Botero, G., Russell, W. O., Sutow, W. W., and Martin, R. G. (1977). Primary Osteosarcoma of Bone: A Clinicopathologic Investigation of 243 Cases, with Necropsy Studies in 54. *American Journal of Clinical Pathology*, 67(5):427–435.
- van Veen, R. L. P., Sterenborg, H. j. c. m., Pifferi, A., Torricelli, A., and Cubeddu, R. (2004). Determination of VIS- NIR absorption coefficients of mammalian fat, with time- and spatially resolved diffuse reflectance and transmission spectroscopy. In *Biomedical Topical Meeting (2004)*, paper SF4, page SF4. Optical Society of America.
- Vaupel, P., Kallinowski, F., and Okunieff, P. (1989). Blood Flow, Oxygen and Nutrient Supply, and Metabolic Microenvironment of Human Tumors: A Review. *Cancer Research*, 49(23):6449–6465.

- Wassmer, B., Zemmouri, J., Rochon, P., and Mordon, S. (2009). Comparative Study of Wavelengths for Laser Lipolysis. *Photomedicine and Laser Surgery*, 28(2):185–188.
- Wilson, B. C., Patterson, M. S., and Burns, D. M. (1986). Effect of photosensitizer concentration in tissue on the penetration depth of photoactivating light. *Lasers in Medical Science*, 1(4):235–244.
- Winkler, K., Beron, G., Delling, G., Heise, U., Kabisch, H., Purfrst, C., Berger, J., Ritter, J., Jrgens, H., and Gerein, V. (1988). Neoadjuvant chemotherapy of osteosarcoma: results of a randomized cooperative trial (COSS-82) with salvage chemotherapy based on histological tumor response. *Journal of Clinical Oncology*, 6(2):329–337.
- Wittig, J. C., Bickels, J., Priebat, D., Jelinek, J., Kellar-Graney, K., Shmookler, B., and Malawer, M. M. (2002). Osteosarcoma: A Multidisciplinary Approach to Diagnosis and Treatment. *American Family Physician*, 65(6):1123–1132.
- Wunder, J. S., Paulian, G., Huvos, A. G., Heller, G., Meyers, P. A., and Healey, J. H. (1998). The Histological Response to Chemotherapy as a Predictor of the Oncological Outcome of Operative Treatment of Ewing Sarcoma\*. *J Bone Joint Surg Am*, 80(7):1020–33.
- Xu, Y., Iftimia, N., Jiang, H., Key, L. L., and Bolster, M. B. (2001). Imaging of in vitro and in vivo bones and joints with continuous-wave diffuse optical tomography. *Optics Express*, 8(7):447–451.
- Zhao, Y., Applegate, M. B., Istfan, R., and Roblyer, D. M. (2019). Quantitative frequency-domain pulse oximetry with deep neural network (DNN) real-time processing. In *Advanced Biomedical and Clinical Diagnostic and Surgical Guidance Systems XVII*, volume 10868, page 108680I. International Society for Optics and Photonics.
- Zhao, Y., Burger, W. R., Zhou, M., Bernhardt, E. B., Kaufman, P. A., Patel, R. R., Angeles, C. V., Pogue, B. W., Paulsen, K. D., and Jiang, S. (2017). Collagen quantification in breast tissue using a 12-wavelength near infrared spectral tomography (NIRST) system. *Biomedical Optics Express*, 8(9):4217–4229.
- Zhao, Y., Deng, Y., Bao, F., Peterson, H., Istfan, R., and Roblyer, D. (2018). Deep learning model for ultrafast multifrequency optical property extractions for spatial frequency domain imaging. *Optics Letters*, 43(22):5669–5672.
- Zijlstra, W. G., Buursma, A., and Assendelft, O. W. v. (2000). *Visible and Near Infrared Absorption Spectra of Human and Animal Haemoglobin: Determination and Application*. VSP. Google-Books-ID: Qn5yenybgtsC.



# CURRICULUM VITAE

## Hannah M. Peterson

Boston University • 44 Cummington Mall • Boston, MA 02215  
hannahmp@bu.edu

### Education

- |           |   |
|-----------|---|
| 2013–2019 | <b>PhD in Biomedical Engineering</b> , Boston University, Boston, MA, USA<br>NCI NRSA Fellow<br>Dissertation: <i>Clinical Feasibility of Diffuse Optical Spectroscopic Imaging in Sarcoma</i><br>Advisor: Darren Roblyer, PhD |
| 2009–2013 | <b>BS in Physics</b> , Rensselaer Polytechnic Institute, Troy, NY, USA<br><i>Magna Cum Laude</i>  |

### Additional Education

- |           |  |
|-----------|--|
| 2013–2019 | <b>Graduate Non-Matriculated Student, Health Metrics and Evaluation</b> , University of Washington, Seattle, WA, USA |
| 2009–2013 | <b>Study Abroad, Physics &amp; Astronomy</b> , University College London, London, UK                                 |

## Research Experience

2013–	<b>Graduate Researcher</b> , Biomedical Optical Technologies Lab, Boston, MA, USA
2011-2013	<b>Post-Bachelor Fellow, Optimal Resource Allocation Team</b> , Institute for Health Metrics and Evaluation, University of Washington, Seattle, WA
Summer 2013	<b>Visiting Researcher, Post-Bachelor Fellow Research Practicum</b> , Infectious Diseases Research Collaboration, Kampala, Uganda
Summer 2011	<b>Student</b> , Scientific Instrumentation Facility Machining Course, Boston, MA, USA
January 2011	<b>Summer Intern, Precision Diagnostics Team</b> , IBM Research — Zurich, Rüschlikon, Switzerland
2010–2011	<b>Student Intern</b> , Applied BioPhysics, Inc., Troy, NY, USA
Summer 2009, 2010	<b>Engineering Technician</b> , U.S. Army—ARDEC, Benét Laboratories, Watervliet, NY, USA
Summer 2008	<b>Laboratory Assistant</b> , Northern Illinois University, DeKalb, IL, USA

## Teaching Experience

Spring 2017	<b>Guest Lecturer</b> , <i>BE700: Cancer Biology and Oncology for Engineers</i> , Boston University, Boston, MA, USA
Spring 2015, 2016	<b>Graduate Teaching Fellow</b> , <i>BE515: Biomedical Instrumentation</i> , Boston University, Boston, MA, USA

## Professional Experience

March 2019	<b>AAAS CASE Fellow</b> , Washington D.C., USA
Fall 2018	<b>MIT IMPACT Fellow</b> , Cambridge, MA, USA
2017	<b>Consultant</b> , Boston University Engineering World Health, Lima, Peru
Fall 2015	<b>Student</b> , Scientific Instrumentation Facility Machining Course, Boston, MA, USA
January 2011	<b>Study Abroad</b> , “Culture and Development” course with NGO Banglanatak, Kolkata, India
Spring 2009	<b>Independent Student Researcher</b> , Rensselaer Polytechnic Institute, Troy, NY, USA
Summer 2006, 2007	<b>Crew Leader</b> , Monsanto Research and Development, Waterman, IL, USA
Summer 2005	<b>Seasonal Field Hand</b> , 2005 summer Monsanto, Waterman, IL, USA

## University Service

2018–2019	<b>Social Media Officer</b> , Boston University Biomedical Engineering Graduate Student Committee, Boston, MA, USA
2018–2019	<b>Member</b> , Quantitative Biology & Physiology Symposium Planning Committee, Boston, MA, USA
2017–2018	<b>Executive Co-Chair</b> , Boston University Biomedical Engineering Graduate Student Committee, Boston, MA, USA
2016–2017	<b>Professional Development Chair</b> , Boston University Biomedical Engineering Graduate Student Committee, Boston, MA, USA
2016–	<b>Senior Student Representative</b> , Quantitative Biology & Physiology Steering Committee, Boston, MA, USA
2014–2018	<b>Chair</b> , Quantitative Biology & Physiology Symposium Planning Committee, Boston, MA, USA
2013–2014	<b>Member</b> , Quantitative Biology & Physiology Symposium Planning Committee, Boston, MA, USA
2013–	<b>Member</b> , Graduate Women in Science and Engineering, Boston, MA, USA

## Academic and Professional Honors

May 2019	National Cancer Institute Graduate Student Recruiting Program
2018–	Ruth L. Kirschstein National Research Service Award (NRSA) Individual Predoctoral Fellowship (F31), National Cancer Institute(NCI)
2017	BU-BMC Cancer Center Travel Award
2013–2014	Quantitative Biology & Physiology Trainee, National Institute of General Medical Sciences (NIGMS)
2009–2010	Morley Science Scholarship, DeKalb County Farm Bureau
2007–2011	Emily Roebling Scholarship, Rensselaer Polytechnic Institute
2007–2011	Gilbert-Avery Foundation Scholarship
2007–2008	DeKalb County Farm Bureau Scholarship
2007	Illinois State Scholar (declined)
2007	Student of the Year Scholarship, MidWeek Newspaper/National Bank & Trust
2007	Bausch and Lomb Science Award

## Professional Memberships

2017–	American Association for Cancer Research
2017–	SPIE
2017–	Optical Society of America
2017–2018	AAAS
2013–2014	American Thoracic Society
2009–	Sigma Pi Sigma National Physics Honor Society

## Peer-Reviewed Publications

1. Zhao Y, Deng Y, Bao F, **Peterson H**, Istfan R, Roblyer D. Deep learning model for ultrafast multifrequency optical property extractions for spatial frequency domain imaging. *Opt Lett, OL*. 2018 Nov 15;43(22):5669–72.
2. Fullman N, Yearwood J, Abay SM, Abbafati C, Abd-Allah F, Abdela J, et al. Measuring performance on the Healthcare Access and Quality Index for 195 countries and territories and selected subnational locations: a systematic analysis from the Global Burden of Disease Study 2016. *The Lancet*. 2018 Jun 2;391(10136):2236–71.
3. **Peterson HM**, Hoang BH, Geller D, Yang R, Gorlick R, Berger J, et al. *In vivo*, noninvasive functional measurements of bone sarcoma using diffuse optical spectroscopic imaging. *JBO, JBOPFO*. 2017 Dec;22(12):121612.
4. Aquino P, Honda B, Jaini S, Lyubetskaya A, Hosur K, Chiu JG, et al. Coordinated regulation of acid resistance in *Escherichia coli*. *BMC Systems Biology*. 2017;11:1.
5. Thomas B, Wulf S, Bikbov B, Perico N, Cortinovis M, Vaccaro KC de, et al. Maintenance Dialysis throughout the World in Years 1990 and 2010. *JASN*. 2015 Jul 24;ASN.2014101017.
6. Persans PD, Berry NE, Recht D, Hutchinson D, **Peterson H**, Clark J, et al. Photocarrier lifetime and transport in silicon supersaturated with sulfur. *Applied Physics Letters*. 2012 Sep 10;101(11):111105.

## Book Chapters

1. **H. M. Peterson**, Y. Y. Lee, T. Vos, and A. D. Flaxman, “Unclear age patterns, requiring expert priors: premenstrual syndrome,” in *An Integrative MetaRegression Framework for Descriptive Epidemiology*, A. D. Flaxman, T. Vos, and C. J. L. Murray, Eds. Seattle and London: University of Washington Press, 2015, pp. 117–123.
2. D. Chou, **H. M. Peterson**, A. D. Flaxman, C. J. L. Murray, and M. Naghavi, “Empirical priors: pancreatitis,” in *An Integrative MetaRegression Framework for Descriptive Epidemiology*, A. D. Flaxman, T. Vos, and C. J. L. Murray, Eds. Seattle and London: University of Washington Press, 2015, pp. 125–128.
3. M. H. Forouzanfar, A. D. Flaxman, **H. M. Peterson**, M. Naghavi, and S. Chugh, “Overlapping, heterogeneous age groups: atrial fibrillation,” in *An Integrative MetaRegression Framework for Descriptive Epidemiology*, A. D. Flaxman, T. Vos, and C. J. L. Murray, Eds. Seattle and London: University of Washington Press, 2015, pp. 129–133.
4. A. D. Flaxman, K. M. Hanafiah, J. Groeger, **H. M. Peterson**, and S. T. Wiersma, “Dealing with geographical variation: hepatitis C virus infection,” in *An Integrative MetaRegression Framework for Descriptive Epidemiology*, A. D. Flaxman, T. Vos, and C. J. L. Murray, Eds. Seattle and London: University of Washington Press, 2015, pp. 135–140.
5. A. Mokdad, A. D. Flaxman, **H. M. Peterson**, C. J. L. Murray, and M. Naghavi, “Improving outofsample prediction: liver cirrhosis,” in *An Integrative MetaRegression Framework for Descriptive Epidemiology*, A. D. Flaxman, T. Vos, and C. J. L. Murray, Eds. Seattle and London: University of Washington Press, 2015, pp. 145–148.
6. A. Lim, **H. M. Peterson**, and A. D. Flaxman, “Risk factors: fruit consumption,” in *An Integrative MetaRegression Framework for Descriptive Epidemiology*, A. D. Flaxman, T. Vos, and C. J. L. Murray, Eds. Seattle and London: University of Washington Press, 2015, pp. 149–153.
7. A. Ferrari, A. D. Flaxman, **H. M. Peterson**, T. Vos, and H. Whiteford, “Expert priors in compartmental models: bipolar disorder,” in *An Integrative MetaRegression Framework for Descriptive Epidemiology*, A. D. Flaxman, T. Vos, and C. J. L. Murray, Eds. Seattle and London: University of Washington Press, 2015, pp. 165–169.
8. T. Vos, J. Blore, A. D. Flaxman, **H. M. Peterson**, and J. Rehm, “Cause-specific mortality rates: alcohol dependence,” in *An Integrative MetaRegression Framework for Descriptive Epidemiology*, A. D. Flaxman, T. Vos, and C. J. L.

Murray, Eds. Seattle and London: University of Washington Press, 2015, pp. 171–174.

## Invited Talks

1. **Peterson HM**, Hoang BH, Geller D, Yang R, et. al. “Clinical feasibility of chemotherapy monitoring for bone sarcoma patients with Diffuse Optical Spectroscopic Imaging”. New England Symposium on Biomedical Optics; 2017 October 16; Cambridge, MA, USA.

## Abstracts and Conference Proceedings

(\*oral presenter, \*\*poster presenter)

1. **Peterson HM\*\***, Cox B, Hoang BH, Geller D, Yang R, et al. “Improvements in diffuse optical spectroscopic imaging (DOSI) for the measurement of sarcoma tumors”. Photonics West Bios; 2019 February 04; San Francisco, CA, USA.
2. Spink S, Teng F, **Peterson H**, Ko N, Roblyer D. “High optode-density wearable probe for monitoring tumor dynamics during neoadjuvant chemotherapy”. Photonics West Bios; 2019 February 02; San Francisco, CA, USA.
3. Tank A, **Peterson H**, Tabassum S, Pera V, Ko N, et al. “Diffuse optical spectroscopic imaging reveals dose and schedule dependent changes in breast tumors throughout neoadjuvant chemotherapy”. Photonics West Bios; 2019 February 06; San Francisco, CA, USA
4. **Peterson HM\***, Hoang BH, Geller D, Yang R, Gorlick R, et al. “Imaging sarcoma with diffuse optical spectroscopy”. SPIE Translational Biophotonics; 2018 May 14; Houston, TX, USA.
5. Istfan R, **Peterson H**, Teng F, Applegate M, et al. “Frequency domain diffuse optics for real-time imaging of cancer treatment response”. Physics of Quantum Electronics. Snowbird, UT, USA. 2018. p. 288.
6. **Peterson HM\*\***, Hoang BH, Geller D, Gorlick R, Yang R, Berger J, et al. “Clinical feasibility of chemotherapy monitoring for bone sarcoma patients with diffuse optical spectroscopic imaging.” In: CLINICAL RESEARCH: Childhood Cancer Clinical Translational Research [Internet]. Washington, DC, USA: AACR; 2017. p. 177–8.
7. **Peterson H\*** and Roblyer D, “Clinical Feasibility of Diffuse Optical Spectroscopic Imaging for Sarcoma,” presented at the Biomedical Optics Congress, Hollywood, Florida, USA, 2016, p. TTh3B.6.



8. Torjesen A, Istfan R, **Peterson H**, and Roblyer D, “An UltraFast Digital Diffuse Optical Spectroscopic Imaging (dDOSI) System for Monitoring Chemotherapy Response,” presented at the Biomedical Optics Congress, Hollywood, Florida, USA, 2016, p. OTh3C.1.
9. **Peterson HM\***, Harvey BC, Parameswaran H, and Lutchen KR, “Effect Of Airway Size On The Bronchodilatory Response Induced By Tidal Breathing And Deep Inspirations,” in B30. DYNAMICS OF AIRWAY NARROWING IN ASTHMA: STILL MISUNDERSTOOD?, 271 vols., American Thoracic Society, 2014, pp. A2687–A2687.
10. **Peterson HM\*** and Flaxman AD, “Metaregression with DisMod-MR: how robust is the model?,” *The Lancet*, vol. 381, Supplement 2, p. S110, Jun. 2013.
11. Persans PD, Berry NE, Recht D, Hutchinson D, Said AJ, Warrender JM, **Peterson H**, DiFranzo A, McGahan C, Clark J, Cunningham W, and Aziz MJ, “Photocarrier Excitation and Transport in Hyperdoped Planar Silicon Devices,” in Symposium A—Amorphous and Polycrystalline Thin-Film Silicon Science and Technology, 2011, vol. 1321.